Development of a versatile sum-frequency microscope and application to chemical imaging of interfaces

par

Dominik M.P. HOFFMANN

Diplom-Physiker, Universität Würzburg, Germany

acceptée sur proposition du jury

Prof. K. Kern, directeur de thèse

Dr. C. Bosshard, rapporteur

Prof. F. Lévy, rapporteur

Prof. K. Wandelt, rapporteur

Lausanne, EPFL

2003

Abstract

Visible-IR-sum-frequency (SFG) spectroscopy is a valuable vibrational spectroscopy suited for in-situ studies of interfaces. Chemical information can be obtained from the resonant enhancement of the SFG intensity, when the tunable IR beam is in resonance with vibrations of a specific molecular group.

In this thesis, a novel sum-frequency microscope (SFM) has been developed and built. It allows the chemical imaging of non-transparent samples like metals and semiconductors. For such samples the interface is imaged most efficiently at an angle of 60° with respect to the surface normal and the new design assures focus over the full field of view (240×240 μm^2) with a spatial resolution of 3 μm. In contrast to "specular" SFG spectroscopy, the incident beams reflected from the sample and the generated SFG light cannot be separated by angular filtering. In this setup the separation thus relies on efficient spectral filtering.

The SFM allows to map chemical composition, order and molecular orientation of self-assembled monolayers (SAMs) prepared from solution and by microcontact printing (μCP). The thesis demonstrates that the results obtainable by this new technique are in part complementary to those of chemical AFM, which is sometimes used for investigating patterned self-assembled monolayers. The chemical specificity allows to address the individual building blocks of a SAM: Head group, terminal group and molecular backbone. Different thiolates are discriminated by their specific vibrational resonances or their SFG spectra, respectively. The nonlinear optical properties of the Au(111) surface are substantially modified by the adsorption of the thiolate, i.e. of the sulfur. This is exploited in this thesis to image quantitatively the total thiolate density with sub-monolayer sensitivity. It is possible to investigate the interspace between microcontact printed thiolate patterns; and thus the different paths by which thiols transfer from the stamp to the Au substrate. We find, that the interspace is covered by octadecanethiolate corresponding to a half monolayer, which is a surprisingly high value attributed to the vapor phase transport during μCP.

The SFM is employed for the local characterization of monolayers with inscribed

chemical micropatterns that are prepared by microcontact printing of one thiol species and post-adsorbing the other from solution. Octadecanethiol and mercaptohexade-canoic acid are used in both preparation orders. The SFM images taken at different IR wavelengths reveal that substantial mixing of phases (> 10% of a ML) occurs in the printed pattern as well as in the interspace. From the local evaluation of the SFG spectra it is concluded that mercaptohexadecanoic acid molecules replace octadecanethi-olate more readily than vice versa.

The hydrophobic recovery of a plasma etched PDMS surface is investigated by SFG spectroscopy. For an untreated surface the methyl groups are found to have a preferential orientation along the surface normal. During oxygen plasma etching the density of oriented methyl groups decreases only by 30%, while the contact angle decreases from 110° to nearly 0°. After the etching we observe an increase in the density of ordered methyl groups only within the first 200 h. Then the density remains constant. Contact angle measurements, in contrast, find a hydrophobic recovery of PDMS on the time scale of 1000 h, which indicates the presence of an additional slower process. The results demonstrate the separation of distinct processes in the hydrophobic recovery of PDMS by SFG spectroscopy.

NaCl crystallites on Au are found to emit intense SFG light up to 2000 times more intense than the SFG signal of a clean Au surface. First experiments are done in order to understand this effect and to check for the possibility of reducing SFG measuring times for molecular films by its use. The observations indicate, however, that the high intensity may be correlated to inner defects of the crystallites.

Zusammenfassung

IR-vis-Summenfrequenz-Spektroskopie eignet sich besonders zur in-situ Untersuchung von Schwingungen an Grenzflächen. Sie liefert chemische Information durch die Resonanz-Verstärkung des SFG Signals, wenn die spektral durchstimmbaren IR-Pulse auf die Übergänge einer spezifischen Molekülgruppe abgestimmt sind.

Ein neuartiges Summenfrequenz-Mikroskop (SFM) wurde im Rahmen dieser Arbeit entwickelt und aufgebaut. Es ermöglicht die chemische Abbildung von nichttransparenten Proben, wie z.B. Metallen oder Halbleitern. Für solche Proben erfolgt die effizienteste Abbildung unter einem Winkel von 60° bezogen auf die Oberflächennormale. Das neue Design stellt die Schärfe im gesamten Bildfeld (240×240 μm^2) sicher und besitzt eine Ortsauflösung von 3 μm. Im Gegensatz zur "spiegelnden" Summenfrequenz-Spektroskopie können der sichtbare und der IR Strahl, die von der Oberfläche reflektiert werden, nicht durch räumliche Filterung separiert werden. Daher beruht die Trennung in diesem Aufbau auf die effiziente Trennung mit spektralen Filtern.

Mit dem SFM wird die chemische Zusammensetzung, die Ordnung und die molekulare Orientierung der Moleküle in selbst-aggregierenden Monolagen (SAMs) untersucht. Die SAMs werden entweder aus der Lösung oder durch Stempeln (μCP) präpariert. Die in dieser Arbeit vorgestellten Ergebnisse sind teilweise komplementär zu den Messungen an strukturierten SAMs mit chemisch funktionalisiertem AFM. Die chemische Selektivität der Summenfrequenz-Erzeugung ermöglicht es, die Eigenschaften der individuellen Bestandteile (Kopfgruppe, Endgruppe und die Methylen-Kette) einer selbst-aggregierenden Monolage zu untersuchen. Unterschiedliche Thiolate werden durch spezifische Schwingungsresonanzen, bzw. durch ihr SFG-Spektrum identifiziert. Die nichtlinearen optischen Eigenschaften der Au(111) Oberfläche werden durch die Adsorption von Thiol, d.h. durch die Bindung zum Schwefelatom, deutlich geändert. Die Änderung wird in dieser Arbeit dazu benutzt, die absolute Thiolatdichte quantitativ abzubilden. Die Methode ist dabei sensitiv auf Bruchteile einer Monolage. So kann die Thiolat-

dichte im Zwischenraum zwischen gestempelten Thiolatstrukturen untersucht werden. Diese ermöglicht Rückschlüsse auf die verschiedenen Wege, über die beim μCP Thiole vom Stempel auf das Goldsubstrat gelangen. Eine überraschend hohe Bedeckung des Zwischenraums mit einer halben Monolage Octadecanthiol kann auf den Transport von Thiolen durch die Gasphase zurückgeführt werden.

Monolagen mit eingeschriebenen chemischen Mikrostrukturen werden lokal mit dem SFM charakterisiert. Die Mikrostrukturen werden durch μCP mit einem Thiol und nachfolgender Adsorption eines anderen Thiols aus der Lösung erzeugt. Dafür werden Octadecanthiol und Mercaptohexadecanol in beiden Präparationsreihenfolgen verwendet. SFM Bilder für verschiedene IR Wellenlängen zeigen eine deutliche Mischung der einzelnen Thiolphasen ($> 10\%$ einer Monolage) sowohl im gestempelten Muster als auch in den Zwischenräumen. Die lokale Auswertung der SFG-Spektren ergibt, daß Octadecanthiol schneller durch Mercaptohexadecanol ersetzt wird als andersherum.

In einem weiteren Teil dieser Arbeit wird für plasmageätztes Polydimethylsiloxan (PDMS) die Rückkehr vom hydrophilen in den hydrophoben Zustand mit Summenfrequenz-Spektroskopie untersucht. Die Spektren zeigen, daß die Methylgruppen an einer unbehandelten PDMS-Oberfläche vorzugsweise entlang der Oberflächennormalen orientiert sind.

Die Dichte der orientierten Methylgruppen nimmt durch das Ätzen nur um 30% ab, wärend der Kontaktwinkel von 110° auf 0° sinkt. Nach dem Plasmaätzen beobachten wir einen Anstieg der Dichte an orientierten Methylgruppen innerhalb der ersten 200 h. Danach bleibt die Dichte in etwa konstant. Im Gegensatz dazu zeigen die Kontaktwinkelmessungen eine Rückkehr des PDMS zum hydrophoben Zustand auf der Zeitskala von 1000 h. Dieses deutet auf einen weiteren, langsameren Prozess hin. Unsere Ergebnisse demonstrieren, daß einzelne Prozesse während der Änderung der PDMS-Oberfläche durch SFG Spektroskopie separiert werden können.

Auf Au deponierte NaCl-Kristallite zeigen eine SFG Emission mit einer bis zu 2000fach höheren Intensität als die von einer reinen Goldoberfläche. Erste Experimente, um den Ursprung der Emission herauszufinden und um abzuklären, ob der Effekt zur Reduktion der Meßzeiten in der Summenfrequenz-Mikroskopie benutzt werden kann, werden gezeigt. Die Beobachtungen legen jedoch die Annahme nahe, daß der Effekt mit inneren Defekten im NaCl Kristallit zusammenhängt.

per aspera cum astro

Contents

Chapter 1

Introduction

Physical and chemical phenomena in science and in everyday life can be ascribed very often to properties of and to processes at interfaces and surfaces. The understanding of the interface is therefore of central interest in fundamental research as well as in technical and industrial applications. Accordingly surface scientists work e.g. in life sciences, physics, material science and engineering, covering a broad variety of fields. The humane immune system, for instance, discriminates between bodily and external tissue by receptors on the cell membrane, which represents a biological interface. As a medical consequence the biocompatibility of anorganic implant surfaces must be assured, i.e. very often they must be modified. Self-assembled monolayers (SAMs) with appropriate chemical functionalities are suited to connect anorganic and biological material. With them proteins and cells can be attached selectively to anorganic substrates. In the field of tribology, as another example, the surface of solids and the interface of solids in contact is studied systematically. The practical relevance lies e.g. in mechanical engineering – surfaces of specific parts in the automotive sector have to be characterized on the scale of some 10 nm – , fabrication of wear-resistant materials, and reduced friction. A last example is the growth of semiconductor hetero-structures by molecular beam epitaxy (MBE) in ultra high vacuum (UHV), which are used e.g. for laser diodes or the growth of quantum dots. These hetero-epitaxial systems typically exhibit numerous interfaces.

This process of hetero-epitaxial growth as many others is studied in the UHV, which allows to work under clean conditions and to prepare well defined (model)systems. These can be studied with a whole zoo of experimental techniques. However, many systems show different properties in the vacuum than they do under ambient conditions (e.g. in air or in an electrochemical solution) and should thus be studied in this environment. A further class of interfaces and processes can only be studied under ambient conditions,

as e.g cell membranes under physiological conditions or the electrochemical deposition of metal atoms.

The question of chemical composition of a surface and the chemical identification of adsorbates is often important in studying those interfaces. Many methods apt for chemical characterization in UHV, as e.g. high resolution electron energy loss spectroscopy (HREELS) and X-ray photoelectron spectroscopy (XPS), are not applicable under ambient conditions. In contrast, optical spectroscopic techniques can be used for samples under either condition as long as the light can access the interface e.g. in the liquid or gaseous environment. IR spectroscopy, Raman spectroscopy and coherent anti-Raman spectroscopy (CARS) yield chemical selective information due to specific vibrations of chemical groups. For transparent samples they probe the surface and the bulk, for opaque samples the spectral information typically stems from the surface layer with a thickness on the order of the utilized wavelength.

Predicted theoretically by Nobel laureate Bloembergen in the 60's of the last century, nonlinear optical effects have been increasingly investigated since the 80's enabled by the development of laser systems with short pulses and thus high peak intensities. Soon also the surface sensitivity of second order processes was shown and pioneered by Shen and coworkers. In several experiments on a wide variety of interfaces the sensitivity of second-harmonic generation (SHG) and sum-frequency generation (SFG) spectroscopy to the upper few atomic layers of centro-symmetric materials was demonstrated and exploited. This high interfacial selectivity makes SHG and SFG spectroscopy real surface science techniques when compared to linear optical methods or to third order optical processes. Particularly SFG spectroscopy is used with great success to probe in-situ the order and the molecular orientation at solid surfaces as well as at solid-liquid and liquid-liquid interfaces.

Within the last decade various nonlinear spectroscopic techniques as e.g. SHG have been extended to imaging methods. Especially SHG microscopy is more and more used in biological studies on membranes. For that cause, molecules labelled with specially designed chromophores – similar as in fluorescence microscopy – are incorporated into the membrane.

Vis-IR-sum-frequency spectroscopy yields chemical information as the SFG signal is resonantly enhanced, when the IR wavelength corresponds to a vibrational transition. Thus sum-frequency microscopy (SFM) can identify specific chemical groups without the need for dye molecules, as the signal is enhanced by vibrational resonances at the interface. It is known, that the spectral region of the C-H vibrations, present in many

membrane systems, can readily be probed by SFG. SFG is very sensitive to the local order and conformation of molecules, which are further parameters of interest in membrane systems. SFG, moreover, was demonstrated for a variety of other vibrational resonances, as e.g. for those of hydrogen on silicon.

The subject of this thesis has been the development of a sum-frequency microscope that is applicable to opaque and to transparent samples and that allows for in-situ chemical mapping of surfaces and interface-sensitive local spectroscopy on the micrometer scale. A further goal was the characterization of chemically inhomogeneous self-assembled monolayers with this novel SFM, as SAMs represent a widely used model system for biomembranes.

This thesis is structured as follows: The interaction of light with matter is discussed in chapter 2 with the focus on the nonlinear optical effects and the fundamentals of sum-frequency generation spectroscopy. The mechanisms of contrast in sum-frequency microscopy are also introduced in chapter 2. As the SFM should be applicable to a wide range of materials, including metals and semiconductors, it is designed for the use in reflection mode. The geometric constraints, which become obvious already in chapter 2, require a novel design that is introduced in chapter 3. In this chapter also the optical performance of the SFM is characterized. The sub-monolayer chemical sensitivity is proven by the investigations of SAMs in chapter 4. The capability of chemical mapping on interfaces is applied amongst others to study exchange processes during the preparation of chemically micropatterned SAMs. These patterns are produced by microcontact printing with a stamp made from polydimethylsiloxane (PDMS). Little is known of the interface stamp/air particularly when the stamp surface is impregnated with a solution containing thiols. It is shown in chapter 5 that sum-frequency spectroscopy is an apt method to study this interface. The results of localized intense emission from NaCl crystallites illuminated with visible and IR laser pulses (chapter 6) demonstrates a further strength of sum-frequency microcopy, namely to identify strong but very localized inhomogeneities, which would hardly be seen in the spatially averaged signal of SFG spectroscopy.

Chapter 2

Theory of nonlinear optics

Photons do not interact. This holds in vacuum because the Maxwell equations are linear differential equations[1]. This changes when photons interact with matter. The first section 2.1 shows this in the microscopic model of the anharmonic oscillator, which is then related to the macroscopic description with polarization densities and susceptibilities within the electric dipole approximation. Focusing on the second order electric susceptibility the main symmetry properties will be listed briefly in section 2.2. Then the geometrical requirements of an SFG experiment on metallic surfaces is introduced as it is the basis for the novel microscope design presented in this thesis (section 2.3). The use of vis-IR sum-frequency generation as a vibrational spectroscopy technique is introduced in section 2.4. Finally the contrast mechanisms used for chemical imaging in sum-frequency microscopy, namely electronic and vibrational contrast, are explained in section 2.5.

2.1 Linear and nonlinear interaction of electromagnetic fields with matter

The interaction of light with a molecule can be modelled in the classical microscopic picture with the 1-dimensional anharmonic oscillator. The molecule is assumed to have an asymmetric charge distribution. If now an external electric field E is applied, the charges q^+ and q^- are moved from the equilibrium distance x_0 of their centers of gravity by the displacement

$$r = \left| \left(x(q^+) - x_0/2 \right) - \left(x(q^-) - (-x_0/2) \right) \right| \tag{2.1}$$

---

[1]Let aside quantum mechanical effects for extremely energetic photons
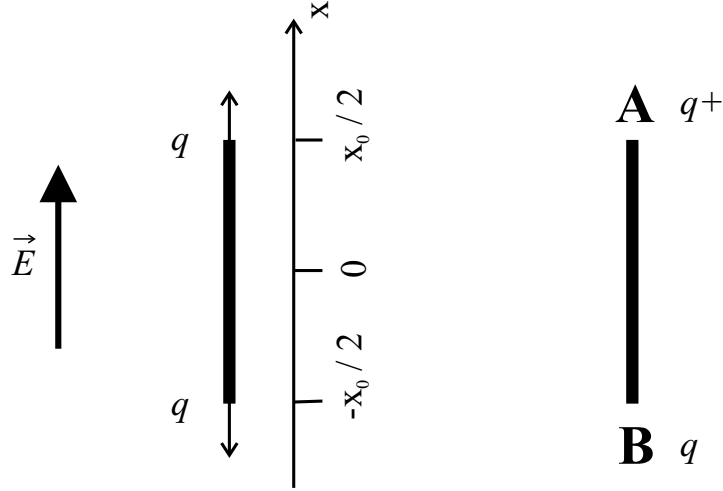
Figure 2.1: Static and dynamic dipole moment: A hetero-nuclear bond A-B can exhibit a static dipole moment qx_0, with q^+ and q^- being the respective net charges. An external electric field $\vec{E}$ induces a displacement of the charges from their equilibrium distance x_0. This corresponds to a dynamic dipole.

and an dynamic dipole $\mu_{ind} = qr$ is induced as schematized in Fig. 2.1 for a hetero-nuclear bond. A restoring force $F(r)$ acts on q^+ and q^-. In a first approximation F is linear in r

$$F = -m\omega_0^2 r \quad . \tag{2.2}$$

Thus the potential U is parabolic (Fig. 2.2, solid line) and the displacement r is governed by the equation of motion of the harmonic oscillator:

$$\ddot{r} + 2\Gamma\dot{r} + \omega_0^2 r = -\frac{q}{m}E \tag{2.3}$$

Γ is the damping constant, ω_0 the natural frequency of the harmonic oscillator and m the reduced mass.

For a time-dependent driving electric field

$$E = E(\omega)e^{-i\omega t} + E^*(\omega)e^{i\omega t} \tag{2.4}$$

with the complex amplitude

$$E(\omega) = \frac{1}{2}|E|e^{-i\varphi}, \tag{2.5}$$

the solution of the linear differential equation (2.3) is given by [1]

$$r^{(1)} = -\frac{e}{m}E(\omega)\frac{e^{-i\omega t}}{\omega_0^2 - 2i\Gamma\omega - \omega^2} + c.c. \quad . \tag{2.6}$$

Here $r^{(1)}$ denotes the solution belonging to the linearly approximated restoring force. The displacement $r^{(1)}$ is linear in E and it oscillates thus at the same frequency ω giving rise to a linear response of the molecule.
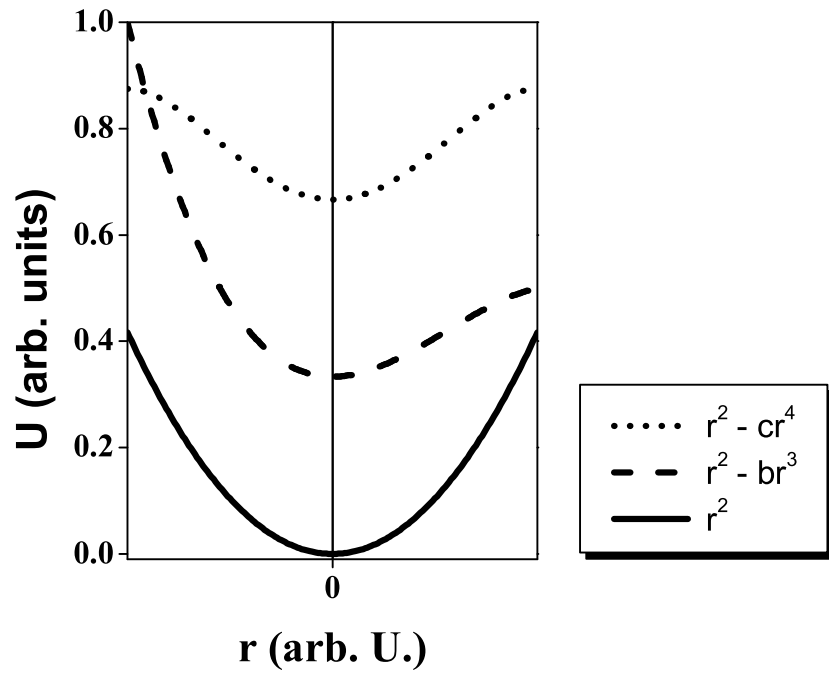
Figure 2.2: Potential as a function of the displacement of positive and negative charges from the equilibrium distance: Harmonic approximation (solid line), potential for a non-centro-symmetric material (dashed line), potential for a centro-symmetric material (dotted line). (curves have been offset for clarity, see also text)

Being sufficient in most cases the linear model of the harmonic oscillator breaks down if electric fields are of the same order as the inner atomic fields ($\approx 10^{10}$ Vm^{-1}). Then the linear approximation for F (2.2) is not sufficient and terms of higher order in r have to be taken into account. Adding the lowest order correction to F

$$F = -m\omega_0^2 r - mbr^2 \qquad (2.7)$$

results in a potential U

$$U = -\int F\,dr = \frac{1}{2}m\omega_0 r^2 + \frac{1}{3}mbr^3, \qquad (2.8)$$

where b is a measure for the strength of the nonlinearity. This potential is non-centro-symmetric (Fig. 2.2 (dashed line)). Solving the equation of motion for this anharmonic potential and an external electric field given by (2.4) leads to two additional terms $r^{(2)}$ with frequencies $\omega_{DC} = 0$ and $\omega_{SHG} = 2\omega$. The DC component can be interpreted as an increase in the equilibrium distance due to the anharmonicity of the potential. The terms at the doubled fundamental frequency of the driving electric field is the special case of anharmonic oscillator driven by a electric field consisting of two frequency components. This process will be discussed now because it is the origin of sum-frequency generation.

We assume an external electric field $E(t)$ consisting of two components with two different frequencies ω_1 and ω_2:

$$E(t) = E(\omega)e^{-i\omega_1 t} + E(\omega)e^{-i\omega_2 t} + c.c. \tag{2.9}$$

An analytical solution of the equation of motion with the potential U (2.8) and the external field $E(t)$ (2.9) is not known. However, if the nonlinear term of the restoring force is small in comparison to the linear term, perturbation theory yields the result that the displacement r has the already known contributions $r^{(1)}$ linear in E and that the lowest order nonlinear correction $r^{(2)}$ to the displacement r is of second order in the applied electric field E^2. These second order corrections have components at frequency combinations of ω_1 and ω_2 namely $2\omega_1$, $2\omega_2$, $\omega_1 + \omega_2$, $\omega_1 - \omega_2$ and 0 [2]. Thus we find for the total displacement r:

$$r = a_1 r^{(1)}(\omega_1) + a_2 r^{(1)}(\omega_2) +$$
$$+ b_1 r^{(2)}(2\omega_1) + b_2 r^{(2)}(2\omega_2) + b_3 r^{(2)}(\omega_1 + \omega_2) + b_4 r^{(2)}(\omega_1 - \omega_2) + b_5 r^{(2)}(0) \tag{2.10}$$

where a_n and b_n are respective coefficients.

The oscillator model used so far has been one-dimensional in order to discuss the underlying processes of the interaction between light and matter. This model, however, cannot include the tensorial character of this interaction. This is possible in the three dimensional notation, which will be used from now on.

The displacement $\vec{r}$ of a charge e results in an induced dipole moment $\vec{\mu}_{ind}$:

$$\vec{\mu} = \vec{\mu_0} + \vec{\mu_{ind}} = \vec{\mu_0} + e\vec{r} = \vec{\mu_0} + \alpha\vec{E} + \beta\vec{E}\vec{E} + ..., \tag{2.11}$$

where $\vec{\mu_0}$ is the static dipole moment. The molecular polarizability α corresponds to $r^{(1)}$ (2.10) and $\alpha\vec{E}$ is the short notation for $\alpha_{ij}E_j$ where E_j is the jth component of $\vec{E}$. The hyperpolarizability β corresponds to $r^{(2)}$ and it is a tensor of third rank. $\beta\vec{E}\vec{E}$ is the short form of $\beta_{ijk}E_jE_k$. (Throughout this thesis the Einstein convention is used, i. e. the sum is taken over all double indices.)

Optical methods average over a spatial region of the scale of the wavelength λ or larger, i.e. in the μm range. Therefore it is useful to relate the microscopic dipole

---

[2]For centro-symmetric media the potential with the smallest symmetry allowed nonlinear extension is

$$U = - \int F dr = \frac{1}{2}m\omega_0^2 r^2 + \frac{1}{4}mcr^4,$$

where c is a strength parameter of the nonlinearity (Fig. 2.2, dotted line). The lowest nonlinear term in the displacement is of third order in E [2]. This explains in the microscopic image why second order processes are forbidden in centro-symmetric molecules and materials.
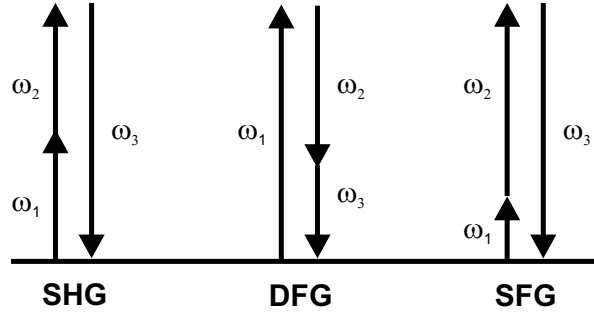
Figure 2.3: Energy term schemes representing the conservation of energy in second order optical processes with non-static output: Second-harmonic generation, difference-frequency generation and sum-frequency generation.

moment $\vec{\mu}$ to a macroscopic quantity. Ensemble and spatial averaging over the molecular dipole moments yields the macroscopic polarization density $\vec{P}$:

$$
\begin{aligned}
\vec{P}(t) &= \vec{P^{(0)}} + \vec{P}^{(1)}(t) + \vec{P}^{(2)}(t) + ... = N\langle\vec{\mu}\rangle \\
&= \langle\vec{\mu_0}\rangle + \varepsilon_0\left(\chi^{(1)}\vec{E}(t) + \overleftrightarrow{\chi}^{(2)} : \vec{E}(t)\vec{E}(t) + ...\right),
\end{aligned}
\tag{2.12}
$$

where $\chi^{(1)}$ denotes the linear susceptibility and $\overleftrightarrow{\chi}^{(2)}$ the first order nonlinear susceptibility[3]. N is the density of microscopic dipole moments $\vec{\mu}$. If the polarization density $\vec{P}(t)$ is oscillating, it emits light with the same frequency.

As will be shown in the following, a non-vanishing $\overleftrightarrow{\chi}^{(2)}$ leads to the coupling of photons, which is not possible in vacuum. The superimposed electric field $\vec{E}(t)$ of two monochromatic plain waves at a fixed position is given by:

$$
\vec{E}(t) = \vec{E_1}\sin(\omega_1 t) + \vec{E_2}\sin(\omega_2 t)
\tag{2.13}
$$

Inserting (2.13) into the first order nonlinear term on the right-hand side in (2.12) yields

$$
\vec{P}^{(2)} = \varepsilon_0\overleftrightarrow{\chi}^{(2)} : \vec{E}\vec{E} =
$$

$$
\frac{1}{2}\varepsilon_0\overleftrightarrow{\chi}^{(2)} : \underbrace{(\vec{E_1^2} + \vec{E_2^2})}_{static} + \varepsilon_0\frac{1}{2}\overleftrightarrow{\chi}^{(2)} : \underbrace{\left(\vec{E_1^2}\cos(2\omega_1 t) + \vec{E_2^2}\cos(2\omega_2 t)\right)}_{SHG} +
$$

$$
+ \varepsilon_0\overleftrightarrow{\chi}^{(2)} : \vec{E_1}\vec{E_2}\left(\underbrace{\cos[(\omega_2 - \omega_1)t]}_{DFG} - \underbrace{\cos[(\omega_2 + \omega_1)t]}_{SFG}\right)
\tag{2.14}
$$

$$
= \vec{P}^{(2)}(0) + \vec{P}^{(2)}(2\omega_1) + \vec{P}^{(2)}(2\omega_2) + \vec{P}^{(2)}(\omega_2 - \omega_1)\vec{P}^{(2)}(\omega_2 + \omega_1)
$$

The DC polarization density $\vec{P}^{(2)}(0)$ results in optical rectification, i.e an induced static electric field. The oscillating electric fields induce polarization components in the

---

[3]For the first order nonlinear susceptibility also the term second order susceptibility is common. Both expressions are used equivalently in this thesis.

material at the second harmonic (SHG) of the fundamental frequencies as well as at the difference (DFG) and at the sum (SFG) of both frequencies. So this process can be understood as the coupling of three photons by $\overleftrightarrow{\chi}^{(2)}$. The process is therefore called three-wave mixing. Fig. 2.3 shows schematically the non-static second order processes just described.

Expression 2.14 was derived from the model for a molecule. It is valid, however, in general for the interaction of light with matter, as it can be deduced also directly from the Maxwell equations. It is also important to keep in mind that the presented derivation of the interaction between light and matter is the dipole approximation as it only considers the polarization density $\vec{P}$. Often this is sufficient but particularly if $\vec{P}$ vanishes, the electric quadrupole moment and the magnetic dipole moment may have to be considered.

2.2   Symmetry properties of the first order nonlinear susceptibility

$\overleftrightarrow{\chi}^{(2)}$ is a third rank tensor comprising 27 elements $\chi^{(2)}_{ijk}(\omega_3; \omega_1, \omega_2)$ with

$$P_i^{(2)}(\omega_3 = \omega_1 + \omega_2) = \varepsilon_0 \chi^{(2)}_{ijk}(\omega_3; \omega_1, \omega_2) E_j(\omega_1) E_k(\omega_2) \tag{2.15}$$

in the case of sum-frequency generation (indices i, j, k indicating the spatial coordinates). Nevertheless they are not all independent. Symmetry allows to reduce the number of independent tensor elements. Permutation symmetries are due to the formal concept of nonlinear susceptibility itself while spatial symmetries reflect physical properties of the material [2][4].

2.2.1   Permutation symmetries

Intrinsic permutation symmetry

According to expression (2.15) the ith component of the nonlinear polarization $\vec{P}^{(2)}$ is given by the sum over terms of the form $\chi^{(2)}_{ijk}(\omega_3; \omega_1, \omega_2) E_j(\omega_1) E_k(\omega_2)$. j and k are just dummy indices, and it can be required that the tensor element $\chi^{(2)}_{ijk}$ stays unchanged if j and k are interchanged simultaneously with the frequency arguments ω_1 and ω_2. Thus we have

$$\chi^{(2)}_{ijk}(\omega_3; \omega_1, \omega_2) = \chi^{(2)}_{ikj}(\omega_3; \omega_2, \omega_1) \qquad . \tag{2.16}$$

---

[4]The reference contains also more detailed information on the individual symmetries discussed in this section.

This so-called intrinsic permutation symmetry reduces the number of independent tensor elements to 18. However, this symmetry has been introduced for convenience. If one would set one value in (2.16) to zero and double the other value, the result for the physically meaningful property $P_i^{(2)}$ would be the same [2].

Full permutation symmetry

The intrinsic permutation symmetry is extended to a full permutation symmetry for the pairs of spatial indices with their respective frequencies if all frequencies are far from resonance and thus from absorption. One important consequence of the full or overall permutation symmetry is the Manley-Rowe relation [2]. Put in a nutshell, this relation states that for each photon created at the sum frequency ω_3 one photon at ω_1 and one at ω_2 are annihilated. Processes within the validity of the Manley-Rowe relation are called *parametric* and are used for frequency conversion in nonlinear crystals (section 3.1.

Kleinmann symmetry

If the involved frequencies are much smaller than the lowest resonance frequency of the material, $\overleftrightarrow{\chi}^{(2)}(\omega)$ can be taken as independent of frequency. Therefore the indices can be permuted without the respective frequencies. This Kleinmann symmetry leads to 10 remaining independent tensor elements.

2.2.2 Spatial symmetries

According to the *Neumann* principle the symmetry properties of any physical quantity must include all symmetry elements of the point group of the material. This means, that spatial transformations belonging to the symmetry group of the material leave all physical properties unchanged. Thus $\chi_{ijk}^{(2)}$ is invariant under these symmetry transformations. Therefore the number of independent tensor elements may decrease even further depending on the sample symmetry. This will now be illustrated for a centro-symmetric medium.

For a symmetry operation represented by the matrix T_{ij} the first order nonlinear susceptibility $\chi^{(2)}$ transforms as a third rank tensor:

$$\chi_{ijk}^{(2)\prime} = T_{il} T_{jm} T_{kn} \chi_{lmn}^{(2)}. \tag{2.17}$$

Next to identity the symmetry operation for centro-symmetric matter is the inversion,

i. e. T_{ij}=-δ_{ij}. Inserting T_{ij} in (2.17) yields

$$\chi_{ijk}^{(2)'} = -\chi_{ijk}^{(2)} \qquad , \tag{2.18}$$

which holds only if $\chi_{ijk}^{(2)} \equiv 0$ for all elements. Thus in centro-symmetric matter, as e.g. in metals, there are no second order processes within the electric dipole approximation. At the surface, however, inversion symmetry is broken and second order processes are not forbidden. This leads to the important surface and interface selectivity of sum-frequency generation.

For an isotropic interface with rotational invariance and no chiral adsorbates, such as the samples investigated in this work, $\overleftrightarrow{\chi}^{(2)}$ consists only of four independent elements

$$\chi_{xxz}^{(2)}, \chi_{xzx}^{(2)}, \chi_{zxx}^{(2)}, \chi_{zzz}^{(2)} \qquad , \tag{2.19}$$

where the interface lies in the xy-plane [3]. For symmetry reasons the following tensor elements are equivalent:

$$\chi_{xxz}^{(2)} = \chi_{yyz}^{(2)}$$
$$\chi_{zxx}^{(2)} = \chi_{zyy}^{(2)} \tag{2.20}$$
$$\chi_{xzx}^{(2)} = \chi_{yzy}^{(2)}$$

$$\tag{2.21}$$

All other tensor elements are zero.

2.3   Aspects of SFG experiments at opaque interfaces

In the first part of this section the principle of wave vector conservation will be introduced as a consequence of the electrodynamic treatment of the interaction between the laser pulses and the interface. Then the role of polarization for the selective probing of single tensor elements in $\overleftrightarrow{\chi}^{(2)}$ will be sketched. The Fresnel factors will be introduced at the end as the origin for the necessity to do SFG microscopy at oblique angles.

2.3.1   Wave vector conservation

Figure 2.4 shows the geometry of a typical SFG experiment. They can be described by monochromatic planar waves with the momentum

$$\vec{k} = \frac{2\pi}{\lambda} \frac{\vec{k}}{|\vec{k}|} \qquad . \tag{2.22}$$
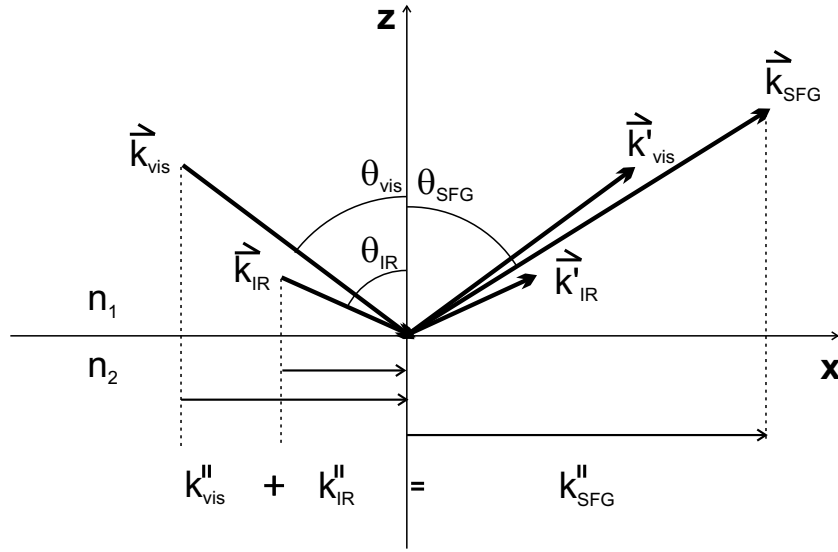
Figure 2.4: Geometry of an SFG experiment on an opaque and homogeneous surface: Energy and parallel momentum conservation lead to the directed radiation of the sum-frequency signal.

The pulses propagate in the xz-plane and the interface between medium 1 and medium 2 lies in the xy-plane at $z = 0$. The respective refractive indices are n_1 and n_2. The y-component of momentum $\vec{k}$ is zero. Medium 1 is assumed to be air, i. e. $n_1 \approx 1$. As the experiments in this thesis are done in reflecting geometry, only the reflected beams are treated.

The visible and the IR beam impinge with their respective momenta $\vec{k}_{vis}$, $\vec{k}_{IR}$ and incidence angles Θ_{vis}, Θ_{IR} on the interface between medium 1 and medium 2. For a metal surface both beams are reflected to a large extent ($\vec{k}'_{vis}$, $\vec{k}'_{IR}$) . A nonlinear polarization density $\vec{P}_{SFG}$ is generated at the interface, which leads to the emission of radiation at the sum-frequency ω_{SFG}. ω_{SFG} is given by:

$$\omega_{SFG} = \omega_{vis} + \omega_{IR} \tag{2.23}$$

The phase relation between the emitters at a homogeneous interface leads to the directed emission of the SFG light at an angle that is given by conservation of the momentum parallel to the interface:

$$k^{||}_{SFG} = k^{||}_{vis} + k^{||}_{IR} \tag{2.24}$$

As

$$\left| \vec{k}_\alpha \right| = \frac{\omega_\alpha}{c_0} n(\omega_\alpha) \tag{2.25}$$

$$with \ n(\omega_\alpha) \approx 1 \ and \ (\alpha = SFG, vis, IR) \quad ,$$

the emission angle for the SFG beam is given by

$$sin\theta_{SFG} = \frac{1}{\omega_{SFG}} (\omega_{vis} \ sin\theta_{vis} + \omega_{IR} \ sin\theta_{IR}) \quad . \tag{2.26}$$

For the geometry in Fig. 2.4 the SFG beam leaves the sample between the IR and the visible reflected beam and propagates closer to the visible beam because ω_{vis} is substantially larger than ω_{IR}.

2.3.2 The role of polarization

So far the polarization of the three involved beams has not been taken into account. Assuming the same coordinate system as in Fig. 2.4, beams are called p-polarized if their electric field vector $\vec{E}$ lies in the plane of incidence, i. e. in the xz-plane. Beams with a polarization perpendicular to that plane consist only of a y-component E_y and are referred to as s-polarized. The possible combinations are identified by a three indices s or p, where by convention the first, second and third letter denote the polarization of the SFG beam, the vis beam, and the IR beam, respectively. Only the combinations ssp, sps, pss and ppp can give rise to an SFG signal at an isotropic interface. Furthermore they probe different elements of the susceptibility tensor $\overleftrightarrow{\chi}^{(2)}$ as given in Table 2.1. More details are found in reference [4].

For a fixed geometry and fixed polarizations the tensor $\overleftrightarrow{\chi}^{(2)}$ can be described by a scalar nonlinear susceptibility $\chi^{(2)}$:

$$I_{SFG} \propto \left|\chi^{(2)}\right|^2 \left|\vec{E}_{vis}\right|^2 \left|\vec{E}_{IR}\right|^2 = \left|\chi^{(2)}\right|^2 I_{vis}I_{IR} \tag{2.27}$$

polarizations	sps	pss	ssp	ppp
probed tensor element	$\chi^{(2)}_{yzy}$	$\chi^{(2)}_{zyy}$	$\chi^{(2)}_{yyz}$	combination of all four independent tensor elements in (2.19)

Table 2.1: Relation between the polarization of SFG, vis and IR beams and the probed tensor elements of the nonlinear susceptibility for an isotropic interface. The first three combinations probe a single element each. With this knowledge $\chi^{(2)}_{zzz}$ can be determined from the measurement with ppp polarization [5].

2.3.3 Nonlinear Fresnel factors

The sum-frequency intensity I_{SFG} is a coherent superposition of the radiation emitted due to the polarization $\vec{P}(\omega_{SFG})$ at the interface. Therefore it is quadratic in $\vec{P}$ and is described following the notation of Hirose et al. [6]:

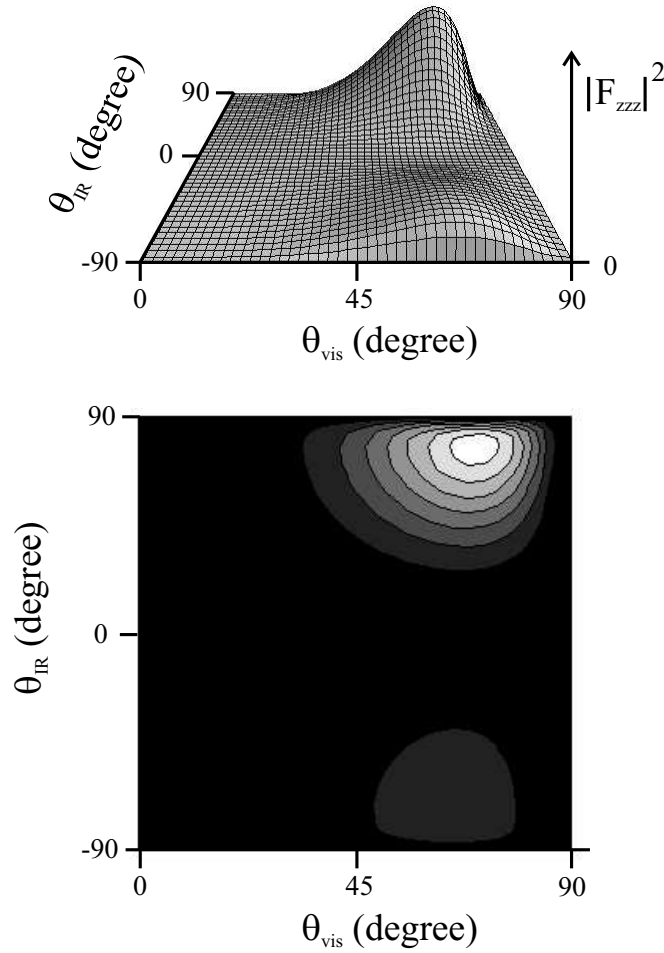$$I_{SFG} \propto \left|L_i\chi^{(2)}_{ijk} K_{j,vis}E_{vis} K_{k,IR}E_{IR}\right|^2 \tag{2.28}$$

Figure 2.5: $|F_{zzz}|^2$ at the air/gold interface as function of the incidence angles θ_{vis} and θ_{IR} ($\omega_{IR} = 2900$ cm^{-1}). The contour-plot (bottom) ranges from 0 to the maximum value of $|F_{zzz}|^2$. One unit in the grey-scale corresponds to 15% of the full scale. $|F_{zzz}|^2$ and the related SFG intensity reach a maximum value for incidence angles of about 70°.

L_i relates the polarization density $\vec{P}$ to the radiated SFG field while K connects the incoming field $\vec{E}_{vis}$ and $\vec{E}_{IR}$ with the effective fields at the interface. The Fresnel coefficients L and K determine the amplitude of reflected and transmitted fields at an interface and can be deduced in classical electrodynamics with the boundary conditions for the electromagnetic fields $\vec{E}$, $\vec{D}$, $\vec{B}$ and $\vec{H}$ at interfaces. Details can be found e.g. in [6]. Usually L and K are combined to the nonlinear Fresnel coefficient F_{ijk}:

$$F_{ijk} = L_i K_j K_k \tag{2.29}$$

For the interface gold/air by far the largest nonlinear Fresnel coefficient that is relevant for the important ppp combination is F_{zzz}. It is larger than the other nonlinear Fresnel factors by at least one order of magnitude. The SFG intensity is proportional to the square of the absolute value of the nonlinear Fresnel coefficient. In Fig. 2.5 $|F_{zzz}|^2$ is

shown as a function of the incidence angles for the vis and IR beam ($\omega_{IR} = 2900$ cm^{-1})[5]. For the calculation the index of refraction n_i in air has been set to 1 for all three involved frequencies. For gold the following values for the refractive index were used [8]:

$$
\begin{aligned}
n_{SFG} &= 1.53 + 1.86i \\
n_{vis} &= 0.46 + 2.27i \\
n_{IR} &= 1.25 + 17.6i
\end{aligned}
$$

$|F_{zzz}|^2$ becomes maximal for $\theta_{IR} \approx 75°$ and $\theta_{vis} \approx 70°$. Note, that $|F_{zzz}|^2$ is zero for incidences angles $\theta_{vis} = \theta_{IR} = 0°$.

In SFG microscopy many samples are isotropic on the scale of some μm. Therefore only four independent tensor elements of $\overleftrightarrow{\chi}^{(2)}$ are observable (section 2.2), one being $\chi^{(2)}_{zzz}$. The resulting SFG intensity is probed by the ppp combination (Tab. 2.19) with the by far strongest nonlinear Fresnel coefficient F_{zzz}.

In conclusion, the constraints imposed by the first order nonlinear susceptibility and by the nonlinear Fresnel coefficients require that sum-frequency microscopy on a metallic surface is done at oblique angles near $70°$.

2.4   Vibrational spectroscopy with SFG

Vibrational spectroscopy is a direct way to obtain chemical information from a sample. Due to its surface specificity and high sensitivity SFG spectroscopy is particularly suited for studying adsorbates on surfaces.

In IR-vis sum-frequency microscopy a visible beam with fixed energy ω_{vis} and an IR beam with tunable ω_{IR} are mixed on the sample and the generated sum-frequency $\omega_{SFG} = \omega_{vis} + \omega_{IR}$ is detected. When ω_{IR} is in resonance with a vibrational transition ω_υ, a resonant enhancement occurs. $\chi^{(2)}$ in eq. (2.27) can be written as

$$
\chi^{(2)} = \chi^{(2)}_{nr} + \chi^{(2)}_{res} \qquad , \tag{2.30}
$$

with $\chi^{(2)}_{nr}$ being the non-resonant second order susceptibility [9]. The resonant second order susceptibility $\chi^{(2)}_{res}$ for a surface layer of molecules is given empirically by the sum over all possible vibrations υ [10]:

$$
\chi^{(2)}_{res} = \sum_\upsilon \frac{C_\upsilon}{\omega_{IR} - \omega_\upsilon - i\Gamma_\upsilon} \qquad , \tag{2.31}
$$

---

[5]See [7] for the explicit formulas.

where Γ_v is a damping constant. C_v is a complex factor of the specific vibration. The square of $\chi_{res,v}^{(2)}$ corresponds to a Lorentzian profile and can be deduced classically from the anharmonic oscillator and quantum mechanically by perturbation theory. The quantum mechanical treatment yields the result, that C_v is essentially the product of IR and Raman cross sections [9, 10]. This is why a vibration must be both IR active and Raman active to be observable in SFG spectroscopy.

The SFG signal is obtained by inserting (2.30) into (2.27):

$$
\begin{aligned}
I_{SFG} \quad &\propto \quad \left|(\chi_{nr}^{(2)} + \chi_{res}^{(2)})\right|^2 \left|\vec{E}_{vis}\right|^2 \left|\vec{E}_{IR}\right|^2 = \\
&= \quad \left(\left|\chi_{nr}^{(2)}\right|^2 \ + \ 2\left|\chi_{nr}^{(2)}\right|\left|\chi_{res}^{(2)}\right|cos\phi \ + \ \left|\chi_{res}^{(2)}\right|^2\right) \ \left|\vec{E}_{vis}\right|^2 \left|\vec{E}_{IR}\right|^2 \quad (2.32)
\end{aligned}
$$

ϕ is the phase angle between the complex quantities $\chi_{nr}^{(2)}$ and $\chi_{res}^{(2)}$.

For self-assembled monolayers on gold, a vibrationally non-resonant SFG intensity arises from the gold and $|\chi_{nr}^{(2)}|$ is significantly larger than $|\chi_{res}^{(2)}|$, which represents vibrational transitions in the adsorbate. Then (2.32) can be approximated by

$$
I_{SFG} \propto \left(\left|\chi_{nr}^{(2)}\right|^2 \ + \ \underbrace{2\left|\chi_{nr}^{(2)}\right|\left|\chi_{res}^{(2)}\right|cos\phi}_{interference}\right) \ \left|\vec{E}_{vis}\right|^2 \left|\vec{E}_{IR}\right|^2 \quad , \ \left|\chi_{nr}^{(2)}\right| \gg \left|\chi_{res}^{(2)}\right| \quad . (2.33)
$$

As the interference term can take positive and negative values, peaks in SFG spectroscopy appear positive or negative on the non-resonant substrate signal. From the expressions (2.12) and (2.33) it follows that the amplitude of the resonance in the SFG spectrum is proportional to the density N of the adsorbed molecules. If the relative intensities for different vibrations of the adsorbate changes, or if the peaks even change their sign, information on reorientation of the chemical groups in the adsorbate might be obtained [11, 12].

When the non-resonant substrate signal is negligible as in the case of polydimethylsiloxane (PDMS) (see chapter 5) the SFG spectrum is governed only by the resonant second order susceptibility:

$$
I_{SFG} \propto \left|\chi_{res}^{(2)}\right|^2 \ \left|\vec{E}_{vis}\right|^2 \left|\vec{E}_{IR}\right|^2 \quad , \ \left|\chi_{res}^{(2)}\right| \gg \left|\chi_{nr}^{(2)}\right| \quad . (2.34)
$$

The SFG signal for this case is proportional to N^2 (eq. 2.12).

2.5 Coverage dependence of the SFG signal

In this section it will be discussed, how the non-resonant and resonant contributions to the effective first order nonlinear susceptibility $\chi^{(2)}$ (2.27) give rise to electronic and vibrational contrast in sum-frequency microscopy (SFM). These two contrast mechanisms
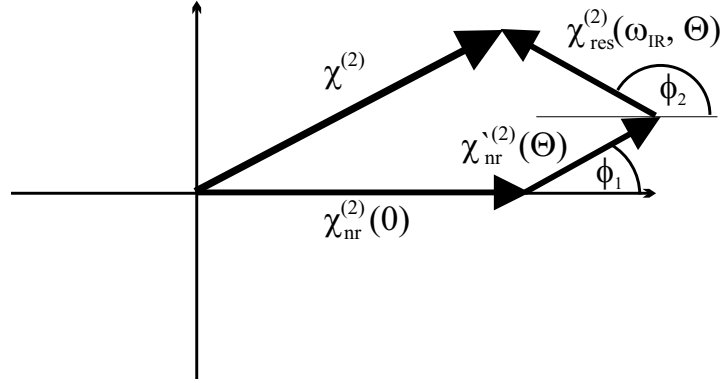
Figure 2.6: Schematic of the total first order nonlinear susceptibility $\chi^{(2)}$ for thiols on gold.

will be used in SFM to monitor the adsorbate density of thiolates on gold and to do surface specific chemical imaging (chapter 4).

According to (2.32) the SFG intensity I_{SFG} for a fixed experimental geometry depends on the first nonlinear susceptibility:

$$I_{SFG} \propto \left| \chi_{nr}^{(2)} + \chi_{res}^{(2)} \right|^2 \qquad . \tag{2.35}$$

The non-resonant effective second order susceptibility $\chi_{nr}^{(2)}$ as well as the resonant $\chi_{res}^{(2)}$ are functions of the adsorbate coverage Θ. Thus (2.35) is written more precisely as

$$I_{SFG} \propto \left| \chi_{nr}^{(2)}(0) + \chi_{nr}'^{(2)}(\Theta) + \chi_{res}^{(2)}(\omega_{IR}, \Theta) \right|^2 \qquad . \tag{2.36}$$

It consists (Fig. 2.6) of the substrate contribution $\chi_{nr}^{(2)}(0)$, which changes by $\chi_{nr}'^{(2)}(\Theta)$ upon adsorption of the thiol, and a contribution $\chi_{res}^{(2)}(\omega_{IR}, \Theta)$ coming from the vibrations of the adsorbate.

For thiolates on Au $\chi_{nr}^{(2)}(0)$ is about an order of magnitude larger than any of the other contributions on the right hand side and the latter two can be treated as small quantities:

$$I_{SFG} \propto \left| \chi^{(2)} \right|^2 \approx \left| \chi_{nr}^{(2)}(0) \right|^2 + 2cos(\phi_1) \left| \chi_{nr}^{(2)}(0) \right| \left| \chi_{nr}'^{(2)}(\Theta) \right| + 2cos(\phi_2) \left| \chi_{nr}^{(2)}(0) \right| \left| \chi_{res}^{(2)}(\omega_{IR}, \Theta) \right| \tag{2.37}$$

The first term is a frequency and coverage independent term from the Au surface resulting from interband transitions in Au at the SFG frequency [13], the second is the coverage-induced change of the broadband signal (see section 4.6), and the third term represents the vibrational features of the adsorbates. ϕ_i with $(i = 1, 2)$ is the phase factor between the respective parts of the first order nonlinear susceptibility. For an SFG intensity I_{nr} measured outside any vibrational transition the third contribution

on the right hand side of (2.37) becomes negligible. Thus, from measurements under non-resonant and resonant conditions two values

$$\tilde{\chi}_{res}^{(2)}(\Theta) = 2cos(\phi_2)\frac{\left|\chi_{res}^{(2)}(\Theta)\right|}{\left|\chi_{nr}^{(2)}\right|} \approx \frac{I_{res} - I_{nr}(\Theta)}{I_{nr}(0)} \qquad (2.38)$$

$$\tilde{\chi}_{nr}'^{(2)}(\Theta) = 2cos(\phi_1)\frac{\left|\chi_{nr}'^{(2)}(\Theta)\right|}{\left|\chi_{nr}^{(2)}\right|} \approx \frac{I_{nr}(\Theta)}{I_{nr}(0)} - 1 \qquad (2.39)$$

can be determined, which measure $\chi^{(2)}$ at each position on the sample normalized to the value of the substrate. $\tilde{\chi}_{res}^{(2)}(\Theta)$ gives a chemical map for a specific molecular group and $\tilde{\chi}_{nr}'^{(2)}(\Theta)$ monitors the adsorbate density (more details in section 4.6).

When the clean substrate value $I_{nr}(0)$ is not directly accessible, it is replaced by the average of $I_{nr}(\Theta)$ in the images. Then the inclusion of the constant factor $2cos(\phi_i)$ allows the direct comparison of $\tilde{\chi}_{res}^{(2)}(\Theta)$ with the normalized peak height in the corresponding spectra.

Chapter 3

Development and setup of a sum-frequency microscope

In this thesis a sum-frequency microscope (SFM) capable of in-situ chemical imaging of interfaces has been developed. High electric fields are needed in order to achieve sufficient SFG intensity, such as those created by picosecond laser-pulses. The complete optical setup produces one beam of pulses at a fixed visible wavelength of 532 nm and another beam of laser pulses with a tunable wavelength. In this work infrared pulses were employed in order to use SFG as a vibrational spectroscopic technique (see section 2.4). The complete accessible range spans the wavelength interval from 410 nm to 10 μm and the setup therefore can also be used for spectroscopy of electronic transitions. Essentially the setup is based on the process of optical parametric generation (OPG) and amplification (OPA) starting from the third harmonic of a Nd:YAG laser.

The optical apparatus was completely re-installed and expanded at the Max-Planck-Institute in Stuttgart at the beginning of this thesis. It is similar to the one used before at the École Polytechnique Fédérale in Lausanne [7]. However, an additional amplifier for the fundamental laser beam was integrated in the setup. This led to the tripling of the IR energy per pulse. The spectral width of the generated pulses was narrowed by the implementation of a grating with 2400 lines/mm. As the control software of the CCD camera only runs under the Windows® operating system, the experiment control and the data acquisition software had to be written completely new. A substantial improvement in the long term stability of the output energy was achieved by the installation of a new climate control in the laboratory.

The optical setup is based on a design developed and extensively described by Krause and Daum [14,15]. Therefore especially theoretical aspects will be treated quite concisely in the description of the laser setup (section 3.1). The main part of this chapter (section

3.2) deals with our novel SFM design and its performance. Sum-frequency microscopy requires the measurement of low photon numbers. Hence the role of predominant noise sources will be discussed at the end of this chapter (section 3.3).

3.1   Laser setup

A schematic drawing of the whole laser system is shown in Fig. 3.1. The main parts of it are as follows:

3.1.1   Nd:YAG laser and generation of third harmonic generation

The generation of tuneable laser radiation starts from an active-passive mode-locked Nd:YAG laser (Continuum, PY-61C-20) that supplies pulses with a wavelength of 1064 nm (9398 cm^{-1}) at a 20 Hz repetition rate. Passive mode-locking is realized by a saturable absorber (Q-Switch I, Exciton) resulting in a pulse length of 35 ps [5]. An acousto-optical modelocker is used for active mode-locking. The oscillator is operated at a pulse energy of about 2.9 mJ. The pulse then is amplified in a one-pass amplifier. Pulse energies up to 60 mJ can be achieved. The final energy of the laser beam is fine tuned by adjusting the temporal delay between the flashlight triggers of the oscillator and the amplifier. Thus the parameters of the flash lights do stay constant and so does the temperature of the Nd:YAG rods. This avoids a change in beam divergence. The beam diameter is 9.5 mm and typical pulse energies are 25 mJ.

The fundamental frequency is doubled and finally tripled by type II KD*P crystals (deuterated potassium dihydrogenphosphate,KD_2PO_4) [16]. The third harmonic pulses with a wavelength of 355 nm (28193 cm^{-1}) have an energy of 3-3.5 mJ per pulse. Although higher energies are easily obtainable that value is sufficient to operate the OPG/OPA setup in saturation.

3.1.2   OPG/OPA for the visible and near infrared

The beam profile of the third harmonic beam is improved by a spatial filter to allow for a efficient parametric generation in the OPG/OPA setup consisting of two lithium borate crystals (LiB$_3$O$_5$, short LBO), cut for type I phase matching. These hygroscopic crystals as well as the one of the OPG/OPA for the mid-infrared are kept at a temperature of $50\pm1°$ C to prevent crystal degradation by humidity. By difference-frequency generation (see chapter 2.1) the pump beam at 355 nm produces a spontaneous parametric emission
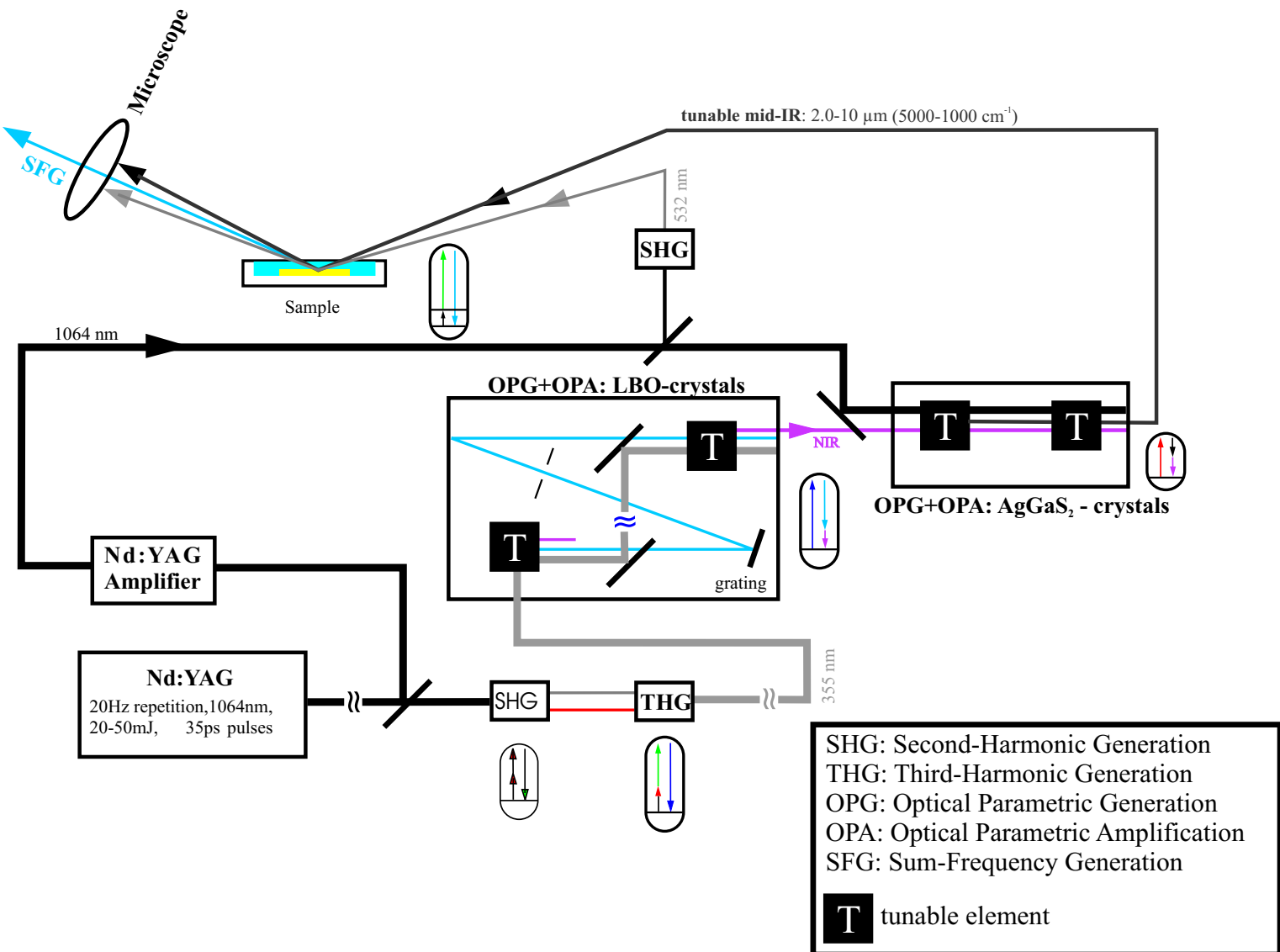
Figure 3.1: Schematic drawing of the optical apparatus that spans the wavelength interval from 410 nm to 10 μm. Details in the text.

in the first LBO crystal, which is then amplified by the second crystal. Energy as well as momentum are conserved in this conversion process. Signal and idler pulses at a defined wavelength are generated for a given tuning angle due to the anisotropic index of refraction in the LBO crystals [15]. Tuning the angle of both crytals is thus the method to change the wavelength. As the two crystals are turned in opposite directions, the offset of the involved laser pulses in each crystal is compensated. The spectral width of the generated pulses is due to the width of the seeding beam in the optical parametric amplification process [15]. Therefore its monochromaticity is enhanced by inserting a grating (2400 lines/mm, Jobin Yvon) and a slit between OPG and OPA. The achieved resolution is better than 10 cm^{-1} (see discussion in section 3.1.3). The obtainable wavelengths range from 4200 to 24000 cm^{-1}. The pulse energy of the signal at 22200 cm^{-1} combined with the idler, which is used for seeding the second OPG/OPA to obtain pulses with $\omega_{IR} \approx 2900$ cm^{-1}, is about 80 μJ. Depending on the wavelength the intensity varies slowly on the scale of $\sim$ 100s cm^{-1} [7].

3.1.3   OPG/OPA for the mid infrared

Chemical information in sum-frequency generation techniques is obtained from vibrational transitions of molecules. Vibrational spectroscopy in the interesting region of wavenumbers from 1000 to 4000 cm^{-1} demands for laser pulses in the mid infrared. For this goal the narrow band radiation generated in the OPG/OPA described above is used to seed a second OPG/OPA. It consists of two collinearly built up AgGaS$_2$ crystals, which are cut for type I phase matching and, which are pumped by the fundamental laser beam (9398 cm^{-1}). The wavelength is also changed by angular tuning. The output in an ideally seeded parametric generation and amplification process depends exponentially on the pump intensity, if exact phase matching and no pump depletion are assumed and if the seeding beam is much weaker than the pump beam [14]. Therefore an additional Nd:YAG amplifier was installed. 15% of the fundamental laser beam (1064 nm) is separated before the frequency tripling unit and then amplified by a factor $\sim$ 15. The beam size and divergence of the fundamental beam can be adjusted independently by a three lens telescope in front of the OPG/OPA. The maximum pump intensity at the entrance side of the first crystal is kept below ($\cong$0.5GW/cm^2), i.e. a factor of two below the damage threshold. The divergence overcompensates self focusing effects, which otherwise might lead to pump intensities above the damage threshold.

Again a signal and an idler component are generated by down conversion. The spectral range of the signal extends from 4700 cm^{-1} to 9400 cm^{-1}. The idler wavelength can be tuned between between 1700 cm^{-1} and 4700 cm^{-1}. By re-aligning the setup, also
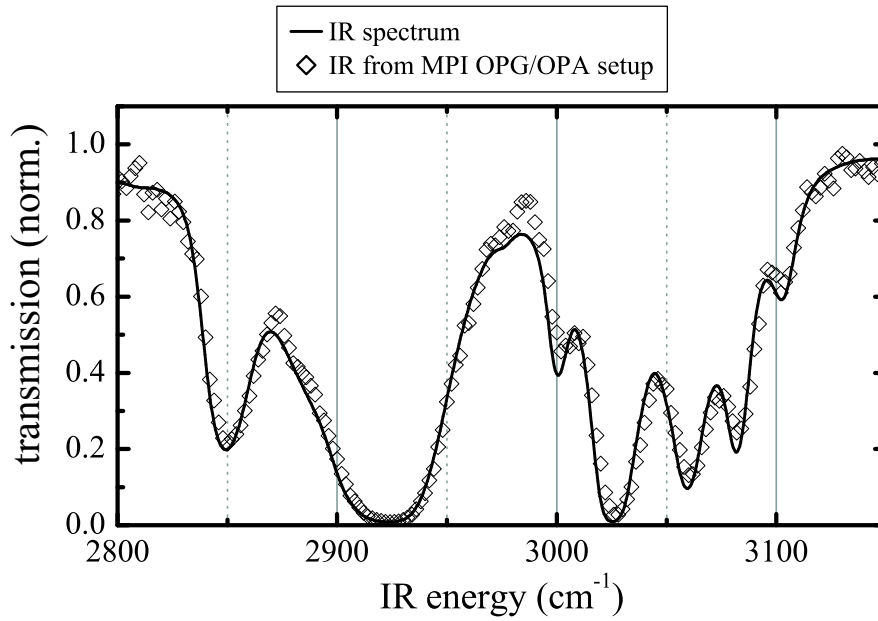
Figure 3.2: Transmission spectrum of a polystyrene foil measured with an FTIR spectrometer (line) and in the described setup (diamonds).

IR pulses at lower wavelengths down to 1200 cm^{-1} can be achieved although with very low pulse energies [7]. Either spectral component can be selected by appropriate optical filters. In the range of the CH vibrations, i.e. $\omega_{IR} \approx 3000$ cm^{-1}, typical energies are 250 μJ/pulse. Maximum energies are about 400 μJ/pulse.

The spectral width of the generated laser pulses is determined by the spectral width of the seeding beam unless there is broadband optical parametric generation in the AgGaS$_2$ crystals, which, however, is not observed for the given pump intensity. A limit of the spectral resolution can be given by comparing the IR transmission spectra of a polystyrene foil recorded with a FTIR spectrometer (resolution 4cm^{-1}) with the one obtained by using the IR output from the AgGaS$_2$ crystals (Fig. 3.2). Numerical convolution of the FTIR data with a width such that the result resembles the spectrum recorded with the output of the AgGaS$_2$ crystals yields a spectral resolution of $\Delta\omega_{IR} \approx$ 10 cm^{-1} in our setup. This agrees with the best resolved vibrational resonances, which have been measured (e.g. Fig. 4.4).

Due to slight differences in the aligning procedure of the whole optical apparatus (beam path $\sim$ 30 m) the absolute wavelength does not exactly equal the nominal wavelength. The absolute calibration of the IR is therefore done every day by recording a transmission spectrum of the polystyrene sheet and by comparing it to the reference spectrum, which gives the exact postion. This calibration is done with a precision ≤ 2 cm^{-1}.

Finally it turned out that the slit width in the LBO-OPG/OPA does not influence the spectral width significantly.

3.1.4   Wavelength control, data acquisition and ambient conditions

As already mentioned before, the wavelength is tuned by changing the angle of the OPG/OPA crystals and the grating position. This control as well as data acquisition and data display is done with a PC. The software has been developed as a part of this thesis. It connects the steering of the crystals with the CCD software and includes necessary aligning routines and the automatic acquisition of spectra. The sample can be positioned by a semi-automatic auto-focusing program. Evaluation software also written during this thesis comprise an automatic cosmic ray removal, the extraction of local spectra from a bigger frame and sophisticated binning processes.

Ambient conditions have a significant influence on the stability of the aligning and the energy output in the IR. The new installation of an air conditioning system, which keeps the temperature constant to $\pm 0.5°C$, proved to be crucial. Additionally it turned out that all optical beam paths need to be shielded against air currents by means of a curtain.

3.2   SFM: Design and characterization

3.2.1   General considerations

Nonlinear optics comprises a number of powerful techniques in material analysis and much effort is presently made to develop imaging methods that combine high spatial resolution with the specific properties of various nonlinear optical processes. Examples for recent efforts are improvements in coherent anti-Stokes Raman spectroscopy (CARS) microscopy [17], the increasing number of second harmonic generation microscopes all over the world, the construction of the first sum-frequency microscope [18], and first results in combining near field techniques with sum-frequency generation [19–21]. One basic advantage of processes, which involve more than one incident photon, is the fact, that the spatial resolution can be improved when compared with an equivalent linear process [22, 23]. In addition, high interface specificity can be obtained for second order optical processes, e.g. nonlinear processes like second harmonic generation (SHG) and sum-frequency generation (SFG).

In an SFG experiment, two intense light pulses are overlapped on a sample in time and space to generate light at the sum of the frequencies of the two light waves. In the electric dipole approximation, the generation is absolutely interface specific for centro-symmetric samples (chapter 2). Due to its nonlinearity, the process shows low efficiency and the incident beams have to be focused to get close to the corresponding sample dam-age threshold in order to minimize measuring times. In an SHG experiment, only one intense beam is incident on the sample and the doubled frequency is observed. Whereas the SHG signal for wavelengths typically shorter than 1 μm is often determined by elec-tronic transitions at the sample, the use of SFG with an IR and a visible beam allows vibrational spectroscopy in the IR thus providing chemical contrast from vibrational transitions (section 2.4).

SHG microscopy has been developed as a scanning method to study biological tissues [24] and sample inhomogeneities. It was developed further instrumentally to study one-dimensional diffusion of metals on metals [25] and became a full interface imaging technique [26]. Similar to CARS microscopy and in contrast to IR micro-spectroscopy both lateral resolution limit and detection efficiency of SFG microscopy (SFM) are due to the generated visible wavelength (e.g. around 450 nm) although it is sensitive to transitions, which correspond to wavelengths of some micrometers. It has been shown that in SFM, areas of different chemical composition or varying molecular orientation can exhibit contrast at characteristic IR wavelengths [18]. SFM thus combines in one instrument potential μm spatial resolution, sensitivity to even buried interfaces, chemical contrast, and – depending on the time structure of the employed incident beams – ns or ps time resolution.

In the literature, there are some promising first results in near-field SFG microscopy. Still, we decided to develop a far-field SFG microscope for several reasons: The SFG-intensity of interfaces or even submonolayers is generally very low, thus demanding integration over several laser shots. Taking images of larger areas (e.g. 100 x 100 pixels) by means of scanning will thus require long measuring times. Given the limit of surface damage, which restricts the power per surface area for the incident beams, lasers with low repetition rate (20 Hz) and high pulse energy ($> 100 \ \mu J$) like the one described in section 3.1 make it far more preferable to measure those pixels simultaneously and not in a pointwise scanning mode. Moreover, the quantitative interpretation of data becomes much more involved when near-field light sources or near-field detection are employed.

Although accessible by common laser equipment and in spite of its attractive prop-erties, to best of our knowledge only one IR-vis-SFG far-field microscope (SFM) has

been reported yet [27]. This may have to do with the low efficiency of the SFG process and the close angular and spectral proximity of the reflected visible beam and the generated SFG beam. The solution to overcome this problem in the above-mentioned SFM setup is the use of total internal reflection in the substrate for the incident visible beam, a solution that limits, however, the applicability to substrates, which are transparent in the visible, and excludes the important classes of metals and semiconductors. For these reflecting substrates, the illumination has to be made from the observation side of the sample by oblique incidence in order to obtain a high electric field component at the surface (section 2.3). For oblique incident beams, however, the most intense SFG component leaves the surface at a similarly large angle, which is determined by the two-dimensional wave vector conservation at a homogeneous interface.

Depending on exact geometry and wavelengths, this SFG light is emitted in a direction at most a few degrees away from the reflection of the incoming visible beam. Emission from regions breaking the translational in-plane symmetry of a sample, however, does no more obey wave vector conservation. SFG light of higher multipole order than electric dipole emission, which can be emitted by small aggregates, or SFG light carrying structural information from the sample (e.g. emitted near sample inhomogeneities), propagates in directions covering a large solid angle (Fig. 3.3). Sampling a substantial part of this light and obtaining full spatial information thus prohibits an angular separation of SFG light and reflected light from the incident beams, which is usually the basis for background suppression in coherent, specular SFG spectroscopy at interfaces. In the microscope setup the suppression relies on spectral filtering alone.

3.2.2   Microscope Design

Reflecting samples have to be illuminated by visible and IR light at incidence angles around 60° with respect to the interface normal in order to maximize the nonlinear Fresnel coefficients and thus the SFG intensity for the important ppp polarization combination, i.e. when incident and SFG beams are all p-polarized (section 2.3). Thus the zeroth order coherent SFG beam leaves also at angles near 60° in a direction close to the reflected visible beam. This means that this most intense SFG beam will enter the entrance lens of a conventional optical microscope observing the sample along the surface normal only close to the lens edge if at all. At the same time the objective will obstruct the incoming visible and IR beams. Aligning the imaging optics along the axis of the zeroth order SFG signal, however, will yield a focus only along one line while sample regions in front of or behind the focal plane will be out of focus in the image plane. As the depth of field decreases with a growing numerical aperture while
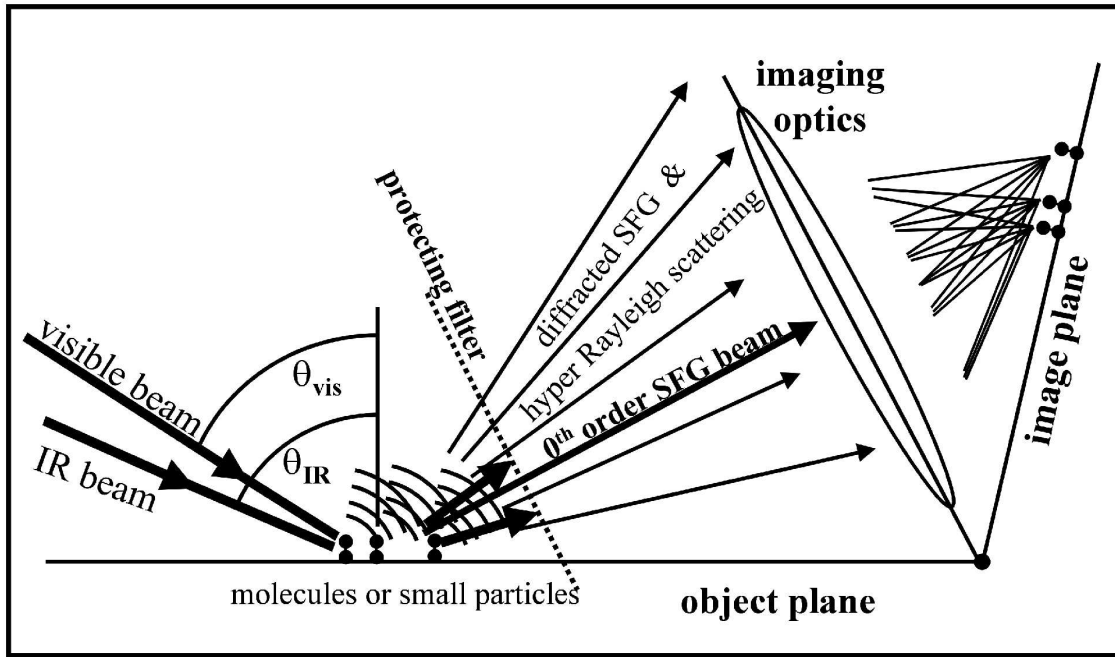
Figure 3.3: Principle of SFG microscopy. In contrast to "classical" SFG spectroscopy not only the specular beam is observed. Diffracted beams contain the light emitted by point-like sources and carry the information of sample inhomogeneities.

the spatial resolution increases, both quantities cannot be maximized simultaneously.

A possible solution is suggested by the Scheimpflug principle. It states, that an object is imaged in focus, if object plane, lens plane and image plane share an intersection line. A special case is the conventional photo-camera, of course, where those planes intersect at infinite distance. If the optical axis lies at a non perpendicular angle with respect to the object plane, the image plane has to be tilted correspondingly (Fig. 3.3). While the image is undistorted in the case of 1:1 magnification the distortion grows with increasing magnification. Furthermore the angle between optical axis and image plane soon approaches 0° [28]. Thus a magnification of e.g. 50x is experimentally not feasible.

Another hypothetical solution to overcome these constraints would be the use of a sample with a zigzag surface similar to a grating with a blaze angle of 30° and facets of <1 μm height. From each facet the SFG zeroth order light is emitted right into the objective, which is observing the grating from above while the whole surface stays within the depth of focus of the objective. Of course, such a concept would impose unacceptable restrictions on sample geometry. Additionally the Fresnel factors would be reduced because the angle of incidence would be only 30° on the facets.

A combination of both ideas solves the task to image the sample in focus with a good resolution and at an angle of 60° (Fig. 3.4a): Light originating from a flat surface

or interface is projected without magnification onto a blazed grating (see imaging path in Fig. 3.4b). This image is then magnified by a microscope whose axis is perpendicular to the macroscopic surface of the grating. The grating thus has to be placed in the image plane of the non-magnifying 1:1 system as well as in the object plane of the 50x microscope system. Its blaze angle is 30° so that the light emitted from one point of the sample is reflected into the microscope objective (Fig. 3.4b). In addition, its grating constant must be such that SFG light from the surface is diffracted in first order by the grating towards the microscope objective (illumination path in Fig. 3.4c). The essential components of the SFM will be described in the following paragraphs.

The construction aims at observing the SFG signal generated by a 532 nm visible light pulse with IR light from the narrow band optical parametric generator and amplifier (OPG/OPA) setup covering the important region of vibrational transitions between 1000 cm^{-1} and 4000 cm^{-1} (10 - 2.5 μm). Restricting the aim to spectroscopy in the range of 2.9 μm - 4 μm, the SFG signal will have a wavelength between 450 nm and 470 nm. The setup can in principle be extended to a larger IR region and allows also difference-frequency generation (DFG) for the same IR range after exchanging some of the spectral filters and the grating. For 450 nm SFG wavelength, a 1800 lines/mm grating (blaze 500 nm; supplier: Jobin-Yvon) was chosen. Two f = 58 mm, f/1.2 Noct-Nikkor objectives with aspherical lenses (supplier: Nikon) are used for the 1:1 imaging of the sample onto the grating. The 50x microscope consists of an LPlan 50x / 0.45 objective (Nikon) with 17 mm working distance and a tube lens. Apart from keeping perfect focus, the setup has another important property, namely, that the image of a sample appears on the CCD as if the sample is directly observed from above, i.e. a square on the sample becomes a square in the image. It allows obtaining undistorted images in spite of observation from the side. The aligning procedure is described in detail in Appendix A. After having developed and tested the design we became aware of a proceedings contribution by J.C. Chastang [29], which analyzes the properties of oblique imaging via a grating and proposes the scheme as a microscope attachment already in 1983. A publication on an application of this scheme was not found, however.

The intense visible and IR beams incident on the sample in an SFG experiment are to a substantial percentage reflected from a metallic or semiconducting sample. It is generally not difficult to attenuate the mid-IR beam (3 μm - 10 μm) because most optical components in a microscope have a vanishing transmission in this range. In contrast, one cannot avoid that the reflected beam at 532 nm will exhibit a tight focus within the glass components of the objectives and can thus easily damage the imaging optics. One can estimate that an attenuation of > 4 orders of magnitude for this beam
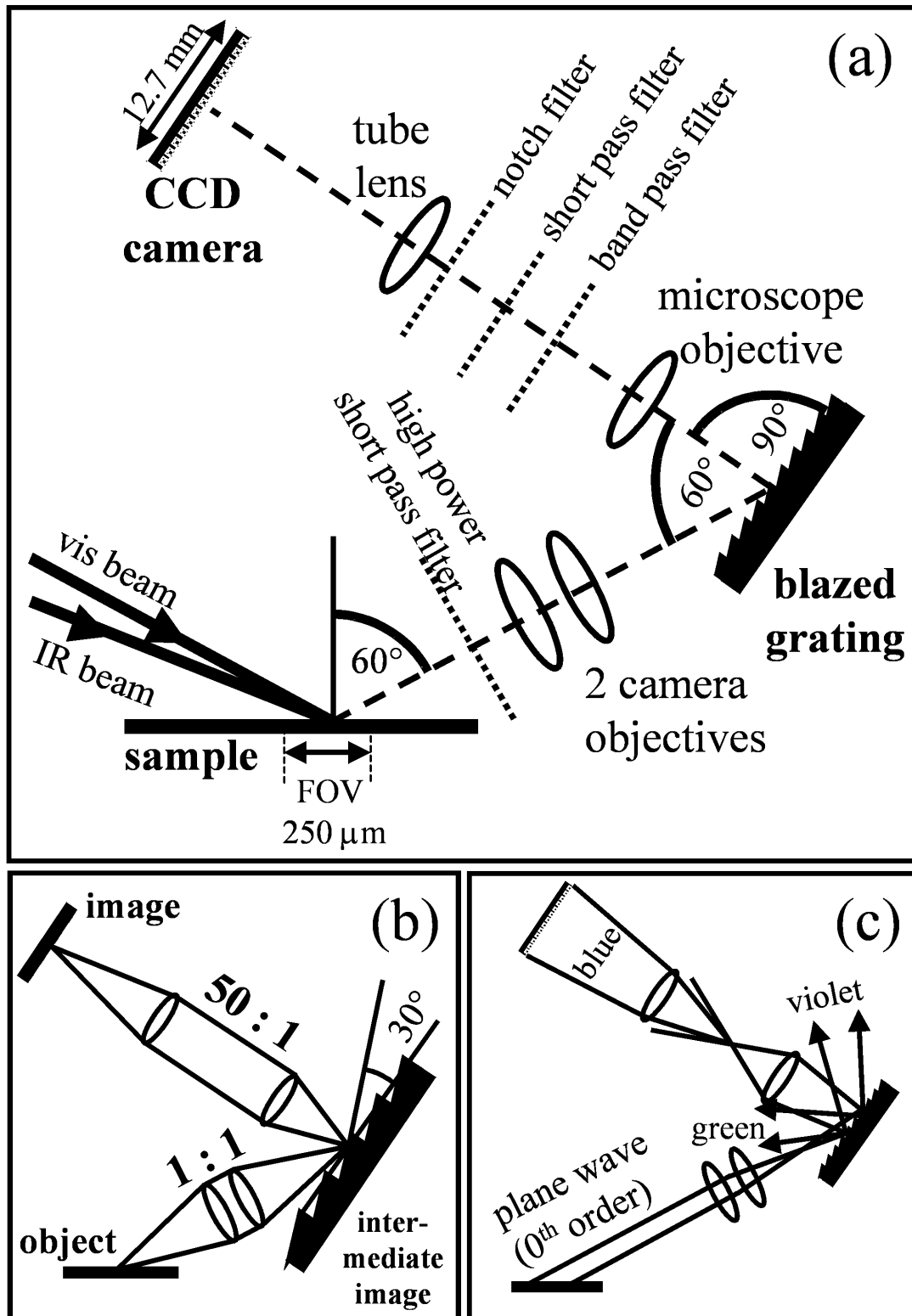
Figure 3.4: (a) Schematic setup of the SFG microscope with the employed optical elements. (b) Path of the imaging beam. (c) Path of the illumination beam.
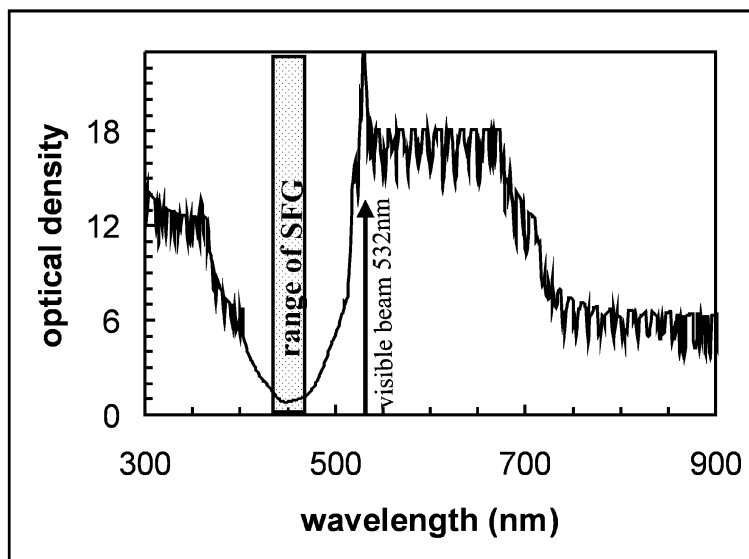
Figure 3.5: Synthetic absorption curve of the four-filter-combination discussed in the text. The curve is the sum of four absorbance curves measured for the individual filters. Due to the limited sensitivity of the spectrometer optical densities larger than 5 may be underestimated in this plot and may in reality be larger.

is necessary already in front of the first objective. This is accomplished by a low-cost dichroic short pass interference filter (edge 460 nm; Linos Photonics), which itself is not damaged by the intense visible beam and transmits > 80% of the SFG signal.

The suppression of stray light from various sources is an important point given the small intensity of the SFG signal. As a general measure, the whole setup is covered by a box made of black cardboard, which admits light only along the imaging beam path. Apart from diffuse light originating from room illumination it is sample luminescence and especially the reflected visible beam, which must be attenuated by several orders of magnitude in order to become negligible with respect to the SFG signal. A basic attenuation along the beam path is obtained by a holographic notch filter (center 532 nm, width 10 nm; Kaiser Optical Systems Inc.), which removes almost 5 orders of magnitude of the visible beam while letting pass 70% of the SFG signal. A further combination of a band pass filter (450 nm, width 40 nm; L.O.T.-Oriel) and a short pass filter (edge 510 nm, Omega Optical Inc.) suppresses both shorter wavelengths from ambient light, to which the CCD is still sensitive, and longer wavelengths, which may be efficiently generated by luminescence of the sample. These interference filters are inserted in-between the microscope objective and the tube lens, where all light beams propagate at a minimum angle with respect to the optical axis (Fig. 3.4a). The effective wavelength-dependent

transmission of the combination of the 4 filters discussed above is shown in Fig. 3.5 for the sensitive spectral range of the CCD camera.

The visible incident beam at 532 nm is suppressed by more than 20 orders of magnitude while about 30% of the SFG signal near 450 nm is transmitted. An additional significant attenuation of wavelengths longer or shorter than the SFG signal is due to the blazed grating (Fig. 3.4c). If required for certain cases, the setup can be turned into the setup of specular SFG spectroscopy without sacrifice of sensitivity by complete binning of the obtained image and replacing the first filter between sample and objective by a pinhole, which removes the specular SFG beam by angular filtering.

The desire for high quantum efficiency for photon detection and low noise led to the choice of a back-thinned, liquid N_2 cooled CCD camera. It consists of a grade 1 SITe chip with 512 x 512 pixels of 24×24 μm^2 area each, integrated in a camera built by Roper Scientific. Depending on the SFG intensity a gated intensifier can be mounted in front of the CCD chip (section 3.2.4). In order to use optimal instrumental resolution, the pixel size should be at least two times smaller than the limit given by the imaging optics (Nyquist Theorem). Depending on the objectives used, one may expect a resolution down to 1 μm. Thus a magnification factor of 50 is appropriate because one pixel then represents an area of 0.5×0.5 μm^2 on the sample. The total field of view seen by the CCD is 250×250 μm^2, which is adequate for many types of interface studies. Further magnification will be disadvantageous given the operational limitation by sample damage that sets a limit to the absolute number of photons, which can be emitted for a given sample, surface area, and pulse duration. A number for the experimental conditions will be given below.

3.2.3 Evaluation of the microscope performance by test structures

The properties discussed in the following paragraphs are not essentially different for linear and nonlinear optics but they are obtained much faster in linear optical experiments. Thus the optical system was characterized in the beginning by images of calibrated test structures (NBS-test No. 29, supplier: Heidenhain), which were illuminated by monochromatic blue incoherent light ($\lambda = 450 \pm 5$ nm). The initial characterization was performed with the CCD setup without intensifier.

An omnipresent and rather trivial reduction of image quality is due to local flaws in spectroscopic filters, grating inhomogeneities, and, finally, small dust particles on different optical components in the beam path. For linear optics imaging, Fig. 3.6
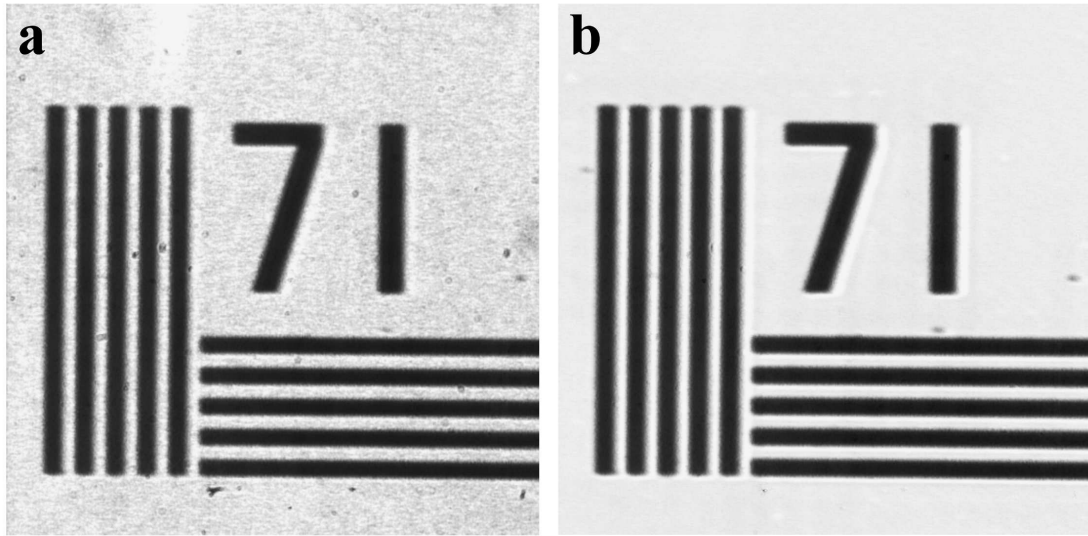
Figure 3.6: Examples of the reduction of grating and filter inhomogeneities: (a) raw image. (b) the same image after normalization to an average of blank images (also see the text)

shows that most of these spots can be removed by dividing the image by an average of some twenty images taken on different parts of a homogeneous sample. In this thesis that type of general flat field correction by an average of linear optical images has been applied to all linear images and most of the SFG images. A second problem arises specifically at extremely low light levels, as in SFG imaging: The number of cosmic ray events in an exposure can become important for exposure times of several minutes. Each such event affects mostly 2, rarely up to 4 pixels (see e.g. Fig. 3.10b) and is stochastic in the sense that it affects different pixels in successive exposures. The spurious count rates can thus be removed simply by comparison within a series of exposures under the same conditions.

Magnification – Distortion-free imaging

Fig. 3.7a shows horizontal lines of a 22 linepairs/mm structure. The image allows evaluating the magnification in vertical direction in several regions of the image field assuming a pixel distance of precisely 24 μm. The result is displayed in Fig. 3.7c. In this figure the magnification values are printed in the region equivalent to the region where they have been obtained in the original image Fig. 3.7a. Equivalently, the vertical lines in Fig. 3.7b are used to obtain the magnification in horizontal direction (Fig. 3.7d). This evaluation yields an average vertical magnification factor of 50.3 ($\pm$ 0.5) and a horizontal magnification factor of 51.1 ($\pm$0.5). The error corresponds to an uncertainty
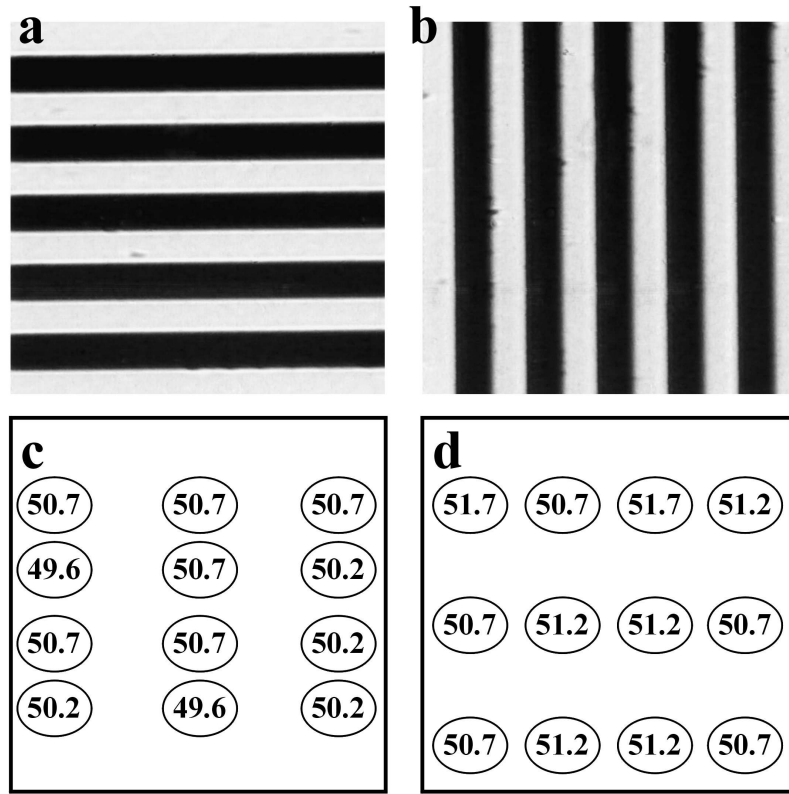
Figure 3.7: Determination of image distortion. Top: Image of a 22 linepairs/mm structure (a) for horizontal lines, (b) for vertical lines. Bottom: Values obtained by evaluating the magnification in different parts of the images (c) for the vertical magnification, (d) for the horizontal magnification. The magnification values are printed in the region of the box equivalent to the region where they have been obtained in the images (a) and (b).

of one pixel. Within this precision the imaging is distortion-free.

Figs. 3.7a and b also show that the edges of the stripes stay focused in the entire image and do not become blurred with increasing distance from the image center. This fact is non-trivial for the horizontal direction because the left edge of the images is 208 μm closer to the objective than the right edge. For comparison, focusing is done by approaching the sample to the first objective and must be done with < 3 μm precision.

Spatial Resolution

Fig. 3.8a shows an image of a test structure with 110 linepairs/mm, which are still well resolved. Analyzing the images of still smaller structures allows to find the resolution limit. It was verified by numerical convolution that the resolution defined by the Rayleigh criterion is given by the period of the striped structure, which exhibits 8% of the intensity modulation of a perfectly well resolved structure (see also [30]). By
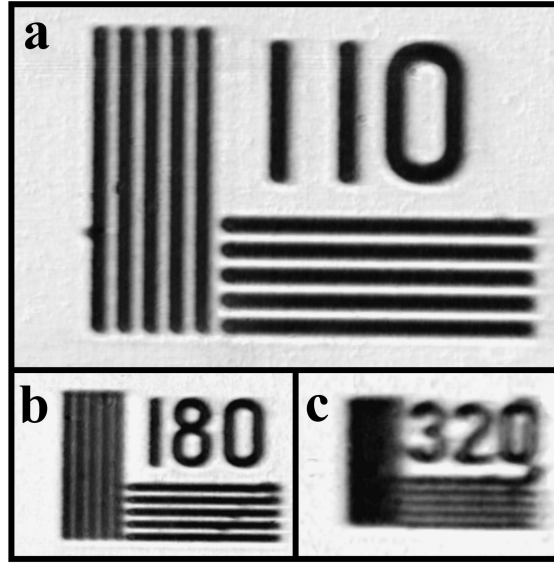
Figure 3.8: (a) Well-resolved test pattern (110 linepairs/mm); (b) resolution limit for vertical lines: 180 linepairs/mm; (c) for horizontal lines: 320 linepairs/mm

interpolating a series of images for different stripe periods one finds that this limit is reached for the horizontal resolution at 4.9 μm (approximately the period of vertical stripes in Fig. 3.8b) and for the vertical resolution at 2.8 μm (approximately the period of horizontal stripes in Fig. 3.8c).

The anisotropic resolution is a consequence of oblique imaging. It results from the fact that a square on the sample appears as a rectangle when observed from the direction of the first objective. The apparently shorter distance in the square creates a diffraction pattern, which leads to beams under larger angles than the apparently longer distance. It is for this reason that the camera objective, which lets pass a circular section in reciprocal space, can still transmit the first order diffraction of the apparently larger distance while it already misses the first order of the apparently shorter distance. From this reciprocal space argument one expects the ratio between vertical and horizontal resolution to be $\cos(60°) = 0.5$ in reasonable agreement with the experimental result.

A simulation of the oblique imaging reproduces the anisotropic resolution (Fig. 3.9) as shown for point-like structures. The object consists of light emitting points in the object plane O. The field amplitude A_{lens} can be calculated for each point of the lens at the distance $\delta_{obj\to lens}$ from the object:

$$A_{lens} = \sum_{objects} A_{obj}\ exp\ \left(i2\pi\frac{\delta_{obj\to lens}}{\lambda} \right) \qquad (3.1)$$

The intensity I_{image} can be determined by an integral over the lens: The integral over the lens plane was replaced by a discrete sum over 2000 points randomly distributed at
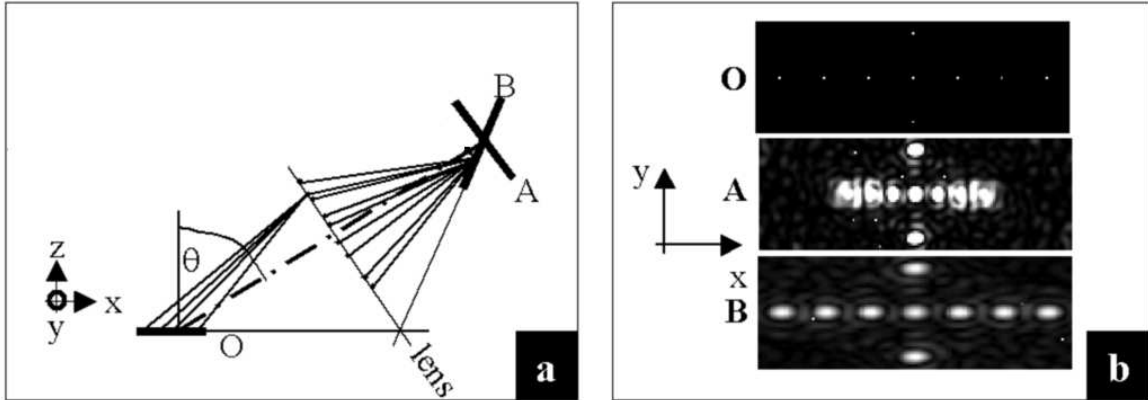
Figure 3.9: (a) Model of anisotropic resolution in the 1:1 imaging process: (b) (O) object plane, (A) calculated intensity in a plane perpendicular to the optical axis, (B) calculated image in the plane of the grating

the lens position (Fig. 3.9a).

$$I_{image} = \left(\sum_{points} A_{lens} \; exp \; \left(i2\pi \frac{\delta_{lens \to image}}{\lambda} \right) \right)^{2} \tag{3.2}$$

The lens is assumed to be perfect. The first simulation shows the image in the plane perpendicular to the optical axis (A). The points on the vertical line in the central field of view are in focus. They are broadened by diffraction due to the finite lens aperture. Points closer to or further away from the objective are out of focus. Fig. 3.9b (B) shows the simulation for the Scheimpflug configuration used in the SFM. The whole field of view stays in focus. The anisotropic resolution is reflected in an elliptic diffraction pattern of the single points. As expected, the ratio of the resolution in the simulation is equal to $\cos{(\theta = 60°)} = 0.5$. The experimental result is 0.6, which is in fair agreement. The simulation is based on a diffraction-limited system. Introducing spherical aberrations of the lens in the simulation reduces the resolution but leads to a similar elliptic, i.e. anisotropic point spread function.

In experimental practice it should often be possible to rotate the sample in a way to make use of the better resolution.

The diffraction limited resolution Δx at $\lambda = 450$ nm derived from the Abbe formula $\Delta x = 1.22 \, \lambda/NA$, in which NA is the numerical aperture, is $\Delta x = 0.92 \, \mu$m for the camera objectives (NA = 0.6) and $\Delta x = 1.22 \, \mu$m for the microscope objective (NA=0.45). The result for the resolution does not attain this limit. As an intermediate image is created on the grating the worse of the objectives will determine the overall resolution.
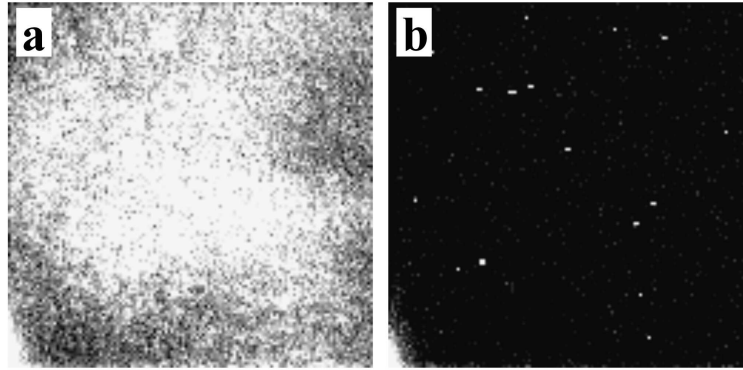
Figure 3.10: Proof of background suppression: Uncorrected raw data with 5 minutes exposure time, 4x4 pixels binned. (a) SFG intensity from a GaAs sample; (b) same conditions but with the visible beam delayed by 50 ps with respect to the IR beam. The intensity scales for both images are identical. White pixels in (b) are due to cosmic rays. The bright spot in the lower left corner is due to an inhomogeneity of CCD dark current.

Experiments in which both systems were tested separately showed clearly that the microscope objective almost reaches its diffraction limit while one single camera objective only attains a resolution of about 4 μm at $\lambda = 632.8$ nm. This demonstrates that the resolution in the setup is due to the fact that the camera objectives do not reach the diffraction limit. This result might suggest that a substantially smaller aperture can be used for the 1:1 projection. The large aperture size is, however, useful in order to collect a maximum of light emitted from strongly inhomogeneous samples as it has been discussed already in the introduction.

Performance for sum-frequency generation

So far the optical performance of the microscope itself has been characterized. Its performance for the SFG method will be demonstrated in the remainder of this section. As pointed out earlier the damage threshold of a sample ultimately limits its SFG photon yield. A good SFG microscope will detect a large amount of the generated photons. Typical integration times for laser intensities below this limit will be given for the 35 ps 20 Hz laser pulses generated by the laser setup described in section 3.1. Pushing the damage threshold by using higher repetition rates and shorter pulses each containing less energy will reduce the necessary measuring times.

Fig. 3.10a gives an example for the observation of a sum-frequency signal for the microscope setup with coincident 532 nm (visible) and 3.4 μm (IR) pulses. The energy of the 35 ps laser pulses employed for the SFG measurements in this chapter are typically 200 μJ/pulse in the visible beam at 532 nm slightly focused to a large spot of 4 mm^2
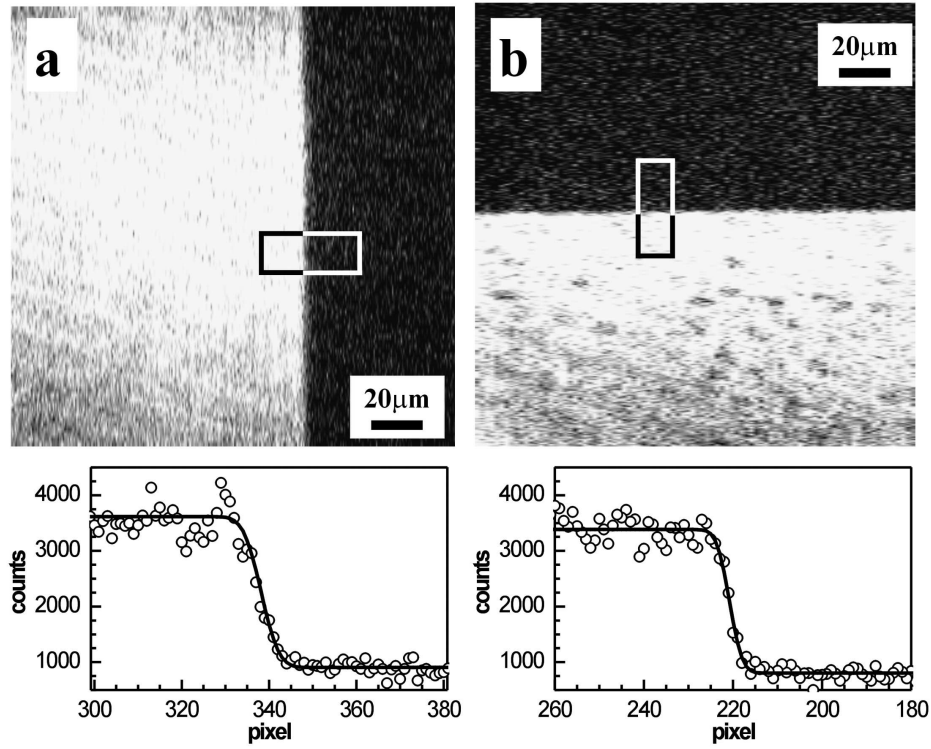
Figure 3.11: Resolution in an SFG image: (a) for a vertical and (b) a horizontal edge of a GaAs sample. The exposure time was 120 minutes. In the measurements, four pixels parallel to the edge were binned keeping the resolution perpendicular to the edges. At the bottom the average of 8 line scans in the boxed area are shown together with the fits discussed in the text.

and 250 μJ/pulse in the IR pulse at 3.45 μm (2900 cm^{-1}) focused to about 0.1 mm^2. Both beams have to overlap in time and have to be adjusted to the sample area imaged by the microscope. The observed SFG signal generated by a GaAs sample corresponds to 3.4×10^6 photons detected by the CCD chip during an exposure of 300 s (6000 laser shots). An array of 4×4 pixels was binned to one pixel in order to reduce the read-out noise (see subsection 3.3.1). The detected average intensity is 2.6 photons per minute originating from a $(0.5~\mu m)^2$ area. The intensity in the center of Fig. 3.10a is 3.7 photons per minute per $(0.5~\mu m)^2$. Higher intensities could not be obtained without damaging the GaAs sample. The intensity distribution in the image is due to the visible and IR beam profiles.

As expected for an SFG process, the observed intensity disappears completely when either the visible or the IR beam is blocked. Fig. 3.10b proves furthermore that no light is observed when both beams are incident but the visible pulse is delayed by 50 ps with respect to the IR pulse (pulse length 35 ps). This demonstrates the absence of background and luminescence light in the image.

In order to verify the anisotropic resolution also for oblique SFG imaging, an image of the edges of a GaAs wafer broken along a defined crystallographic direction was made. Such edges are known to be straight and sharp on a sub-μm scale. In the case of GaAs the observed SFG signal is dominated by the bulk contribution.

Already on first inspection of Fig. 3.11 the SFG image shows sharp imaging without signs of defocusing at the edges of the image field and a better resolution in vertical than in horizontal direction. In both measurements, four pixels were binned in a row parallel to the respective sample edge. As the edges are parallel to the rows of the pixels this type of binning reduces the read-out noise without reducing the resolution in the direction perpendicular to the respective edges. Fitting an error function (erf) to an average of 8 such line scans yields as a distance between the 10% and the 90% intensity level a value of 4.6 μm for the vertical and 2.9 μm for the horizontal edge. This corresponds to a resolution according to the Rayleigh criterion of 4.9 μm in horizontal and 3.1 μm in vertical direction in good agreement with the above results obtained by linear optics experiment.

3.2.4   Intensified CCD

The data presented so far, have been recorded directly with the CCD chip. Therefore the setup is very sensitive to background light. Especially this influence can be efficiently reduced by the use of an image intensifier (Gen II, S20 cathode, manufacturer: Roper Scientific).

Figure 3.12 shows the schematic design of such an intensifier. A photon that hits the input multi-alkali photocathode leads to the emission of an electron with a probability given by the quantum efficiency QE of the cathode material. The electron is then accelerated towards the electron-multiplying microchannel plate (MCP) by a bias voltage of ~ 200 V . In the MCP, high voltage (~ 800V) leads to further acceleration and multiplication of the electron number producing secondary electrons by electrons hitting the walls of the channels. The electrons exiting the MCP are accelerated by a constant voltage of 8 kV and strike the phosphor screen, where they are converted to photons again. One detected photon is converted into ~ 1000 photons. The multiplying factor displays some scatter, as will be described in the next subsection.

In gated mode operation the high voltage is always applied to the MCP and the phosphor screen. Only the voltage between the photocathode and the MCP is switched from positive to negative bias. For a positive bias the electrons cannot reach the MCP, the intensifier is turned off. As the switching voltage is only 200 V gating can be done at very high speed and the gate-controller (PG200, Roper Scientific) allows for gate widths
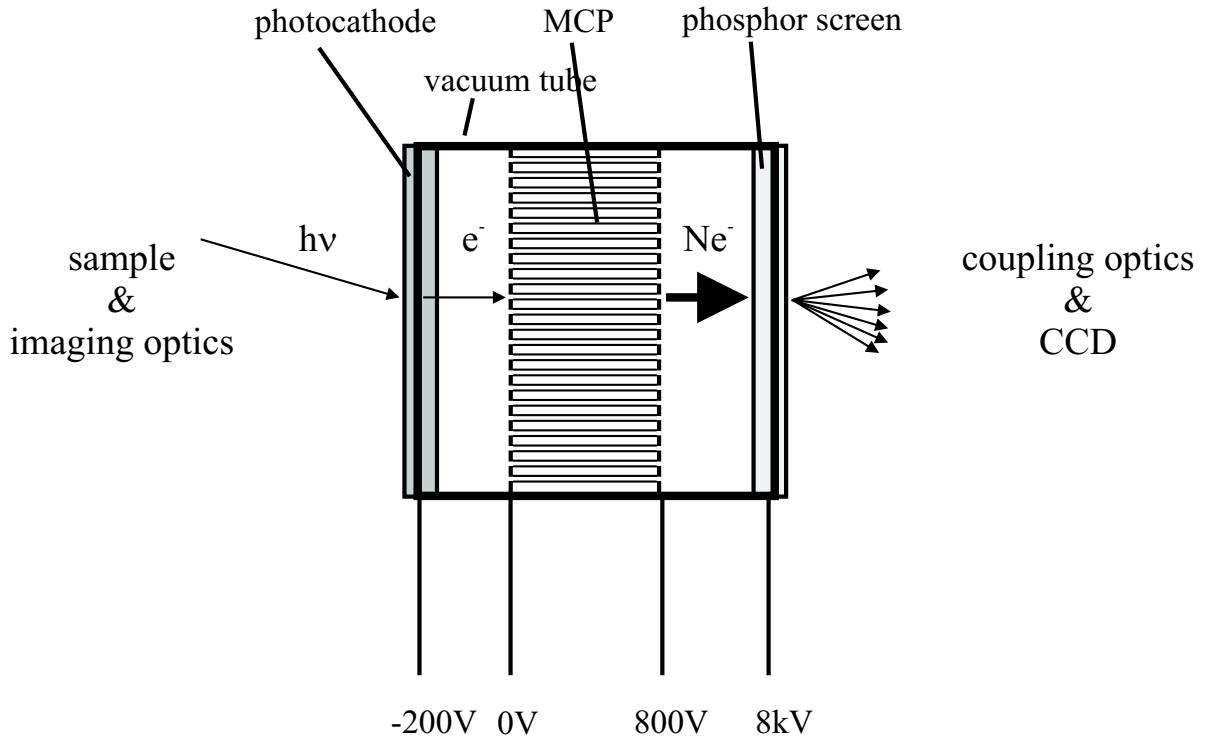
Figure 3.12: Schematic design of the image intensifier.

down to $t_{gate} = 5$ ns.

The gate is triggered by the laser pulse when it leaves the laser. Usually a gatewidth of $t_{gate} = 100$ ns is employed with a minimum delay of 30 ns. This gatewidth and delay guarantees, that the voltage of the MCP is at its maximum when the signal arrives. For a laser repetition rate of 20 Hz this corresponds to a background suppression of 20×100 ns/s=1/500 000 for light, which is not synchronous with the laser pulses (e.g. ambient light) or which is delayed (luminescence). In order to keep the setup as versatile as possible the MCP is coupled with a 1:1 two-lens-system to the CCD. These systems are known to impose a vignetting effect on the image [31], i.e. a homogeneously image appears brighter in the center than at the periphery. This can be corrected for by the flatfield procedure described in subsection 3.2.3. As a drawback the photocathode reduces the quantum efficiency QE for photon detection by a factor of about 5 when compared with the back-thinned CCD alone (Tab. 3.1).

Fig. 3.13 shows a horizontal and a vertical edge of GaAs taken at a wavelength of $\lambda = 450$ nm using the intensified CCD (ICCD) setup. Below the image the line indicated in the image is plotted. The vertical resolution is evaluated to be 3.2 μm. The horizontal resolution (Fig. 3.13b) is 5.1 μm. This is in good agreement (Tab. 3.1) with the results obtained without image intensifier (subsection 3.2.3). Thus the MCP does not reduce the spatial resolution significantly. The resolution is still limited by the
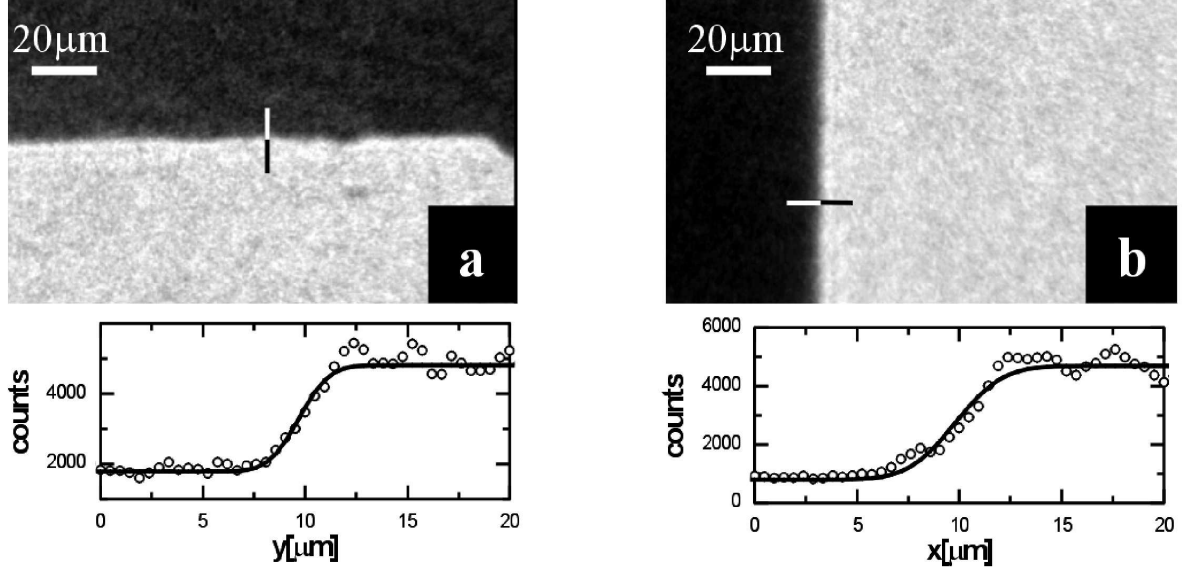
Figure 3.13: Linear optical images (λ = 450 nm) of (a) a horizontal edge of GaAs. The cross-section corresponds to the line drawn in the image. Vertical resolution: 3.2 μm. (b) a vertical edge of GaAs. Horizontal resolution: 5.1 μm

camera objectives used for the 1:1 optics. The manufacturer specifies the coupling optics with a 60 μm spot size FWHM on the CCD. For a magnification of 50 this corresponds to a resolution of $\sim$ 1.2 μm. Folding the resolution obtained for the GaAs edges with the SFM without intensifier (section 3.2.3) with this value yields a theoretical horizontal resolution of 5.0 μm and a vertical one of 3.2 μm. This agrees with the obtained result for the ICCD within experimental error.

	CCD	ICCD
vert. resolution (μm)	3.1	3.2
horiz. resolution(μm)	4.9	5.1
QE at the detector (λ=450 nm)	0.82	0.15

Table 3.1: Specifications of the SFM with and without intensifier. While the quantum efficiency QE differs significantly the spatial resolution is similar for both configurations.

3.3   Maximizing the SNR in SFG microscopy

Due to the low intensities, usually related to SFG microscopy, it is indispensable to maximize the obtainable signal-to-noise ratio (SNR) and therefore to consider the main

sources of noise. In the first section this will be done for the CCD in the second for the intensified CCD.

3.3.1 SNR in SFM using the CCD

For a scientific grade CCD there are three primary noise sources: Photon noise, read-out noise and dark noise [32]. Noise in this sense denotes the scatter in the intensity/pixel from frame to frame. The signal for the CCD is given in photons/pixel, which corresponds directly to electrons/pixel. Thus the noise has the unit (photons/pixel).

The flux, at which photons arrive at a fixed position, varies statistically. For a given photon flux Φ on average $\bar{n}$ photons are present in a time-interval Δt:

$$\bar{n} = \Phi \, \Delta t \tag{3.3}$$

The actual number of photons hitting the detector in the same time interval Δt at an arbitrary time will be n with a probability P(n), which is Poisson distributed for usual light sources [32]:

$$P(n) = \frac{\bar{n}^n}{n!} e^{-\bar{n}} \tag{3.4}$$

The number of detected photons in the same time interval is determined by the quantum efficiency

$$QE = \frac{number \ of \ detected \ photons}{incident \ photons} \quad , \tag{3.5}$$

which denotes the probability that an incident photon is recorded by the detector. The photon noise σ_{phot} of the measurements equals the square root of the detected photon signal $\bar{n} \times QE$:

$$\sigma_{phot} = \sqrt{\bar{n} \times QE} = \sqrt{\Phi \Delta t \times QE}. \tag{3.6}$$

As photon noise is inherent in the generation of light it cannot be reduced by camera design.

Read-out noise σ_{read} is electronic noise generated mainly in the amplification process of the signal in the CCD AD-converter. A σ_{read} of about 34 photons/pixel per readout was measured. If an image is recorded by adding m frames, the total readout noise is

$$\sigma_{read,m} = \sqrt{m} \sigma_{read} \quad . \tag{3.7}$$

The dark current I_{dark} stems stems from thermally generated electrons in the CCD chip. Dark current noise σ_{dark} is the statistical variation of this charge generation and it follows Poisson distribution. σ_{dark} is therefore given by:

$$\sigma_{dark} = \sqrt{I_{dark} \Delta t} \quad . \tag{3.8}$$

Under measuring conditions, i.e. when the CCD chip is cooled with liquid nitrogen to T = -120° C, I_{dark} is reduced to 1.62 e$^-$/pixel per hour[1]. Dark noise plays a negligible role in the applications in this thesis if compared with both read-out noise and photon noise.

Spikes due to cosmic rays constitute a substantial origin of noise in the raw data as their intensity corresponds to hundreds of photons. As they can be readily removed by comparing different frames acquired under identical conditions (section 3.2.3), they will not be considered here. For the intensified CCD their role is small anyway, as will be clear in the second part of this section.

Fig. 3.14a shows the signal-to-noise ratio for the CCD camera without intensifier as a function of time. The line shows the SNR calculated under consideration of the three noise contributions just described:

$$SNR = \frac{Signal}{Noise} = \frac{detected\ photons}{\sqrt{\sigma_{phot}^2 + \sigma_{dark}^2 + \sigma_{read,m}^2}} = \frac{\Phi \Delta t QE}{\sqrt{\Phi \Delta t QE + I_{dark}\Delta t + m\sigma_{read}^2}} \quad (3.9)$$

The photon flux Φ of 1 photon per pixel and minute is a value that is typically achieved in the measurements on Au substrates. The exposure time $t_{exp} = 10$ min is a tradeoff between low read-out noise and number of cosmic ray events. At first the case of no binning is treated. The triangles denote the SNR including only photon noise σ_{phot} while the circles represent the SNR if only read-out noise σ_{read} is considered. The latter case is almost identical to the exact value calculated with (3.9) (solid line).

At these low intensities the total SNR is dominated by $\sigma_{read,m}$. Therefore (3.9) can be approximated by

$$SNR \approx \frac{\Phi\ QE\ \Delta t}{\sqrt{m\sigma_{read}^2}} = \frac{\Phi\ QE\ \Delta t}{\sigma_{read}\sqrt{m}} =$$

$$\frac{\Phi\ QE}{\sigma_{read}} \times (\sqrt{t_{exp}}\ \sqrt{\Delta t}) \qquad .$$

(3.10)

In the read-out noise dominated regime the SNR scales as $\sqrt{t_{exp}}$ with the exposure time per frame and as $\sqrt{\Delta t}$ for longer acquisition times.

The first possibility to improve the signal-to-noise ratio by adjusting the recording parameters of the CCD is the use of longer exposure times. Fig. 3.14b (B) shows this $\sqrt{2}$ enlargement of SNR by doubling t_{exp}. A second and stronger effect has the binning of pixels to a "superpixel". The signal scales with the number n_{bin} of pixels binned together, while the read-out noise stays the same for the "superpixel". For a 2×2 binning this increase by a factor of 4 is shown in trace (C), which comprises all three

---

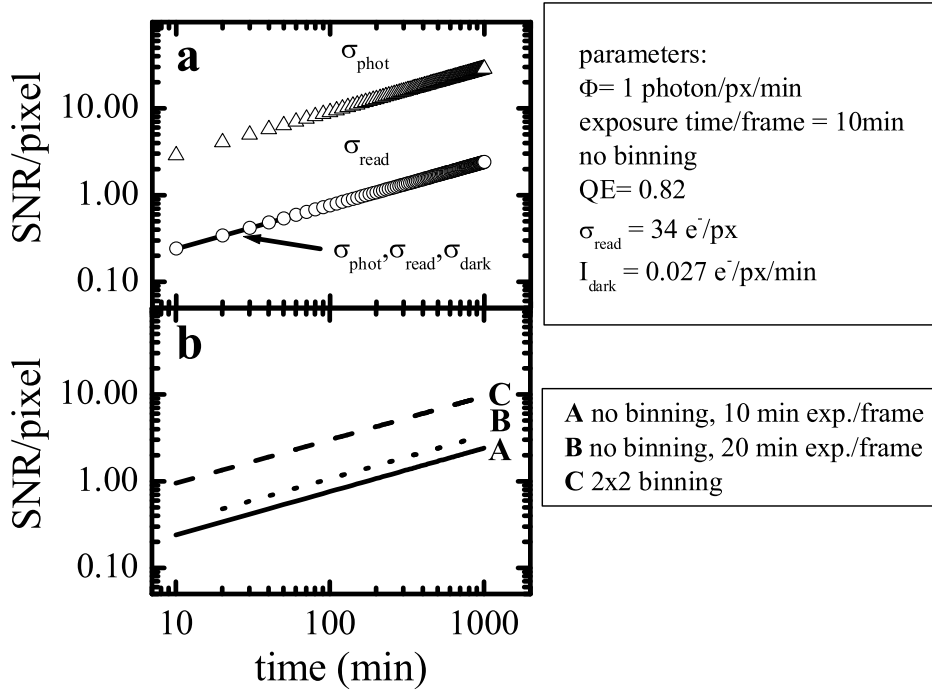[1]according to the data sheet of the CCD chip

Figure 3.14: Calculation of the signal to noise ratio for the CCD camera without intensifier: **(a)** (line) SNR calculated with eq. 3.9 and parameters given in the box. (circles) SNR with only read-out noise considered. (triangles) SNR with only photon noise considered. **(b)** (A) same data as in (a). (B) SNR for longer exposure times per frame. (C) SNR with 2×2 pixel binning

noise contributions. A 2×2 superpixel corresponds to an area of $\sim 1 \times 1$ μm^2 on the sample in the SFM setup. The Nyquist theorem is still fulfilled for the resolution of the SFM, which is > 2 μm. Therefore usually 2×2 binning is applied for taking SFM images. It is important to note, that the noise would increase as $\sqrt{n_{bin}}$ and such would the SNR, if the binning is done via software after the acquisition.

There are at least two further possibilities to modify the setup in order to reach the photon-noise limited case: First, there are laser systems on the market that have a repetition rate of ~ 2 kHz. Compared to the 20 Hz laser system used in this thesis this means an increase of the signal by a factor of 100 for identical pulse energies and total acquisition times. The impact on the SNR in sum-frequency microscopy will be demonstrated in chapter 7. There is no such laser at this institute but the microscope itself is mounted on a breadboard (70×60 cm^2), which allows making measurements also at different laser sources. The other possibility will be described now.

3.3.2   SNR in SFM using the intensified CCD

The use of an image intensifier can improve the SNR for low signals. An image intensifier produces ~ 1000 photons on the CCD for one incoming photon. So the contribution of the read-out noise becomes negligible. This comes at the cost of a lower quantum efficiency QE of the intensifier when compared with the bare CCD chip. In addition the multiplication factor for a single photon in the MCP scatters significantly as can be seen in Fig. 3.15: An image was taken at such low intensity that single photons could be spatially separated on the CCD chip. The histogram shows the distribution of counts, that are produced for one single photon. The fit of this distribution with a Gaussian yields a mean multiplication factor $M = 328$ counts/photon with a standard deviation $\sigma_M = 148$ counts/photon.
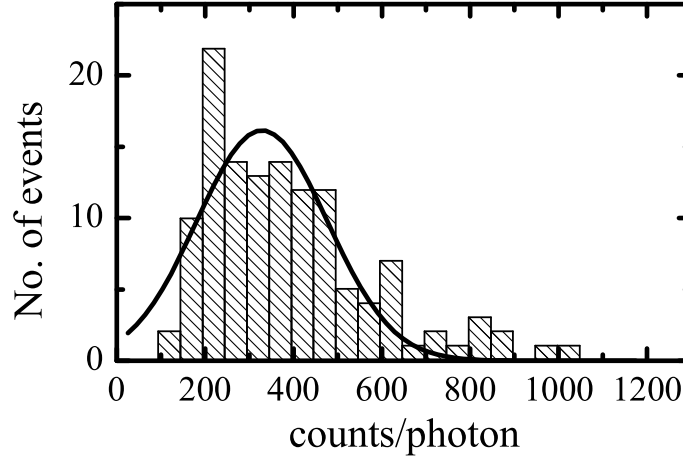
Figure 3.15: Histogram of the MCP multiplication M factor for single photons. The Gaussian fit (solid line) gives M = 328±148 counts/photon.

The signal S in units of counts/pixel is given by

$$S = \bar{n}\ QE\ M \qquad , \tag{3.11}$$

with an average number of detected photons

$$\bar{n}_{det} = \Phi\ QE\ \Delta t = \bar{n}\ QE \qquad . \tag{3.12}$$

The standard error is given by

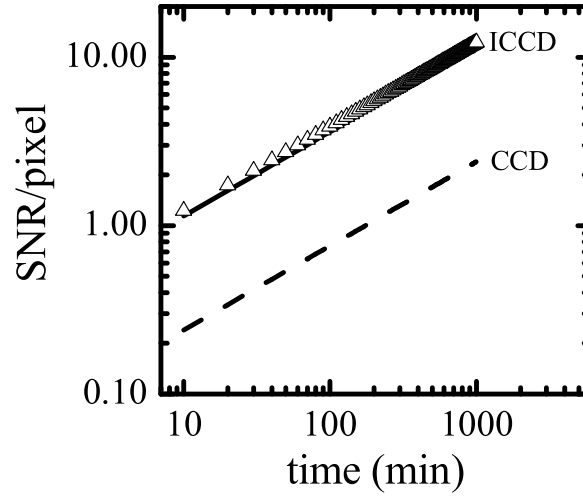$$\sigma_{n,det} = \sqrt{\bar{n}\ QE} \qquad . \tag{3.13}$$

Figure 3.16: Signal-to-noise ratios for ICDD and CCD using the same flux of photons (solid lines). SNR for the ICCD if only photon noise is considered (triangles).

Using the theory of error propagation the noise σ_S is obtained:

$$
\sigma_S = \sqrt{\left(\frac{\partial S}{\partial n_{det}}\right)^2 \sigma_{n,det}^2 + \left(\frac{\partial S}{\partial M}\right)^2 \sigma_M^2}
$$

$$
= \sqrt{M^2 \, \bar{n} \, QE \; + \; \bar{n}^2 QE^2 \, \frac{\sigma_M^2}{\bar{n} QE}} \tag{3.14}
$$

(3.14) and (3.11) combined give a signal-to-noise ratio of

$$
SNR = \sqrt{\bar{n}}\sqrt{QE}\frac{M}{\sqrt{M^2 + \sigma_M^2}} \approx \sqrt{\bar{n} \, QE} \, 0.91 \quad . \tag{3.15}
$$

The SFM with the intensified ICCD thus shows a photon noise limited behavior for the detected photons $\bar{n} \times QE$. The fact, that the SNR achieves only nine tenth of $\sqrt{\bar{n} \, QE}$ is due to the scatter in the multiplication factor M. Fig. 3.16 compares the SNR for the intensified CCD with the one obtained for the CCD alone. The reduced QE of 0.15 of the MCP at $\lambda = 450$ nm has been accounted for. Identical illumination intensities of 1 photon/(pixel minute) have been assumed. The SNR is enhanced by a factor > 5 by the use of the image intensifier.

This motivates the decision to use the ICCD as standard detector for the 20 Hz laser setup. The data presented in the following sections has been recorded with the intensified CCD and usually the pixels have been binned 2×2.

It shall be mentioned already here that the SNR discussed here is the one of the
total SFG intensity in one pixel. The chemical contrast in sum-frequency microscopy on
Au substrates is usually a difference of $\sim 10\%$ in the total signal (see chapter 4). The
"chemical" signal is therefore smaller than the total SFG intensity and the subtraction
of two images increases the noise by a further factor of $\sqrt{2}$. This leads to a significant
reduction of the SNR in the chemical contrast. Nevertheless the results of the next
chapter demonstrate that the SFM allows for the quantitative chemical characterization
of interfaces.

Chapter 4

Chemical imaging and vibrational spectroscopy of micro-structured self-assembled monolayers

Self-assembled monolayers (SAMs) [33] of organic molecules provide numerous possibilities to modify the properties of metal- and semiconductor interfaces or of nanoparticles. Applications comprise amongst many others the control of wetting, corrosion protection and immobilization of bio-molecules.[1]

SAMs of alkanethiols ($HS(CH_2)_{n-1}CH_3$, short C_n) and their ω-terminated derivatives have been studied extensively e.g. with scanning-tunneling-microscopy (STM), atomic force microscopy (AFM) [35], He-scattering, and IR spectroscopy. Due to its high sensitivity to molecular order and symmetry, sum-frequency spectroscopy contributed significantly to the insight into the conformation and the orientation of the molecules in the SAM [36–38]. Alkanethiols can be deposited on metal surfaces from the vapor phase, from solution [39] or by microcontact printing [40, 41], where they chemisorb spontaneously. Especially long chain thiols (n≥12) on Au(111) are known to form well ordered, densely packed and stable monolayers. This order, the wide variety of possible functionalizations and the relative simplicity of preparation makes this class of SAMs also a model system for bio-membranes.

As the system alkanethiol/Au(111) is probably the best characterized self-assembled monolayer it is challenging to test the potential of the sum-frequency microscopy for a quantitative chemical analysis of a multi-component SAM with an inscribed chemical pattern. In addition SFM yields information on laterally structured SAMs, which is hardly accessible by space averaging methods like most spectroscopic and diffraction

---

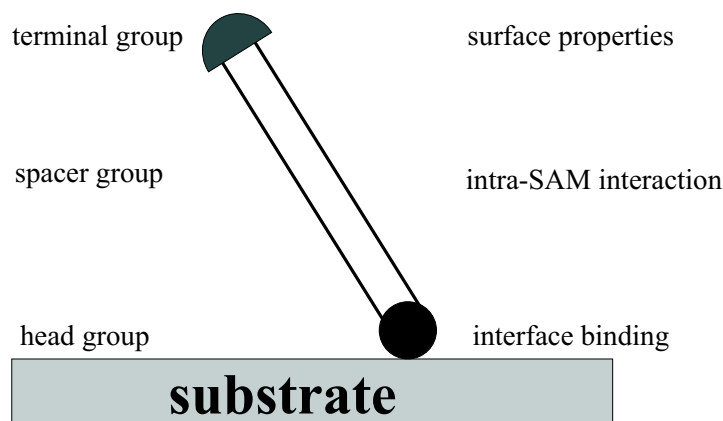[1]More appliances and respective references are found e.g. in [34].

Figure 4.1: Schematic structure of a self-assembling molecule and major interactions.

techniques.

Sum-frequency microscopy (SFM) combines the strengths of SFG spectroscopy with the benefit of lateral resolution on the μm-scale: SFM can quantitatively probe the composition of structured monolayers on the μm-scale by taking complete spectra with the microscope. In principle it is not necessary that the terminal groups are different in their chemical properties as e.g. in their hydrophobicity, as they are in the studies, which use different AFM techniques with chemically modified tips [42, 43]. SFM allows for the identification and quantification of particular chemical groups (even with isotope selectivity). This is a prerequisite for studying diffusion and intermixing processes in multicomponent SAMs prepared by microcontact printing. Taking SFG images at vibrationally non-resonant wavelengths gives access to the total molecular density of the SAM on the Au surface.

SAMs are formed by chemisorption of molecules, which consist of three building blocks (Fig. 4.1): The head group of the molecule binds to the substrate. The spacer group stabilizes the monolayer and is important for its order and compactness. Its length combined with the orientation defines the distance of the terminal group from the substrate. The terminal group determines the surface properties to a large extent. For alkanethiols the thiol group corresponds to the headgroup, the methylene chain forms the spacer group and the methyl group is the terminal group. For ω-terminated alkanethiols the terminal group is substituted by another group, e.g. by a carboxyl group.

SFM probes in particular the conformation, orientation and order of the backbone and the terminal group of the SAM. In contrast, STM probes predominantly the head-group and topography on a much smaller length scale [12]. Furthermore, SFM is a method, which allows to take in-situ images under ambient conditions and in solutions,

which is not possible for many spectroscopic and diffraction methods as high-resolution electron energy loss spectroscopy (HREELS) [44] and low energy helium diffraction [45].

In section 4.1 the main characteristics and properties of alkanethiolate SAMs will be summarized. Section 4.2 gives an overview of microcontact printing used for preparing SAMs with patterned chemical functionalities. A short description of the sample preparation follows in section 4.3. Section 4.4 shows the results obtained for self-assembled monolayers from solution. These results are compared to the SFG spectra for microcontact printed SAMs (section 4.5). The difference between the SFM images taken at the edge of large printed areas (section 4.6) and images of 10 μm wide line patterns (section 4.7) gives information about the printing process. Quality and composition of SAMs after coadsorption are probed by spatially resolved SFG spectra.

4.1 Properties of alkanethiolates on gold

In the first subsection the main structural properties of SAMs from alkanethiols on Au(111) will be summarized. The second part of this section gives a brief overview on the kinetics during the adsorption process.

Structural properties of alkanethiolate SAMs

Upon adsorption of the alkanethiols on the Au(111) surface, the reconstruction of the clean gold surface is lifted. The S-H bond is cleaved and the thiol chemisorbs to the gold surface via the sulfur atom. The high binding energy of 30.1 kcal/mol, which is nearly independent of the chain length n, contributes to the high stability of the SAM [46]. The van-der-Waals interaction between adjacent molecules in densely packed monolayers is at least 0.8 kcal mol^{-1} per methylene unit [47] and it is thus the second important stabilization factor.

Long chain thiols (n > 12) form well-oriented, compact and crystalline monolayers at room temperature. A full monolayer (ML) exhibits a hexagonal packing of the sulfur atoms in a $(\sqrt{3} \times \sqrt{3})$R30° structure with respect to the Au(111) surface [45, 48] (Fig. 4.2a). Further studies identified a $c(4 \times 2)$ superlattice [49, 50]. SFG spectroscopy [36] and X-ray standing wave results [51] indicate that the sulfur atoms are located not exactly in the three-fold hollow sites. Kluth et al. [44] deduce from their HREELS measurements that octadecanethiol adsorbs in the three-fold hollow sites at room temperature but that annealing at 375 K results in the formation of sulfur dimers that arrange in a $c(4 \times 2)$

unit cell. The origin of the $c(4 \times 2)$ superlattice is still under debate ([34] and ref. therein).

The methylene chains of alkanethiolates on Au(111) are tilted by $\theta \approx 30°$ [47,52–55] (Fig. 4.2b) from the surface normal in order to minimize the free energy of the SAM by van-der-Waals interactions of the spacer groups. The number of gauche-defects is low and the chains are in an all-trans zig-zag configuration (Fig. 4.2b). θ mainly depends on the interplay of the lattice constant of the substrate and the intra-SAM chain-chain interaction. The tilt direction ϕ is defined as the angle between the projection of the chain onto the Au(111) surface and the next-nearest-neighbor(NNN) direction of Au(111) (Fig. 4.2a). ϕ depends on the length of the methylene backbone and $\phi \sim 8°$ for C_{18} [56].

SAMs made from alkanethiols tend to exhibit a higher degree of disorder with decreasing chain length n [57]. Furthermore phases different from the $c(4 \times 2)$ structure have been observed mostly for short chain thiols (n< 12)([34] and references therein), of which the best known is the pinstripe phase at coverages below 1 ML [58–61]. This stripe phase is classified as $(p \times \sqrt{3})$ (p integer or half-integer), where p is the spacing of the stripes and $\sqrt{3}$ the periodicity within the stripe, both in units of the Au(111)-lattice spacing. The distance between the stripes scales with the length of the alkanethiol and the stripe spacing is approximately twice the length of the respective molecule. Therefore most models assume that the thiol lies flat on the surface. For decanethiolate on Au(111) Schreiber et al. [62] found the stripe phase for coverages Θ below 0.27 ML, an intermediate phase with unknown structure for increasing coverage and the beginning of the $c(4 \times 2)$ phase at $\Theta = 0.47$ ML. The stripe phase of alkanethiolates has been used recently as a template for producing bimolecular fullerene chains on Au(111) [63].

There is no clear evidence of a stripe phase in SAMs assembled from solution with commonly used concentrations (~ 1 mM). It has been observed for a low concentration (0.3 μM) by Yamada et al. [64]. One reason for this might be the high rate of adsorption for concentrations in the mM range, which makes the time window of the existence of the stripe phase too short.

Recently the stripe phase was observed for a long chain thiol, namely C_{18}, during the assembling process in a extremely diluted solution of C_{18} in ethanol ($< 1\mu$M) [65] and in a thermal desorption experiment [66].

Kinetics of the adsorption process

The adsorption process of thiols from solution on Au(111) is a process with at least two steps [39, 67, 68]. It was studied first by Bain et al. [39]: Among differently terminated alkanethiols they investigated the temporal adsorption behavior of octadecanethiol and
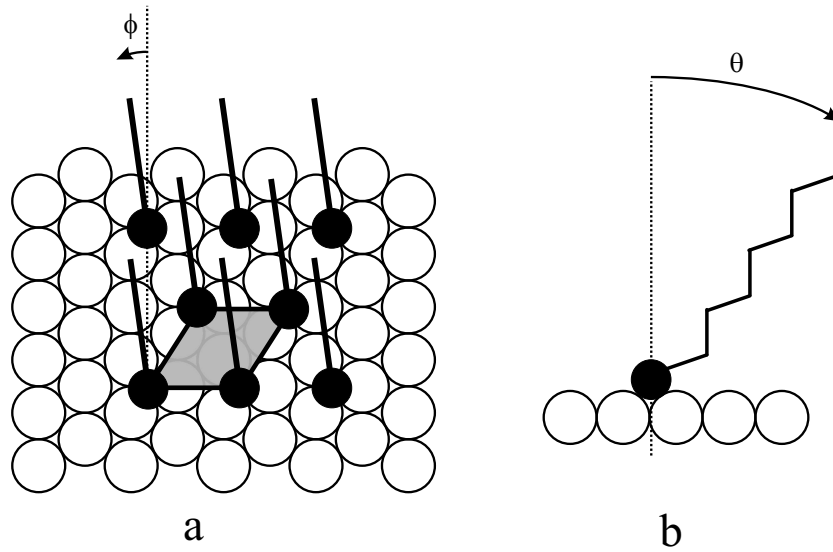
Figure 4.2: Schematic of tilt orientation of alkanethiols on Au(111): (a) tilt direction ϕ relative to the nearest neighbor direction. The grey parallelogram corresponds to the ($\sqrt{3} \times \sqrt{3}$)R30° cell. (b) tilt angle θ with respect to the surface normal.

mercaptohexadecanoic acid by ellipsometry. Two distinct steps were identified: More than 80 % of a monolayer adsorbs in a fast process (seconds to few minutes for 1 mM solutions of octadecanethiol or mercaptohexadecanoic acid). Experiments with STM [64], AFM [69] and SHG [70] revealed the domain-wise growth of the coverage in this first step. The completion and ordering of the SAM in the second step takes several hours [39].

The initial adsorption step is described well by Langmuir kinetics [37,70,71]. Quantitative results vary between different groups and it seems that the reason is the different sample preparation. The Langmuir model is based on the assumption that there is no interaction between the adsorbed molecules and that the rate of growth is proportional to the number of free adsorption sites. For a detailed discussion of more sophisticated models see e.g. [34].

Recently Himmelhaus et al. [37] studied the adsorption process from solution with SFG spectroscopy by examining the evolution of the vibrational resonances as a function of the immersion time. They reported a fast initial adsorption step ($\sim$5 min for a 3 μM solution of C_{21} in ethanol). In this step the spectrum is dominated by a broad feature centered around $\omega_{IR} = 2916$ cm^{-1} attributed to the antisymmetric methylene stretching mode. This indicates a high degree of gauche deformations in the hydrocarbon chain. The first adsorption step is followed by the straightening of the hydrocarbon chains, which happens on a 3-4 times longer timescale, as indicated by the substantial decrease of the methylene peaks. In the third and final step the reorientation of the terminal

group occurs, as measured by the evolution of the peaks corresponding to the methyl group and the methylene group adjacent to the methyl group. This step is ~ 35 times slower than the initial step. The final order in the SAM is induced by the adsorption of the last 10–20 % of a full monolayer.

4.2   Printing chemical micro-patterns into SAMs

In producing monolayers, which consist of different molecular species, the homogeneity and stability of the pattern during and after preparation is of importance. Interdiffusion, desorption and exchange processes can diminish the purity of chemical patterns. Sum-frequency microscopy is a direct method for the quantitative investigation of these processes by chemical characterization on the μm-scale with sub-monolayer sensitivity.

Various methods have been developed for the lateral structuring of chemical properties on surfaces, e.g. electron beam lithography [72], dip-pen lithography [73] and microcontact printing (μCP) [40, 41]. In μCP an "ink" – a solution containing the adsorbate molecules – is brought in contact with the substrate by means of an elastomeric stamp fabricated from polydimethylsiloxane (PDMS) (see also subsection 4.3). The method is in principle suited for producing sub-100 nm structures [74]. Recently also the printing of single proteins has been demonstrated [75]. μCP offers many advantages: Only one initial lithographic step is necessary to produce a so-called master (Fig. 4.3), from which several copies of the actual stamp can be obtained. Printing is done under ambient conditions and arrays of different patterns can be produced on large areas (> 1 cm^2) in a parallel process.

Subsequent printing routines on the same substrate with different inks or filling up uncovered regions of the substrate with molecules from solution allows to inscribe a chemical pattern into the monolayer. This is e.g. useful in controlling wetting properties of surfaces as well as in creating templates for selective adsorption of microcrystals on a pattern [76]. Biomedical applications include the selective binding or adhesion of proteins, larger bio-molecules and cells at defined positions [77]. A tempting perspective, which μCP also offers, is the possibility to realize an interface between laterally structured biomaterial and structured microelectronics.

Chemical patterns of thiolates produced by μCP have been investigated by several techniques: An indirect technique for evaluating the compactness of microcontact printed SAMs measures the protection they provide to the gold surface against etching agents [74]. An exact correlation between surface coverage of thiolates and the protection against the etching agent is probably difficult to establish, especially for low

thiolate coverages. For multicomponent SAMs scanning probe studies revealed the role of domains (size $\sim$ 15-40 nm) during the coadsorption of SAMs [78, 79]. Scanning tunneling microscopy (STM) gives a better resolution than atomic force microscopy (AFM) but probes mainly the head group, i.e. the sulfur [12]. AFM with functionalized tips allows to differentiate qualitatively between hydrophobic and hydrophilic regions in a mixed SAM [43]. The quantitative interpretation of the measurements, however, is difficult as the contrast is not only due to the chemical groups (see section 4.5). Scanning electron microscopy (SEM) shows a contrast between methyl- and hydroxyl-terminated alkanethiolates. This contrast is most probably not due to the different chemical groups directly but to contaminants, which adsorb more readily on the high free energy surfaces with terminal hydrophilic functionality [76]. The resolution of scanning electron microscopy studies in the literature is usually > 50 nm, so that domains are not resolved. Therefore regions might appear homogeneous in SEM images, although they consist of two kind of domains with different thiolate species, as in the exchange processes during post-adsorption of a thiolate on a pattern printed with a different thiolate (see section 4.7).

Such exchange processes of alkanethiolate SAMs in a solution with an adsorbed thiolate species have been investigated e.g. by contact angle measurements [80], voltammetry [81], FT-IR external reflection spectroscopy [82], SEM and secondary ion mass spectroscopy (SIMS) [83], and AFM [43]. It was found that molecules in a well ordered monolayer are exchanged at a substantially lower rate than in disordered SAMs or layers with sub-monolayer coverage. Thiol molecules with a terminal COOH group are reported to replace adsorbed alkanethiols with up to 9 methylene groups more in a photolithographically patterned SAM on the timescale of 10 min [83]. This indicates that hydrogen bonding of the terminal carboxyl group contributes significantly to the stability of the SAM. Cooper et al. give an estimate for the energy per carboxyl group of at least 7.2 kcal mol^{-1}. No exchange has been observed for homogeneous alkanethiolate SAMs on the same timescale [83]. On the timescale of $\sim$ 100 h an exchange for homogeneous SAMs has been observed [81]. When only alkanethiols are involved, longer alkanethiols can displace shorter ones due to the higher enthalpy of the interaction between the methylene groups. This exchange is not always complete and a fraction of the thiolate, which is presumed to be bonded near defect sites, is not exchanged [84].

4.3   Sample preparation

Polycrystalline Au(111) films on glass

All SAMs in this work were deposited on Au-films on glass substrates. The thorough cleaning of the substrate included ultrasonic treatment in acetone and cleaning with nochromix/H_2SO_4 conc. This ensured a low density of defects in the Au-films (thickness 2000 Å), which were thermally evaporated in vacuum (base pressure $\sim 10^{-6}$ mbar) on a 20 Å thick adhesion layer of Cr. These films are polycrystalline with a Au(111) surface orientation of the individual crystallites. Each gold film was flame-annealed below red glow (T$<$ 550° C) before the thiol is adsorbed.

Self-assembly from solution

In order to prepare homogeneous self-assembled monolayers, flame-annealed Au-samples were immersed in thiol solutions. Typical immersion times were $>$ 12 hours for solution-assembled SAMs, and $\sim$ 15 min for producing chemical patterns by post-adsorption from solution. Octadecanethiol ($HS(CH_2)_{17}CH_3$) and mercaptohexadecanoic acid ($HS(CH_2)_{15}COOH$) (Aldrich) were used as received to prepare solutions in pure ethanol (p.a.). The solutions were stored in the refrigerator under exclusion of light to minimize photo-induced oxidation of the thiols.

Microcontact printing

Flat stamps were prepared by mixing SYLGARD184 (manufacturer Dow Corning) with a curing agent (ratio 10:1) and pouring this mixture into a petri dish made from polystyrene. After 1 h (to allow bubbles to escape from the mixture) the mixture was stored at 65° C for at least 12 h in order to achieve complete polymerization. Pieces were cut from the stamp and the side facing the bottom of the dish was used for printing.

For the preparation of micro-structured stamps the micropatterned master is produced from a silicon wafer by electron beam lithography and reactive ion etching. This master (Fig. 4.3a) can be reproduced many times in PDMS (Fig. 4.3b) by the same procedure as described for the flat stamp. Microcontact printing is done under dust-reduced conditions at room temperature. The applied procedure is illustrated in Fig. 4.3c+d: The flat or patterned stamp ($\sim$ 5 $\times$ 10 mm^2) is freshly cut, rinsed with 10 ml of ethanol, and dried under a stream of N_2. A drop of thiol solution ($\sim$ 100 μl) is put on the stamp. Typical soaking times are 30 s (flat stamp) or 60 s (structured stamp). The drop is removed under a stream of nitrogen applied for at least 20 s. The stamp then is placed on the substrate within 15 s. Contact to the substrate is verified by the change
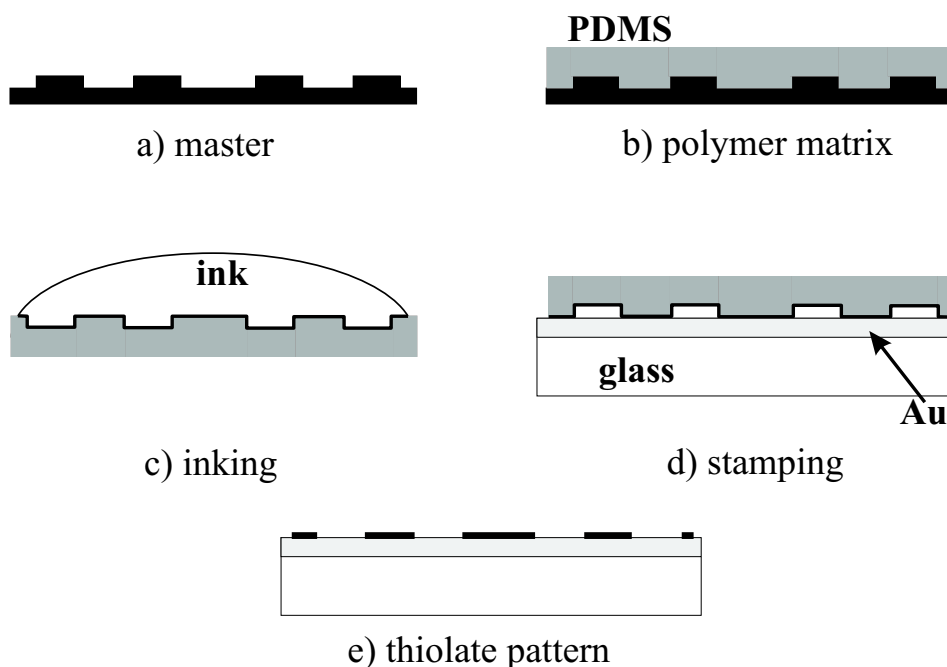
a) master

PDMS

b) polymer matrix

ink

c) inking

glass

Au

d) stamping

e) thiolate pattern

Figure 4.3: Patterning by microcontact printing: A micropattern on a Si master (a) can be replicated many times as a PDMS stamp (b). Inking this stamp with a solution of thiols (c) and subsequent printing (d) generates a thiolate pattern (e) on the Au substrate.

of reflecting properties at the polymer/gold interface. If necessary, light pressure is employed to accomplish complete contact. Contact times ranged from 30 s to 120 s. The sample with the thiolate pattern (Fig. 4.3 e) is rinsed with ethanol and either mounted in the SFM or immediately immersed in a thiol solution for producing micro-structures consisting of two different thiolates.

4.4 Probing order by sum-frequency spectroscopy in monolayers self-assembled from solution

4.4.1 Octadecanethiolate SAM

Fig. 4.4 shows SFG spectra of SAMs prepared by immersing the Au-substrate overnight (>12 h) in a 1 mM ethanolic solution of octadecanethiol (brief C_{18}) or mercaptohexadecanoic acid (brief $C_{15}COOH$) respectively. The lines as guide to the eye are the data (symbols) smoothed with an average of 3 neighboring data points. To our knowledge this is the first SFG spectrum reported of a $C_{15}COOH$ SAM. The molecules are sketched in Fig. 4.5. Both spectra have been normalized to the non-resonant background on the low-energy side of the spectrum.
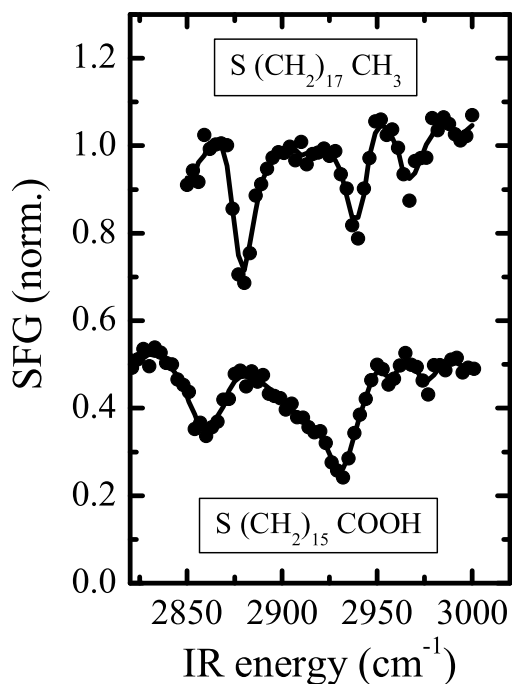
Figure 4.4: SFG spectra of differently terminated self-assembled monolayers: Octadecanethi-olate SAM (top). Mercaptohexadecanoic acid SAM (bottom). (The dots are exp. data, the line is the smoothed data, the bottom spectrum has been offset by -0.5 units for clarity.)
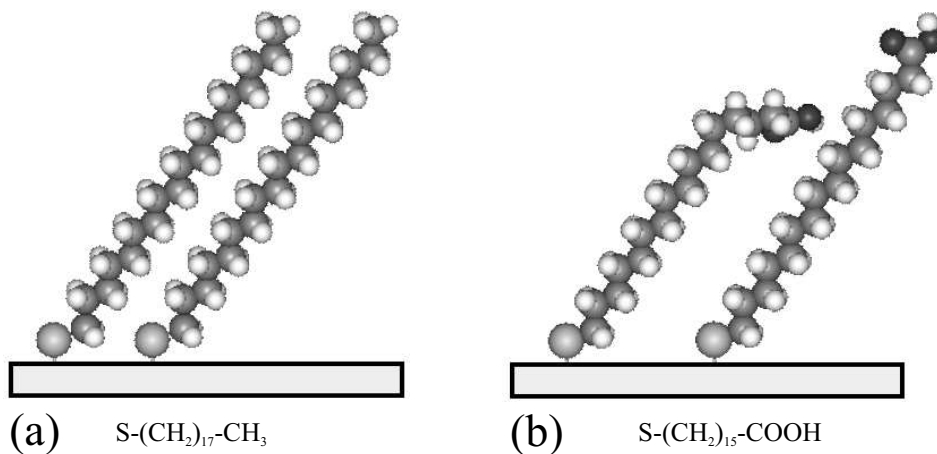
Figure 4.5: (a) Molecular structure of all-trans octadecanethiolate on Au. (b) Mercaptohex-adecanoic acid with and without gauche defect (dark atoms=oxygen).

For the octadecanethiolate SAM three stretching modes appear as negative peaks on a high SFG intensity generated at the thiolate-Au interface. The high intensity is due to an interband transition of the gold that has its threshold around 506 nm [13]. The infrared energy of $\omega_{IR} = 2900$ cm^{-1} corresponds to a wavelength of the SFG light of

vibration	cm^{-1}	symbol
CH$_3$		
CH$_3$, sym	2880	r$^+$
CH$_3$, sym, Fermi	2939	r$^+_{FR}$
CH$_3$, antisym, in plane	2967	r$^i_{ip}$
terminal CH$_2$, sym, adjacent to CH$_3$	2865	d^+_t
CH$_2$, not observed		
CH$_2$, sym	2855	d$^+$
CH$_2$, antisym,	2916	d$^-$

Table 4.1: Vibrations of the methyl and methylene group of an octadecanethiolate SAM self-assembled from solution. The values for CH$_3$ are taken from the SFG spectrum in Fig. 4.4. The CH$_2$ positions are observable for less well ordered phases and are taken from [37].

ca. 460 nm, which lies well above this threshold (see also section 2.4). This SFG signal shows no features in the range of the spectra and is denoted therefore as (vibrationally) non-resonant.

The three peaks can be assigned to the following methyl resonances of the adsorbed thiolate: The symmetric vibration at 2880 cm^{-1} and its Fermi resonance at 2939 cm^{-1} and the antisymmetric vibration at 2967 cm^{-1} [11, 37, 55, 85, 86] (Tab. 4.1). The peaks are negative because there is a phaseshift of $\phi \approx \pi$ between the resonant second order susceptibility $\chi^{(2)}_{res}$ and the non-resonant $\chi^{(2)}_{nr}$ (compare Eq. 2.33). The antisymmetric stretching mode of the methylene group in the alkane backbone at 2916 cm^{-1} is not observed. This is due to the high order in the octadecanethiolate layer with the backbone being predominantly in an all-trans configuration (Fig. 4.5a). The resulting local inversion symmetry for the CH$_2$-groups suppresses the emission of the corresponding SFG signal. This local symmetry does not hold for the terminal CH$_2$-group next to the methyl group. Therefore a small positive peak can appear at 2865 cm^{-1} [37].

4.4.2 Mercaptohexadecanoic acid SAM

In contrast, the C$_{15}$-COOH SAM does exhibit symmetric (2860 cm^{-1}) and antisymmetric (2930 cm^{-1}) methylene vibrations (Fig. 4.4 bottom). The strength and spectral width of these modes demonstrate the deformation of the alkane backbone (see the left molecule in the Fig. 4.5b), which destroys the local inversion symmetry [3]. From the spectrum, which is comparable to the one of an amino-amido thiolate [38], it can be concluded that

the hydrocarbon backbone of the C15-COOH thiolate is not in an all-trans configuration. Bittner et al. estimate for similar methylene intensities that the intensity is due to $\gtrsim 1$ CH_2-group per molecule [38]. Dannenberger et al. propose as a model for their NEXAFS results on SAMs with a terminating carboxyl group, that already at the beginning of the adsorption process the carboxyl groups dimerize due to hydrogen bonding with an energy gain of 60 kJmol^{-1}([87] and references therein). Such a dimer is most stable for a planar configuration of the two COOH groups involved, a constellation, which is incompatible with a well ordered methylene all-trans backbone and thus in agreement with the observed spectrum.

A vibrational line directly related to the carboxyl group was not observed in the SFG spectrum between 2400 cm^{-1} and 3720 cm^{-1} (see also section 4.7.2). The range includes vibrations and overtones of the free and the hydrogen bonded carboxyl group [88]. There are several possible reasons for this result: 1.) The product of the IR and the Raman tensor might be small and may leads to a peak height, which is smaller than 5% of the Au signal. This value is needed to identify the peak in the SFG spectrum. 2.) The IR dipole moment may be oriented parallel to the Au surface. The Fresnel coefficient for this geometry is too small for the peak to be detected. 3.) The COOH-groups are oriented at random. This isotropic orientation of the endgroup is not likely due to the strong anisotropy of the interface. 4.) The dimerization of two carboxyl groups in a planar configuration, suggested by Dannenberger [87] et al., possesses inversion symmetry [88] and can thus explain the vanishing SFG signal.

4.5   SAMs printed with a flat stamp

The preparation of SAMs from solution leads to a laterally unstructured monolayer. Microcontact printing has been described in section 4.2 as a straight-forward method to produce laterally structured chemical patterns with dimensions down to 100 nm. In this section the sensitivity of sum-frequency spectroscopy to molecular order and orientation is used to compare printed SAMs with SAMs prepared from solution.

Fig. 4.6 displays the SFG spectrum of a C_{18}-SAM, which was printed on a Au-substrate with a flat, i.e. unstructured, PDMS stamp (concentration 1 mM, 30 s inking time, 60 s contact time). The spectrum was taken about 3 mm away from the edge of the stamp. Table 4.2 lists the position of the prominent peaks. Their positions and amplitudes agree well with the ones of the SAM self-assembled from solution (Tab. 4.1 and upper spectrum in Fig. 4.4). The ratio of the intensities in the symmetric and
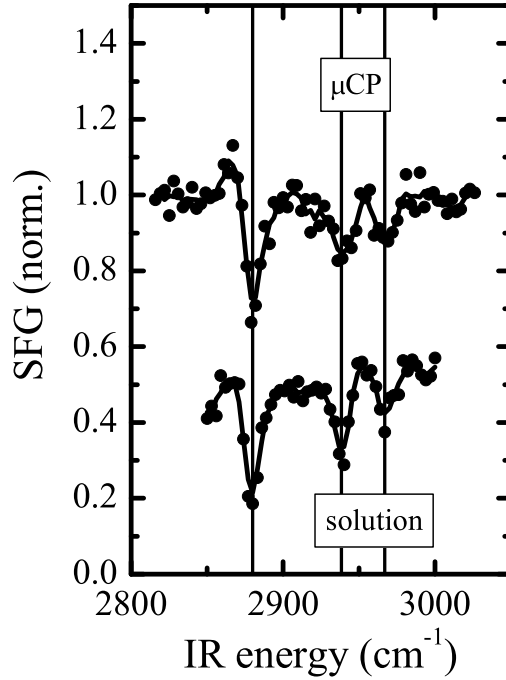
Figure 4.6: The SFG spectrum in the inner region of a microcontact printed octadecanethiolate SAM (upper spectrum) is similar to the one of the solution assembled SAM from Fig. 4.4 (top spectrum), which is also displayed in this figure at the bottom with an offset of -0.5 units. (dots = data, line = 3-point-smoothed data, vertical lines at the position of the dominant methyl vibrations)

antisymmetric CH_3 stretching modes are about the same indicating a comparable average tilt angle of the thiolates [12]. Symmetric and antisymmetric methylene stretching vibrations are not observed either. Thus the spectrum of the printed monolayer is in good agreement with the one of the solution-assembled SAM.

This result is in agreement with the result from a NEXAFS study, which observed

vibration	cm^{-1}	symbol
terminal CH_2, sym, adjacent to CH_3	2865	d_t^+
CH_3, sym	2880	r^+
CH_3, sym, Fermi	2939	r_{FR}^+
CH_3, antisym, in plane	2968	r_{ip}^i

Table 4.2: Vibrational resonances in the spectrum of the microcontact printed octadecanethiolate SAM in Fig. 4.6 top.

no significant difference for the orientation of the hydrocarbon backbone and the order in SAMs of C_{18} (and C_{12}) prepared from solution and by μCP with 2 mM ink [89]. Grazing incidence X-ray diffraction (GIXD) also showed the same molecular structure for both preparation methods, namely the $(\sqrt{3} \text{ x } \sqrt{3})$R30° structure with the c(4 x 2) superlattice [90]. Identical structures are observed also by STM, although for higher concentrations of the ink and under different stamping conditions [91]. For a short contact time of 5 s (and with applied pressure to the stamp) Böhm et al. [92] identified by SFG spectroscopy a vibrational resonance in the CH_2 region combined with a lower contact angle in comparison to a solution-prepared SAM of C_{18}. Both results are attributed to a substantial number of gauche defects at the early stage of self-assembly, which lead to disorder in the film. However, for longer contact times of 30 s and more, as used in this thesis, they observe typical contact angles of a well ordered monolayer. For this longer contact time no SFG spectrum is presented in their publication.

Different from our results and the results just discussed, AFM and especially lateral force microscopy (LFM) and friction force microscopy (FFM) yield a contrast between regions, which have been prepared by microcontact printing and from solution. This contrast is mainly attributed to differences in the density of domain boundaries and in the defect density and not to the molecular order and structure [89, 90]. Bar et al. showed that contaminants, minimal differences in the packing density of the SAM and experimental parameters of the AFM influence substantially the contrast observed in LFM and FFM [93, 94].

4.6   Contrast in sum-frequency microscopy: The edge of a μCP-SAM on gold

The results on thiolate SAMs presented so far were obtained by SFG spectroscopy. According to equation 2.33 the spectrum reveals information on the orientation and order of the thiol molecule, while the question of thiolate density remains open. This question can be answered by sum-frequency microscopy, which yields additional information by electronic contrast (see section 2.5). The stability of microcontact printed SAMs at elevated temperatures is briefly treated at the end of this section.

Fig. 4.7a shows a linear optical image of the edge of a printed C_{18}-SAM region taken with the microscope in the reflected light with a wavelength of 450 nm. The sample is the same as in subsection 4.5. The dotted line indicates the border between the printed region and the bare gold. No difference in the reflected light intensity is observed. In

contrast, SFM images of exactly the same region (Figs. 4.7b-d) exhibit substantial contrast.

SFM images of the edge were taken at 2824 cm^{-1}, 2878 cm^{-1}, and 2918 cm^{-1} to obtain information on the adsorbate density, the methyl contrast $\tilde{\chi}_{CH3}^{(2)}$ (Eq. 2.38) , and the methylene contrast $\tilde{\chi}_{CH2}^{(2)}$. Measuring times are 140 min per image and the greyscale is identical for all three images. The darker region in the upper left corresponds to the printed area, the brighter area to the clean Au surface. The slowly varying intensity in the image is due to inhomogeneities of the illumination by the IR beam. The plots on the right of Fig. 4.7 show the SFG intensity added up along the direction of the arrow in Fig. 4.7b within the white rhomb. They represent the cross section of the edge between the thiol and the pure Au. The intensity is normalized by $I_{nr}(0)(\omega_{IR} = 2824$ cm$^{-1})$ on the high intensity side of the edge. The x-axis is given by the coordinate measured perpendicular to the edge. The relative contrast between the two areas is determined by the high and low intensity at the edge between the dashed lines in the cross sections.

For the non-resonant IR frequency of 2824 cm^{-1} (Fig 4.7b) a contrast of $\tilde{\chi}_{nr}'^{(2)}(\Theta) = 33\%$ in the SFG intensity is observed between the thiolate covered and the pure Au. $\tilde{\chi}_{nr}'^{(2)}$ is a measure for the adsorbate density. Buck et al. studied in-situ the adsorption of thiols on gold by SHG [70, 71]. The SHG intensity decreased exponentially in the time coordinate from the value for pure gold to a value for gold covered by a monolayer of C_{16}. The formation of the thiolate monolayer can be described by Langmuir adsorption kinetics (see section 4.1). The thiolate coverage was calibrated in that study by X-ray photoelectron spectroscopy (XPS). These and another study [95] concluded that for metal substrates $\chi_{nr}^{(2)}$ changes linearly with adsorbate coverage:

$$\chi_{nr}'^{(2)}(\Theta) \propto \Theta \tag{4.1}$$

The interaction of the sulfur atom of the thiolate with the Au surface modifies the non-resonant susceptibility. The non-linear optical properties of the interface are either localized on a scale smaller than the distance between adsorbates or they arise from extended regions while the contributions of individual adsorbates remain linear perturbations. The results from second-harmonic generation in the visible cannot be transferred a priori to the IR-vis sum-frequency generation process, as $\overleftrightarrow{\chi}^{(2)}$ is a function of the involved frequencies in the three wave mixing (see section 2.2). Himmelhaus et al., however, showed that the linear relation (4.1) holds also for IR-vis sum-frequency generation with $\omega_{IR} \approx 3000$ cm^{-1} [37]. From (4.1) and (2.39) follows the linear dependence of the electronic contrast on the coverage:

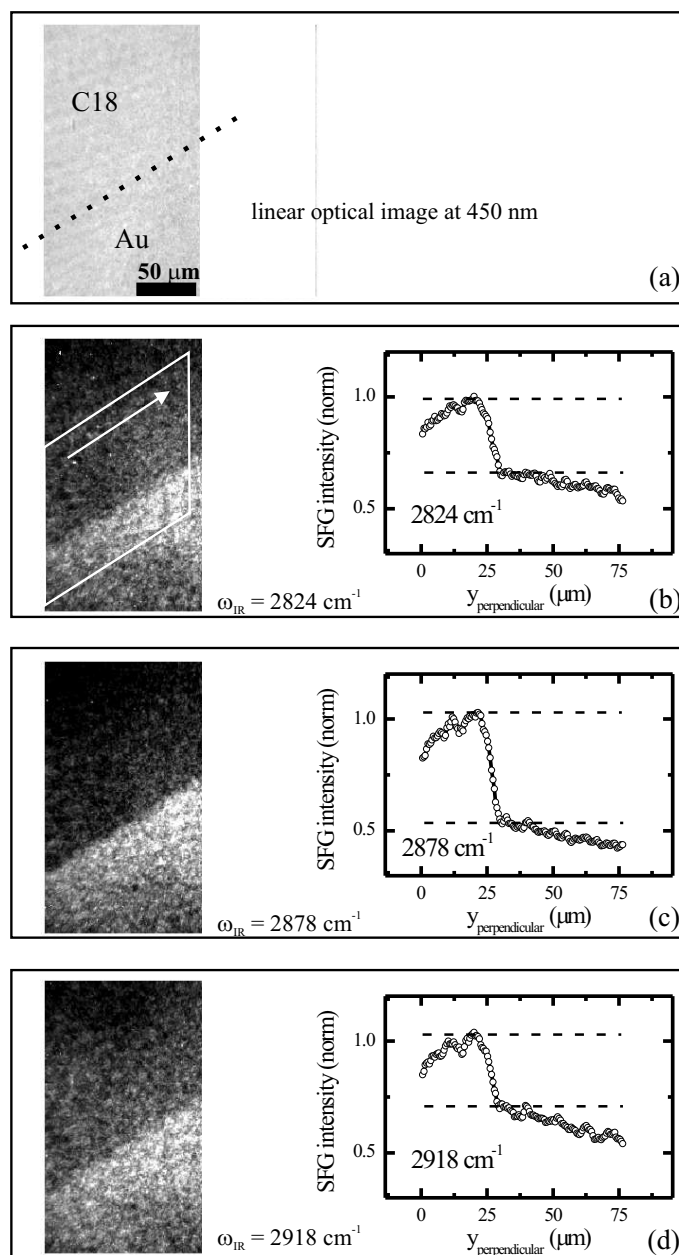$$\tilde{\chi}_{nr}'^{(2)} \propto \Theta \tag{4.2}$$

Figure 4.7: (a) Image taken in reflection with light at a wavelength of 450 nm. (b-d) SFM images of the same region, which show the edge in a microcontact printed SAM at the (b) vibrationally non-resonant IR frequency $\omega_{IR} = 2824$ cm^{-1}, (c) in resonance with the symmetric methyl vibration at $\omega_{IR} = 2878$ cm^{-1}, and (d) with the antisymmetric methylene vibration at $\omega_{IR} = 2918$ cm^{-1}. The brightness scale is identical in all three SFM images. Right hand side: Cross sections for the respective images have been obtained by adding up the lines along the direction of the arrow within the displayed frame in (b). The x-axis is the distance measured perpendicular to the edge.
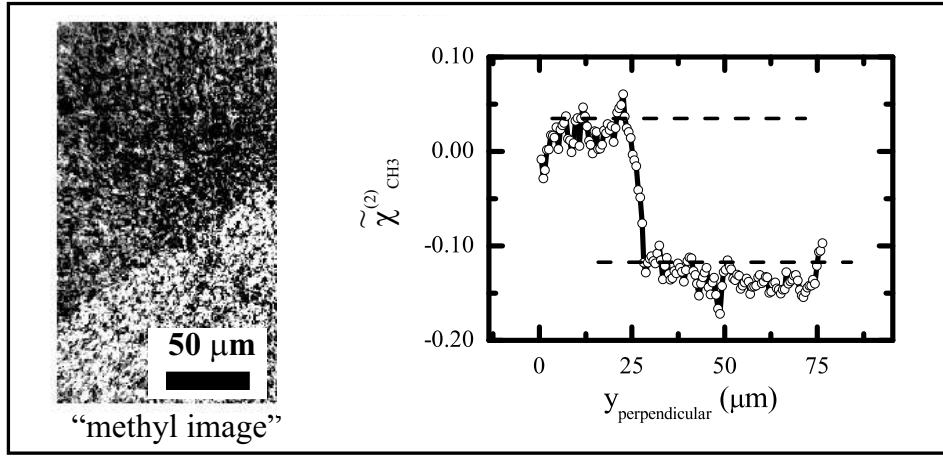
Figure 4.8: Vibrational contrast of the methyl group for the measurement in Fig. 4.7. The cross section is obtained as in Fig. 4.7.

The adsorption of thiolates changes the electronic structure in the topmost Au layer. We use this electronic contrast in sum-frequency microscopy to monitor the thiolate density.

The electronic contrast $\tilde{\chi}_{nr}^{\prime(2)} = 33\%$ corresponds fairly well to the literature: Himmelhaus et al. [37] report a reduction of $\sim 25\%$ in the non-resonant SFG intensity by the adsorption of a full monolayer of C_{22}. The microcontact printed SAM has about the same adsorbate density, i.e. sulfur intensity, as solution assembled monolayers.

An enhanced contrast of 49% is observed for the methyl resonant wavelength $\omega_{IR} = 2878$ cm^{-1} (Fig. 4.7c). This increased intensity difference is due to the additional vibrational contrast of the methyl group. The chemical information can be separated by applying (2.38). The result is a pure "methyl map", which is shown in Fig. 4.8. The dark regions represent the presence of methyl groups in an upright orientation (dark because $cos(\phi_2) \approx -1$). The bright regions correspond to the pure Au surface. The edge of the adsorbed thiolate can clearly be discerned. The cross section shows a $\tilde{\chi}_{CH3}^{(2)}$ contrast of about $16 \pm 2\%$ with respect to $\chi_{nr}^{(2)}(0)$. In order to compare $\tilde{\chi}_{CH3}^{(2)}$ with the contrast in the spectrum of this SAM (Fig. 4.6) it must however be normalized to $\chi_{nr}^{(2)}(0) + \chi_{nr}^{\prime(2)}(\Theta = 1)$ instead of normalizing to $\chi_{nr}^{(2)}(0)$. This yields a chemical contrast of $24 \pm 3\%$ in good agreement with the SFG spectrum ($28 \pm 4\%$) from the center of the printed area (Fig. 4.6).

Fig. 4.7d has been recorded in resonance with the asymmetric methylene resonance at $\omega_{IR} = 2918$ cm^{-1}. The cross section exhibits a contrast of 32%. For $\tilde{\chi}_{CH2}^{(2)}$ evaluated as just described for $\tilde{\chi}_{CH3}^{(2)}$ no contrast is observed in the image and in the cross section (noise level $\approx 2\%$, data not shown), demonstrating the absence of gauche defects and

C$_{18}$ (μCP, 60 s), unstructured stamp

$\tilde{\chi}_i^{(2)}$	norm. to $I_{nr}(0)$	norm. to $I_{nr}(\Theta)$
$\tilde{\chi}_{nr}^{(2)}$	0.31	–
$\tilde{\chi}_{CH2}^{(2)}$	< 0.02	< 0.03
$\tilde{\chi}_{CH3}^{(2)}$	0.16	0.24

Table 4.3: Non-resonant and resonant contrasts according to eqs. 2.39 and 2.38 for the microcontact printed SAM in Fig. 4.7. The left column contains the values obtained by normalization to the pure gold surface. The contrast values normalized to the substrate signal of the thiolate covered Au surface are listed in the right column, in order to compare the contrast with the spectrum in Fig. 4.6.

thus the high order of the molecular backbone in the SAM. All contrast values are summarized in table 4.3.

Combining the results of this and the last section, SFM shows, that the octadecanethiolate SAM prepared by microcontact printing is equally well ordered as a SAM assembled from octadecanethiol solution. This order is present in the center of the stamped area as well as at its edge. These results were obtained for many samples prepared by this method.

For technical applications it is important to know, how stable the order in the thiolate SAM is and if the pattern stays unchanged. For this we heated several samples of microcontact printed SAMs in an argon atmosphere to temperatures between 40° C an 115° C. The total heating time was up to 220 h. During this time we interrupted the heating and took SFM images of the edge after the sample had returned to room temperature. Within the resolution of our microscope (2.8 μm) no broadening of the edge of the printed SAM was observed. For temperatures above 70° C, however, a degradation of the SAM was observed, which occurred sooner for higher temperature.

4.7   Monolayers with inscribed chemical micro-structures

A road to more complex chemical patterns is microcontact printing of one thiol with subsequent adsorption of a different thiol from solution. In order to understand the properties of the final structure it is necessary to first characterize the microcontact printed phase consisting of one thiol. The results of microsctructured SAMs of C$_{18}$ and
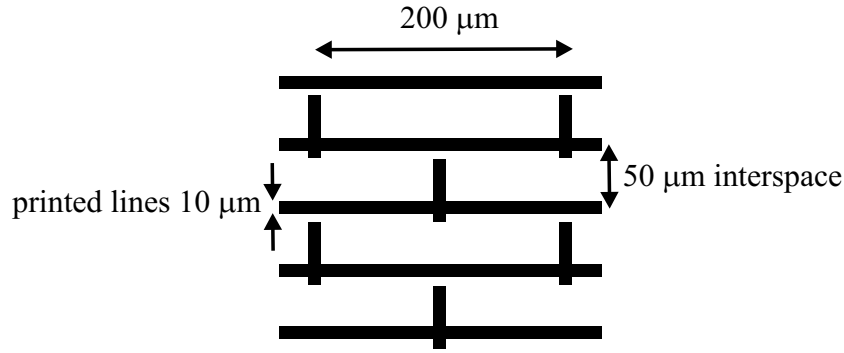
Figure 4.9: Schematic drawing of the pattern on the micro-structured PDMS stamp.

$C_{15}COOH$ are presented in the first two subsections. These are followed by the results on chemical patterns produced by post-adsorbing one thiol species on a printed pattern of the other. The quantitative results of these four subsections are discussed at the end of this section.

4.7.1 Patterns of octadecanethiolate on Au (μCP)

This subsection characterizes printed C18 micropatterns and demonstrates that the vapor transport is an significant process even for long chain thiols such as C_{18}.

Patterns of octadecanethiolate on Au with 10 μm wide lines and a distance of 50 μm were prepared by microcontact printing. The pattern (Fig. 4.9) extends over the whole stamp. Fig. 4.10 shows the SFM results for a sample with the preparation parameters (C_{18} concentration 0.6 mM, 30 s inking, 60 s contact).

The cross section on the right hand side of Fig. 4.10 were obtained again by adding up lines in the frame parallel to the direction indicated by the black arrow.

The SFM image (Fig. 4.10a) is taken at the vibrationally non-resonant IR frequency of $\omega_{IR} = 2821$ cm^{-1}. The image provides contrast specific to the Au-thiolate interface and monitors the density of Au-sulfur bonds. $\tilde{\chi}'^{(2)}_{nr}(\Theta)$ was determined according to eq. (2.39) by replacing $I_{nr}(0)$ with $I_{nr}(\Theta)$ of the area between the lines: The non-resonant contrast of $\tilde{\chi}'^{(2)}_{nr}(\Theta)$ between printed lines and the interspace is 24%.

Fig. 4.10b shows the corresponding image and cross section for $\omega_{IR} = 2879$ cm^{-1}. The respective scales are identical to Fig. 4.10a. The contrast between the printed lines and the interspace is 34% as it is enhanced by the chemical contrast $\tilde{\chi}^{(2)}_{CH3}$.

The chemical information $\tilde{\chi}^{(2)}_{CH3}$ is displayed in Fig. 4.10c, which shows the chemical map of the methyl group calculated with (2.38). The contrast of the line pattern in the image is just above the photon noise level (see also chapter 7). Determining the cross
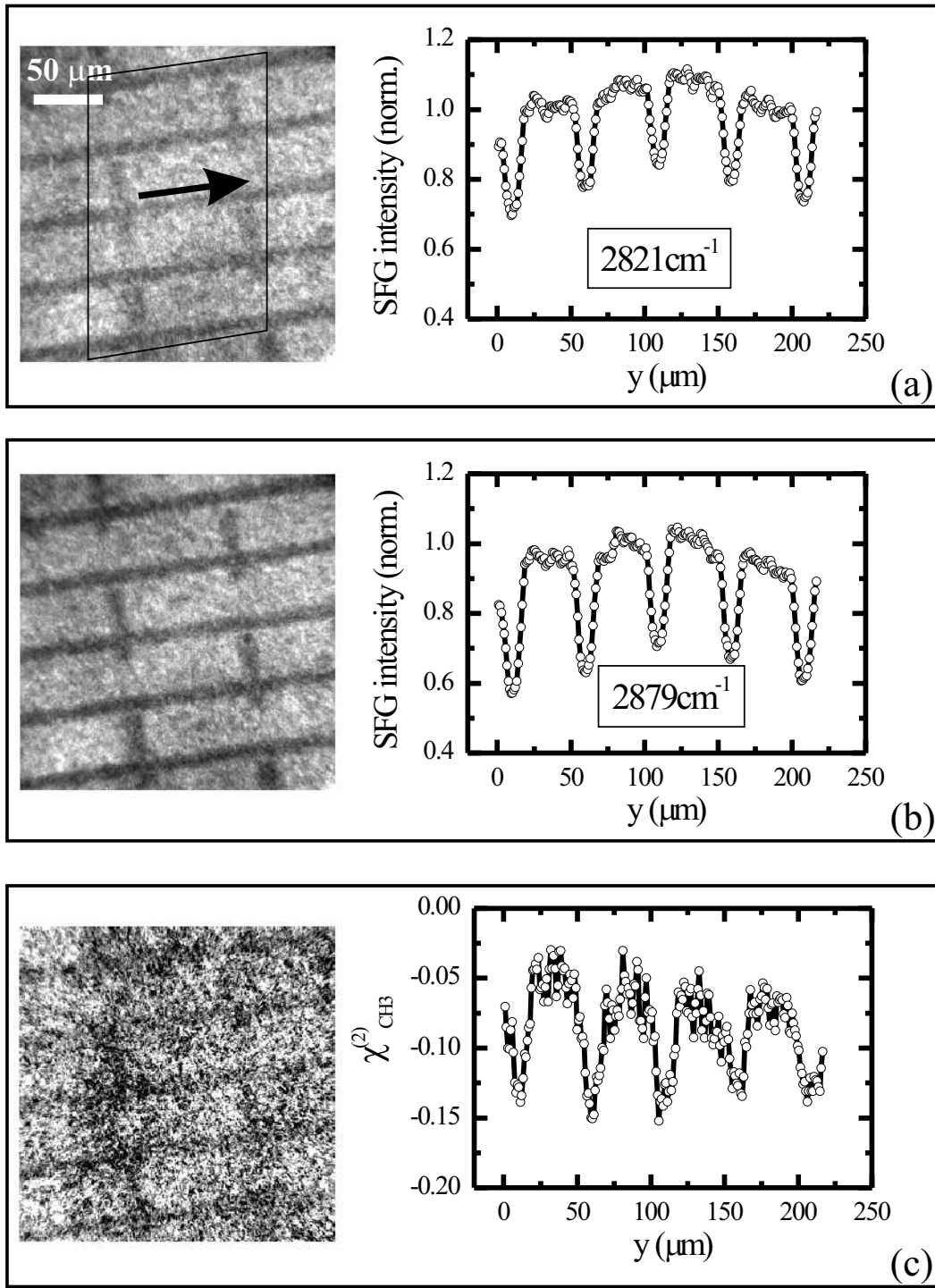
Figure 4.10: SFM images (acquisition time = 60 min, average SFG intensity = 35 photons/pixel) and cross sections of a micro-structured pattern of octadecanethiolate on gold: (a) at 2821 cm^{-1}, (b) at 2879 cm^{-1}, (images reproduced with identical brightness scale). (c) represents $\tilde{\chi}_{CH3}^{(2)}$ evaluated with eq. 2.38. $I_{nr}(0)$ was replaced by the value of $I_{nr}(\Theta)$ in the Au area for $\omega_{IR} = 2821$ cm^{-1}.
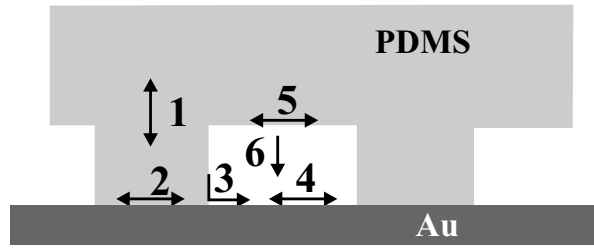
Figure 4.11: The scheme sketches paths of dispersal of thiols during the printing process. The numbers identify different paths and are referred to in the text. From [74]

section as for Figs. 4.10a and b yields a contrast in $\tilde{\chi}^{(2)}_{CH3}(\Theta)$ of 9% between lines and interspace. This contrast is superimposed on a value of $\tilde{\chi}^{(2)}_{CH3}(\Theta) = -0.05$ between the lines (Fig. 4.10c, cross section). The effect that $\tilde{\chi}^{(2)}_{CH3}(\Theta)$ is ≤ 0 also in the interspace was observed in general for all samples of this kind.

We thus obtain the result that the non-resonant as well as the resonant contrast between the printed lines and the interspace, which was not in contact with the stamp, are significantly lower than for the SAM prepared with an unstructured stamp.

The printed pattern (Fig. 4.9) does not consist exclusively of parallel stripes. The printed area outside the stripes, however, represents less than 7% of the evaluated region. This reduces the measured contrast in the cross sections of the SFM images by $\approx 2\%$, i.e. by a value corresponding to the experimental error of $\pm 2\%$. The chemical contrast $\tilde{\chi}^{(2)}_{CH3}$ is reduced by less than 1%, which is definitely within the experimental noise (Fig. 4.10c, right).

Low molecular weight fragments of the PDMS might be deposited on the Au substrate during the printing process and might reduce the quality of the deposited thiolate SAM. In order to test this effect as the origin of the reduced contrast the identical printing process was applied but instead of the ink only pure ethanol was used. Subsequently the sample was immersed for 15 min in a 1 mM solution of C_{18}. This time is sufficient to form a monolayer with more than 80% of the final coverage layer [39]. Images taken at the resonant wavelength were found to be homogeneous and the added up cross section (noise level: 3%) showed no contrast. No trace of the periodic line pattern could be detected in the Fourier transfor of the image. Thus the reduced contrast between printed areas and the gold in comparison to the results of the flat stamp must originate from the dispersal of thiols during printing.

Delamarche et al. identified different possible paths for the dispersal of thiols during microcontact printing [74], which are sketched in Fig. 4.11. These paths are briefly

summarized as follows: Thiols diffuse easily in PDMS (path 1)([74], especially reference 42). Where the stamp is in contact with the substrate, lateral diffusion of thiols occurs at this interface (path 2). This could also affect the interspace of the printed lines (also paths 3 and 4). Within the precision of our SFM, the printed lines do not broaden for printing times between 30 s and 120 s. However, at higher concentrations of thiols in the ink (4.9 mM) we observed a broadening of the lines from 10 ± 1 μm to 15 ± 1 μm. At the same time no smearing out of the edges is seen within the resolution of the SFM. This demonstrates that diffusion from the printed area to the interspace should be seen by a broadening of the lines and that it cannot explain the lower contrast of the interspace several micrometers away from the printed lines (Fig. 4.10). Path 5 denotes the thiol diffusion along the PDMS surface and is not considered here, as it does not affect the Au substrate directly.

The lower contrast values are most likely due to the process of vapor phase transport of C_{18} in the cavities, which form between the stamp and the Au-substrate (paths 6 and 4). In order to study how fast the interspaces are filled by the thiol during the stamping process we compared the results from the flat stamp with the contrast values of line patterns printed with the same ink concentration (0.6 mM) for different printing times (Fig. 4.12 and Tab. 4.4). The Au surface is not exposed to vapor thiol in the experiment with the flat stamp (section 4.6). Therefore the contrast values in Tab. 4.3 correspond to an exposure time of 0 s. Further the contrast is given for lines printed 60 s and 120 s, respectively, and evaluated as in Fig. 4.10. The results of section 4.6 justify the assumption, that the printed lines exhibit a well ordered phase after 60 s and 120 s contact time.

The contrast for non-resonant wavelengths (full symbols in Fig. 4.12) monitors the difference in the sulfur coverage between printed lines and interspaces. This contrast is reduced from 33% , which corresponds to a coverage of 1 ML (Tab. 4.3), down to about 10% (Tab. 4.4). The combined electronic and vibrational contrast for the symmetric methyl vibration at 2880 cm^{-1} decreases from 49% down to 19% (open symbols).

The results for the two samples with 120 s contact time do differ only slightly. The evaluation procedure gives an uncertainty of less than ± 2%. We tested the reproducibility of the quantitative evaluation for the same sample on two different days. The contrast values between lines and interspaces can be reproduced within ± 1% demonstrating the reproducibility of quantitative chemical analysis in sum-frequency microscopy. Differences in the contrast, which are substantially larger than 2%, are therefore due to different sample properties and not due to the method.

A linear fit of the data points (Fig. 4.12) shows that the non-resonant contrast
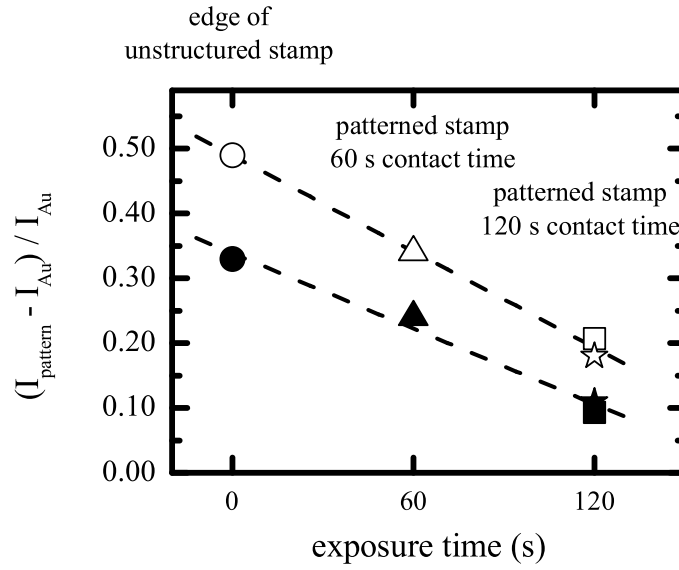
Figure 4.12: Pattern contrast as a function of exposure time to C_{18} vapor. The edge in section 4.6 serves as a reference for contrast without exposure to C_{18} vapor (circles). For the structured stamp (other symbols) it is assumed that the contact time corresponds to the time of exposure to C_{18} vapor, which is fulfilled if the diffusion through the gap between stamp and surface is so fast that it can be neglected on this time scale. Values for a non-resonant ω_{IR} (closed symbols) and in resonance with the symmetric methyl vibration (open symbols).

approaches zero faster than the combined contrast. The linear fit is a qualitative first order approximation, as the adsorption process follows Langmuir kinetics, which would result in an exponential decay of the data. The decrease in the non-resonant contrast shows that thiols are adsorbed in the interspace. The faster decrease in the fit for

C_{18} (μCP), contrast lines/interspace

norm. to $I_{nr,interspace}(\Theta)$

IR wavelength	contact time (s)		
	60 s	**120 s**	**120 s**
non-resonant	0.24	0.11	0.10
2880 cm^{-1}	0.34	0.18	0.21

Table 4.4: Contrast values for microcontact printed lines of C_{18} with different contact times. The absolute error of the individual values is ± 0.02 (see also text).

the non-resonant contrast can be understood, if we assume, for example, that the thin phase of C_{18} exhibits a different averaged orientation or even disorder of the CH_3 group resulting in a lower vibrational contrast (see also section 4.1).

Delamarche et al. [74] studied the transport through the gas phase in cavities formed by the substrate and the stamp for microcontact printing of sub-μm patterns on gold. The gold was then etched in a solution of CN^-/O_2. Well ordered thiolate monolayers protect the gold surface against etching. Unprotected areas are removed. From SEM images of the gold substrate after the etching process conclusions are drawn on the distribution of thiols. The authors clearly see the adsorption of C_{16} from the vapor phase in the interspace of sub-μm structures. However, for a stamp with a height of 3 μm, which is comparable to the one of the stamp used in this study, they find no significant deposition of C_{16} between printed lines for contact times of 20 s, even though the vapor pressure is still one order of magnitude higher for C_{16} than for C_{18}, which is used in the experiment discussed here. This apparent discrepancy may indicate the high sensitivity of sum-frequency microscopy also to thin phases of adsorbed thiolates. The shorter contact time (20 s) in their publication creates a thiolate phase between the pattern with a coverage clearly below 1 ML. Such a phase probably does not give sufficient resistance to the etching.

In order to check whether the unexpectedly high transport rate through the vapor phase is plausible we used a simplified model: The impingement rate ϕ per area for molecules of mass m at a vapor pressure $\bar{p}$ and temperature T is given by [96]:

$$\phi = \frac{\bar{p}}{\sqrt{2\pi mkT}} \qquad , \tag{4.3}$$

where k is the Boltzmann constant. Assuming a sticking probability of 1 yields a lower limit for the covering time τ. Then the adsorption rate r_{ads} for a Au surface is given by

$$r_{ads} = \frac{\phi}{n_{sites}(t)} \qquad , \tag{4.4}$$

where $n_{sites}(t)$ is the density of free thiol adsorption sites. The resulting Langmuir isotherm of the real adsorption process leads to an exponential decrease in the contrast with $e^{-\frac{t}{\tau}}$ with $\tau = 1/r_{ads}$.

The fit in Fig. 4.12 can be understood as a linear approximation of the Langmuir isotherm. In this linear approximation the interspace will be covered after the charac-

teristic time τ. For

$$\bar{p} = 3 \times 10^{-5} \ Pa$$
$$m = 286 \ u$$
$$T = 300 \ K$$
$$n_{sites} = 4.6 \times 10^{18} m^2$$

a characteristic time $\tau = 17$ s is obtained[2]. This approximation yields the lower limit for τ. In the experiment diffusion in the gas phase probably also plays a role. Furthermore the partial pressure of C_{18} solvated in the PDMS stamp is most probably smaller than the assumed vapor pressure for the pure octadecanethiol. Also the sticking probability is smaller than 1. Therefore τ will be larger than the lower limit of 17 s, which makes the value of about 200 s for the discussed experiment reasonable.

4.7.2 Patterns of mercaptohexadecanoic acid on Au (μCP)

While octadecanethiol SAMs make a surface hydrophobic due to the terminal methyl group, mercaptohexadecanoic acid SAMs result in a hydrophilic surface. Before combining both thiols to form a chemically micro-structured surface we investigate the properties of microcontact printed mercaptohexadecanoic acid SAMs by SFG microscopy and

---

[2]vapor pressure of octadecanethiol from [74], n_{sites} calculated for a $(\sqrt{3} \times \sqrt{3}R30°)$ structure

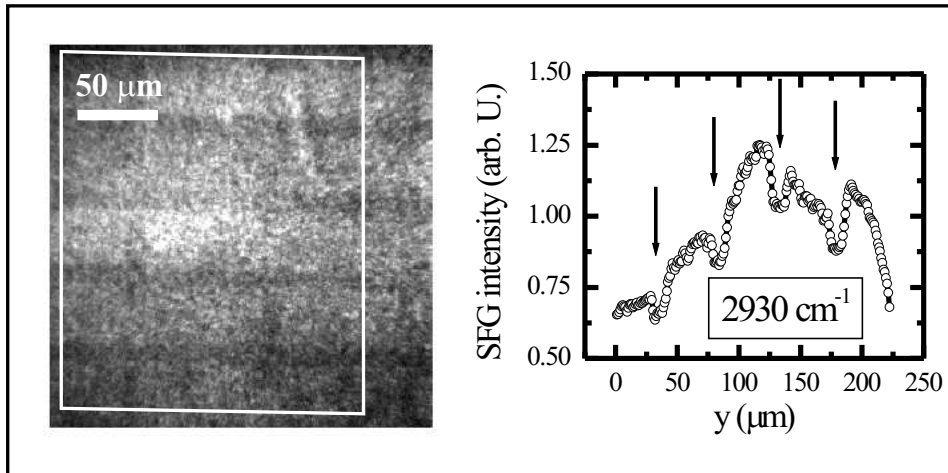**Figure 4.13:** (left) Vibrationally resonant SFM image at $\omega_{IR} = 2930$ cm^{-1}) of a microcontact printed pattern of C_{15}-COOH (acquisition time $= 40$ min, average intensity 30 photons /pixel). (right) The cross section taken within the white box yields a contrast of about 15%. The slow change of intensity is due to the inhomogenous illumination of the sample.
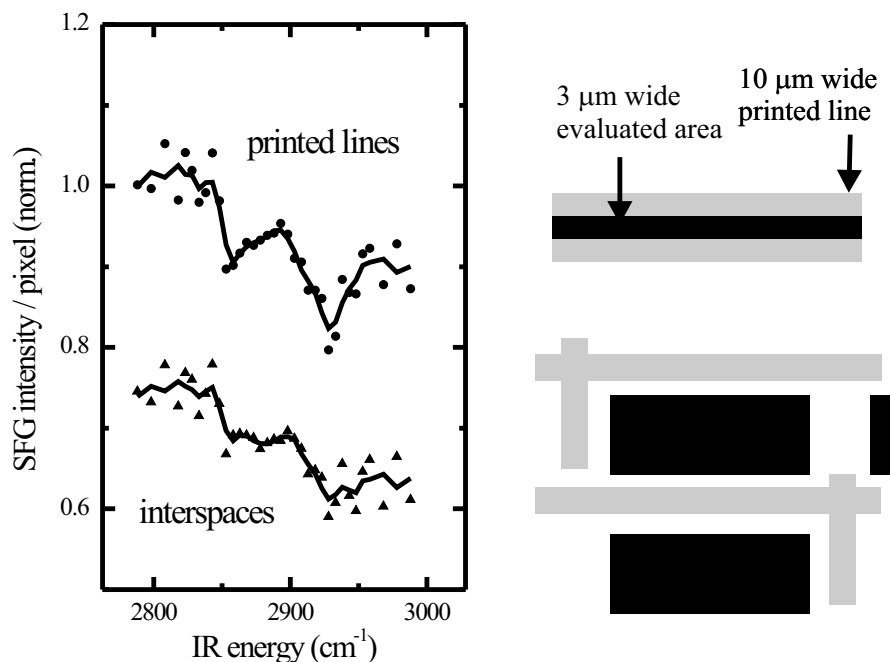
Figure 4.14: Locally resolved spectra of the printed mercaptohexadecanoic acid pattern: In the inner 3 μm of the 10 μm wide lines (top) and in the area between the pattern (bottom, offset by -0.25 units). The pattern is represented by the grey lines in the schematic on the right hand side. The regions, which were evaluated for the respective local spectra, are indicated by the black regions.

spectroscopy.

Fig. 4.13 shows the SFM image of a microcontact printed $C_{15}COOH$-SAM on Au at $\omega_{IR} = 2930$ cm^{-1}, i.e at the antisymmetric methylene stretching vibration (see spectrum in Fig. 4.4). Preparation parameters were an ink concentration of 1.3 mM, 60 s inking time, and 120 s contact time. The pattern is the same as in Fig. 4.9.

The cross section in Fig. 4.13 yields a contrast of $(15 \pm 2)\%$. For the non-resonant image at $\omega_{IR} = 2980$ cm^{-1} the contrast is $(7 \pm 2)\%$. The difference of 7% for $\tilde{\chi}_{nr}'^{(2)}$ between lines and interspace indicates that thiols are also adsorbed between the lines similar as in the case of C_{18}. This is still true if the adsorbate density of a full monolayer of $C_{15}COOH$ is 20% smaller than for C_{18} [81].

This is confirmed by taking images at each point of a spectrum and extracting locally resolved spectra. The upper spectrum in Fig. 4.14 corresponds to a 3 μm wide stripe in the printed pattern. The spectrum corresponds to that of the solution-assembled
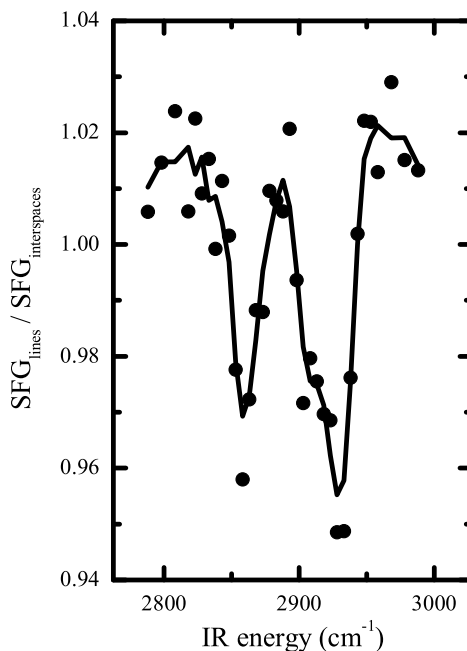
Figure 4.15: Quotient spectrum of the $C_{15}COOH$ SAM obtained from the two spectra in Fig. 4.14. It can be seen that the noise level is reduced very efficiently by dividing the spectrum of the printed lines by the spectrum of the interspaces.

SAM. The vibrational resonances, however, show only about half the intensity of the ones of the solution self-assembled SAM. Due to the finite optical resolution of the SFM (see section 3.2.3), the spectrum for a given pixel in the image will include some crosstalk of the spectra of the surrounding pixels. However, we confirmed by numerical convolution with an Airy function corresponding to the spatial resolution of the SFM that the 3 μm wide evaluated areas (Fig. 4.14, top right) exhibit a signal contribution of less than 1% from outside the 10 μm wide lines. The lower peak intensity thus indicates a lower density of adsorbed molecules or a difference in order compared to the solution-assembled $C_{15}COOH$-SAM.

The spectrum of the region between the printed pattern (Fig. 4.14 bottom) exhibits also a methylene signature.

"On-substrate" calibration

The possibility to compare the spectra of different regions within the field of view can be used to enhance the sensitivity in SFG spectroscopy. The SNR in SFG spectra can be reduced by several effects: One source of noise are fluctuations in the laser pulse

energy and beam shape. A long time drift in the IR output energy can induce a slope in the spectra. Absorption lines in the medium above the sample may induce systematic artifacts, especially if one measures in the range of water vibrations. These influences are reduced efficiently by "on-substrate" calibration in sum-frequency microscopy:

Fig. 4.15 shows the ratio of the upper spectrum and the lower spectrum in Fig. 4.14. Fluctuations of the laser intensity (as seen in Fig. 4.14) cancel very efficiently by this method. The slope in the non-resonant signal signal vanishes. The noise level of the spectrum is reduced by a factor of 2-3 in comparison to the local spectra. If the noise was uncorrelated it should increase by a factor of $\sqrt{2}$ due to the division of the spectra.

We employed this "on-substrate" normalization to search for a signature of the vibration of the COOH group in the region from 2400 cm^{-1} to 3720 cm^{-1} in order to use this signature for discrimination of C_{15}COOH and C_{18} thiolates. The noise level was 3% of the background or lower. However, no resonance could be found. Possible explanations for the absence of a resonance of the carboxyl-group in the SFG spectra were already discussed in section 4.4.2.

4.7.3   Printed lines of C_{18} − post-adsorption of C_{15}-COOH from solution

From the application point of view it is desirable to pattern a surface not only with a single functionality, but rather to define distinct areas with differing chemical activity on the same substrate. This is achieved by combining microcontact printing and assembly from solution. The results of this and the following section give new insight into the exchange and reorientation of thiolate SAMs during the filling up of microcontact printed SAMs with a different thiol species from solution.

Thiolate SAMs patterned with hydrophilic and hydrophobic functionalities were prepared by first micro-contact printing octadecanethiolate (ink concentration 1 mM, inking 60 s, contact 120 s) then immediately immersing the sample in a solution of mercapto-hexadecanoic acid (1 mM) for 15 min. Measurements for a printed monolayer of C_{18} and a solution-assembled monolayer of C_{15}-COOH (sections 4.5 and 4.4.2) are used as reference for this SAM with an inscribed chemical pattern. Both spectra are displayed in Fig. 4.16.

Images of the SAM with the chemical pattern were taken at three IR frequencies (Fig. 4.17a-c). 2860 cm^{-1} and 2880 cm^{-1} were chosen to provide the chemical selectivity to
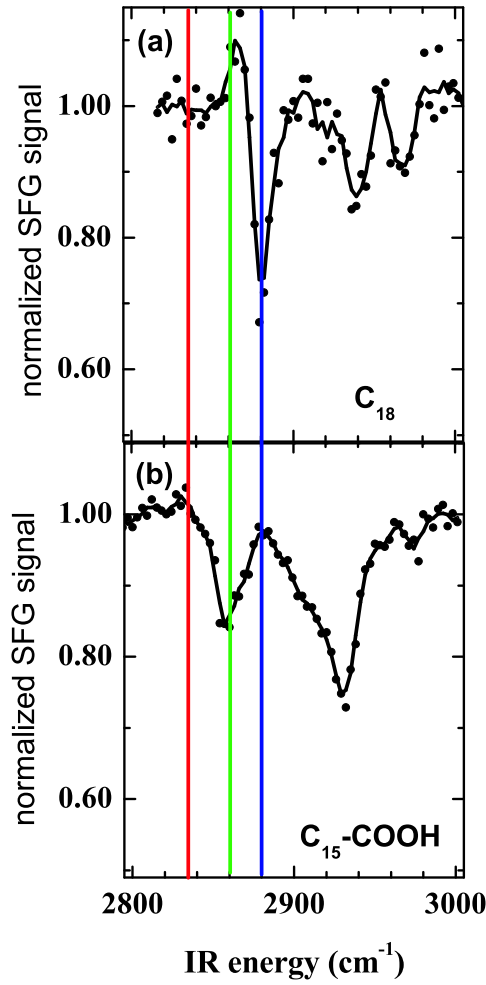
Figure 4.16: SFG spectra of homogeneous thiolate layers: (a) octadecanethiolate monolayer micro-contact printed with a flat PDMS stamp and (b) mercaptohexadecanoic acid monolayer adsorbed from solution. The IR frequencies of the three measurements in Fig. 4.17 are marked and color-coded.

the two thiolates because for these frequencies there is no overlap between their spectra (Fig. 4.16). The image at 2835 cm^{-1} provides contrast specific to the SFG signal from the Au surface and monitors the density of Au-thiol bonds (see section 4.6).

Fig. 4.17 (d-f) shows the pattern evaluated using eqs. 2.38 and 2.39. In order to allow the direct comparison of $\tilde{\chi}_{res}^{(2)}$ with the peak height in the normalized spectra in Fig. 4.16, $I_{nr}(0)$ is replaced by the average of $I_{nr}(\Theta)$ in the images; this constant is about 30% smaller than $I_{nr}(0)$.

The contrast in Fig. 4.17d is small indicating a small difference in thiolate coverage; if the two phases had identical densities of sulfur-Au bonds, this contrast would completely vanish. What is surprising is that the contrast observed in Fig. 4.17e,f is also small and significantly smaller than expected from the spectra of the pure phases (Fig. 4.16).
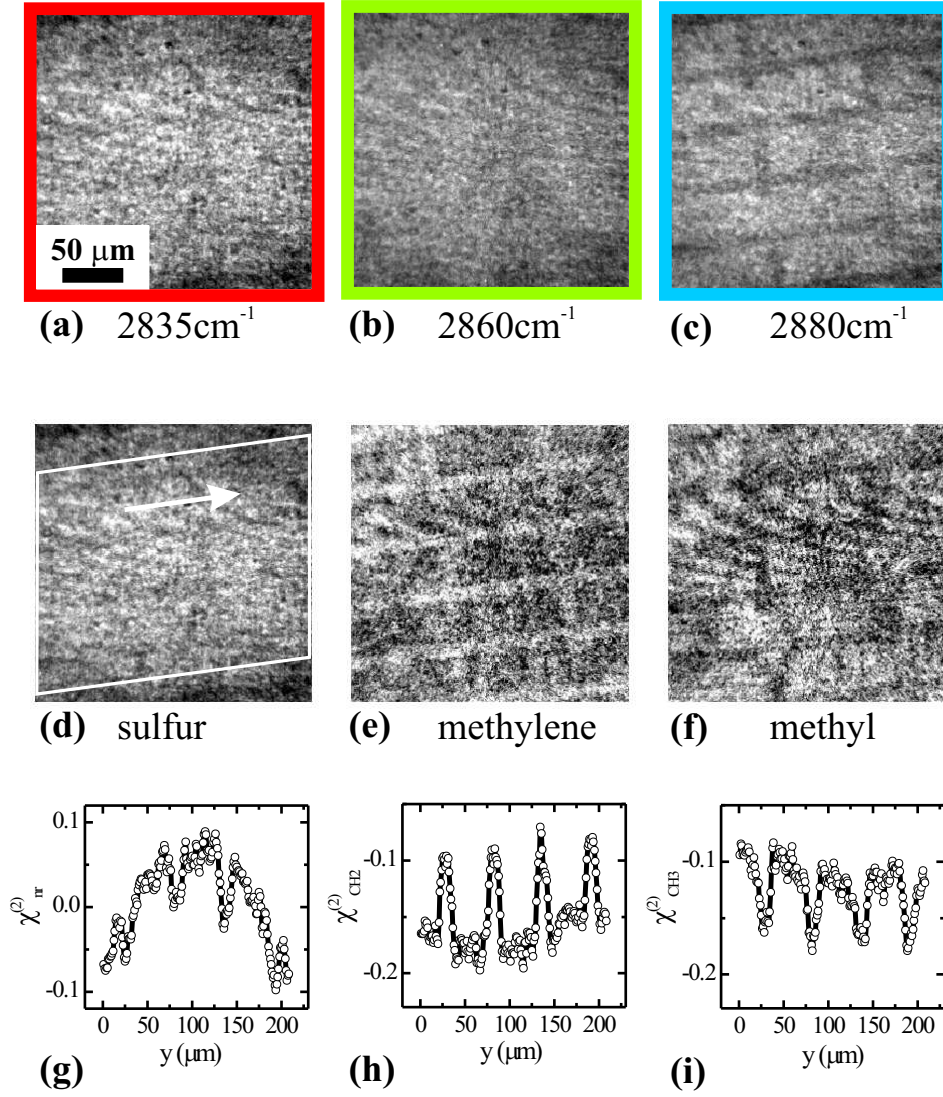
Figure 4.17: (a-c) Original SFG images (acquisition time=135 min) at the three IR frequencies corresponding to the lines in Fig. 4.16: (a) non-resonant, (b) at the symmetric methyl stretch, (c) at the symmetric methylene stretch. (d-f) Processed data, using eq. 2.38 and eq. 2.39: (d) "sulfur-image", (e) "methylene-image", (f) "methyl-image". (g-i) Cross sections through the stripe pattern in (d-f) with the intensity integrated parallel to the stripe direction (arrow in (d)). The contrast is discussed in the text and the color code corresponds to Fig. 4.16

Chemical contrast line/interspace:

C$_{18}$ (μCP,120 s), C$_{15}$COOH (solution)

$\tilde{\chi}_i^{(2)}$	sample (immersion times)	
	sample 1 (15 min)	sample 2 (20 min)
$\tilde{\chi}_{nr}^{(2)}$	0.07	0.08
$\tilde{\chi}_{CH2}^{(2)}$	-0.09	-0.05
$\tilde{\chi}_{CH3}^{(2)}$	0.08	0.07

Table 4.5: Chemical contrast between printed lines and interspace evaluated with eqs. 2.39 and 2.38.

Coverage difference line/interspace (% of the respective monolayer)

C$_{18}$ (μCP,120 s), C$_{15}$COOH (solution)

	sample (immersion times)		
	1 (15 min)	2 (20 min)	3 (15 min)
adsorbate	21%	24%	24
C$_{15}$COOH	-43%	-24%	-23%, *loc. spec*
C$_{18}$	27%	24%	23%, *loc. spec.*

Table 4.6: Coverage difference between printed line and interspace in percent of a full monolayer of the respective thiolate (Fig. 4.16). The values denoted by *loc. spec.* for sample 3 are derived from the fit of local spectra for the printed lines and the interspace respectively (see text).

As a result the contrast is only slightly larger than the dominating photon noise in the images (accumulated SFG intensity $\approx$ 30 photons/μm^2). The low contrast is a property of the monolayer and not due to the imaging because the large acceptance angle of the microscope (see chapter 3) collects even high diffraction orders of the pattern. Numerical contrast values are obtained from cross sections perpendicular to the stripes of the printed pattern in Fig. 4.17g-i. They are listed in table 4.5 for sample 1. For each point of the cross section the intensity is integrated parallel to the direction of the stripes (arrow direction in Fig. 4.17f). The vertical stripes in the pattern are neglected (as in section 4.7.1) because they represent less than 5% of the evaluated region. Fig. 4.17h,i demonstrate that the contrast is inverted when the IR beam is tuned from a resonance of one thiolate to the resonance of the other.

$\tilde{\chi}_{nr}'^{(2)}$ is a measure of the adsorbate density. The edge of a macroscopic printed C$_{18}$ monolayer exhibits a non-resonant contrast of $\approx$ 33% (subsection 4.6). Taking this

value for calibration we obtain the result that the post-adsorbed regions have a total thiolate coverage, which is 21($\pm$5)% of a monolayer lower than the printed regions. This difference may be explained by a less compact structure, in which $C_{15}COOH$ thiolates arrange in agreement with the observation of substantial deviations from the all-trans configuration of the alkane backbone, which we concluded from the SFG spectrum (see section 4.4.2). The vibrational contrast can be calibrated with the spectra of the pure phases (Fig. 4.16). $\tilde{\chi}'^{(2)}_{res}(\Theta)$ is proportional to coverage when no substantial reorientation of the molecules occurs. From the contrast we obtain coverage differences between the post-adsorbed and printed regions of -27($\pm$4)% of a complete C_{18} layer and +43($\pm$5)% of a $C_{15}COOH$ layer. The latter value takes into account that a small positive peak in the C_{18} spectrum (see Fig. 4.16a) enhances the contrast at 2835 cm^{-1}. Contrasts of -100% and +100% would be expected if the stripes consisted of the pure phases. The evaluation thus reveals that such a perfect separation is not compatible with observation. The fact that the highest $\tilde{\chi}^{(2)}_{res}$ values in Fig. 4.17h and Fig. 4.17i both do not attain zero but have significant negative values suggests that the SAMs consists of mixed phases of the molecular species.

These results are typically observed for samples prepared with $\sim$ 15 min immersion time (see sample 1 and sample 2 in table 4.5). The according coverage differences for samples 1 and 2 are listed in table 4.6.

The relative SFG intensities in the printed and the post-adsorbed regions indicate the mixing of phases of the two different thiolates. Absolute quantification of the adsorbed species would require that in the SFM image there is also a region of clean Au. The preparation method of contact printing and assembly from solution, however, covers all regions of the gold with the thiolate. Therefore we took advantage of the potential, which SFM offers, and applied SFG microscopy to extract local spectra.

Sample 3 was prepared by first microcontact printing octadecanethiolate (concentration 1.3 mM, inking 60 s, contact 120 s) then immediately immersing the sample in a solution of mercaptohexadecanoic acid (1 mM) for 15 min. The non-resonant contrast between the pattern and the Au region is about 8%, i.e. the adsorbate density is comparable to the sample in Fig. 4.17, although the ink concentration of C_{18} was slightly higher. The points in Fig. 4.18a and b show the normalized spectrum $spec_{lines}(\omega_{IR})$ belonging to the inner 5 μm of the printed lines. The local spectrum $spec_{interspace}(\omega_{IR})$ in the interspace was also extracted. This time the vertical bars of the pattern (Fig.4.9) were excluded.

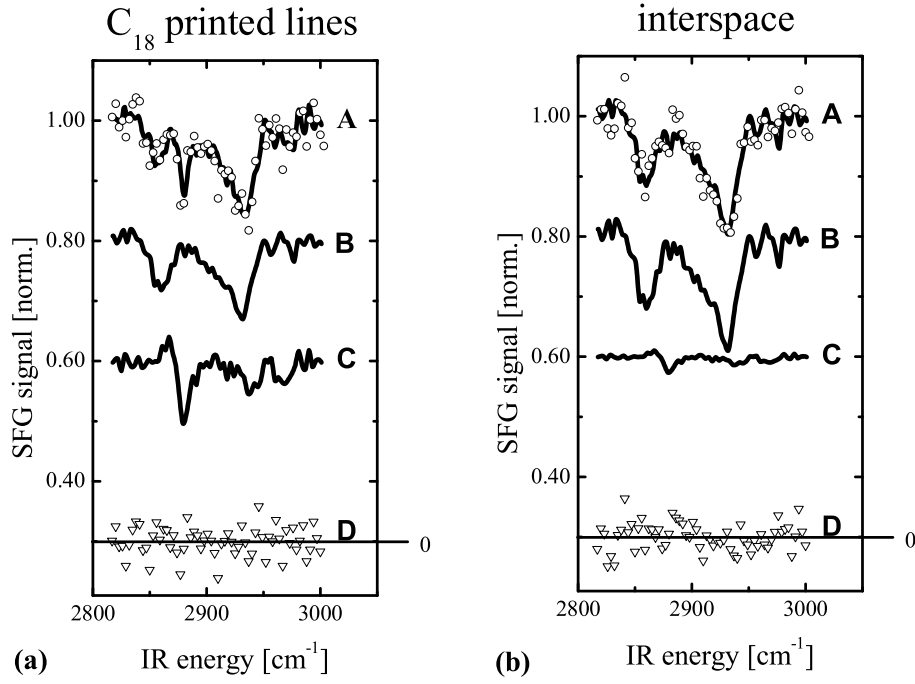The local spectra $spec_i(\omega_{IR})$ (i=lines, interspace)) are fitted by the following func-

Figure 4.18: Local spectra of the printed lines and the interspace for a microcontact printed C_{18} pattern with post-adsorbed $C_{15}COOH$ from solution: (points) data/slope (see text), (A) fit, (B)$a_{C15COOH} \times spec_{C15COOH}$, (C) $a_{C18} \times spec_{C18}$, (D) fit-data

tion:

$$
spec_i(\omega_{IR}) = \frac{data(\omega_{IR})}{b + m(\omega_{IR} - \omega_0)} \tag{4.5}
$$

$$
= \left(\underbrace{1}_{\tilde{\chi}_{nr}^{(2)}} + \underbrace{a_{C18}(spec_{C18}(\omega_{IR}) - 1)}_{\tilde{\chi}_{CH3}^{(2)}} + \underbrace{a_{C15COOH}(spec_{C15COOH}(\omega_{IR}) - 1)}_{\tilde{\chi}_{CH2}^{(2)}} \right)
$$

The normalization of the data with a slope represented by the denominator in the center allows the fit with the vibrational signatures on the right-hand side. The initial 1 on the right-hand side accounts for the non-resonant Au SFG signal. The second term is the spectral contribution of the methyl group in the reference spectrum of a printed C_{18} monolayer (Fig. 4.16a), i.e the 1 corresponding to the non-resonant Au signal in that spectrum is subtracted. The third term represents the contribution of the methylene groups in a self assembled C_{15}-COOH monolayer from solution (Fig. 4.16b). Fitting parameters are the slope m, the offset of the non-resonant signal b and the weighting factors a_{C18} and $a_{C15COOH}$.

The solid line (A) (Fig. 4.18a+b) is the result of the fits by nonlinear regression. The obtained weighting factors are given in table 4.7. The individual spectra scaled

Weighting factors:

C_{18} (μCP,120 s), C_{15}COOH (solution)

	printed lines	interspace
$a_{C15COOH}$	0.51	0.74
a_{C18}	0.31	0.08

Table 4.7: Weighting factors spectra in the fit to the local spectra in Fig. 4.18.

with these weights have been displayed in (Fig. 4.18a+b) as traces (B) and (C). Curve (D) shows the difference between the fit and the data in (A). No indication of additional peaks is observed in (D), i.e. the local spectra are within the experimental uncertainty a linear superposition of the two reference spectra.

The differences in the weighting factors for one species between lines and interspace correspond to the coverage difference in units of a full monolayer of the respective thiolate. The values are listed in Tab. 4.6 for sample 3.

The results of local SFG spectroscopy in Fig. 4.18 confirm the results obtained from the SFM images. Mixing of thiolates occurs in the printed lines as well as in the interspace. The findings will be discussed in more detail in section 4.7.5. Before that the results for the inverse preparation path are presented in the following section.

4.7.4   Printed lines of C_{15}-COOH $-$ C_{18} from solution

In section 4.4 it was shown that SAMs of carboxyl-terminated thiols differ from alkanethiolate SAMs with respect to order and gauche defects. Therefore the stabilization due to the van-der-Waals interaction between the methylene groups is presumably reduced. On the other hand the mercaptohexadecanoic acid thiolate monolayer is stabilized by lateral hydrogen bonding [80, 81, 83]. Therefore it is of interest investigate, if the order of preparation influences the result, i.e. the chemical micro-structure. In this section the results of the reversed preparation process to the one in section 4.7.3 are presented.

Fig. 4.19 shows the measurements of a microcontact printed C_{15}COOH-SAM (concentration 1 mM, 60 s inking, 120 s contact), which was immersed into a 1.3 mM solution of C_{18} for 15 min. The SFM images were taken at the corresponding IR frequencies as for the sample in section 4.7.3, i.e. at ω_{IR} = 2830 cm^{-1}, 2860 cm^{-1}, and 2880 cm^{-1} (Fig. 4.19a-c). The evaluation of the maps corresponding to the sulfur density as well as to the methylene and methyl groups (Fig. 4.19d-f) and the calculation of the cross
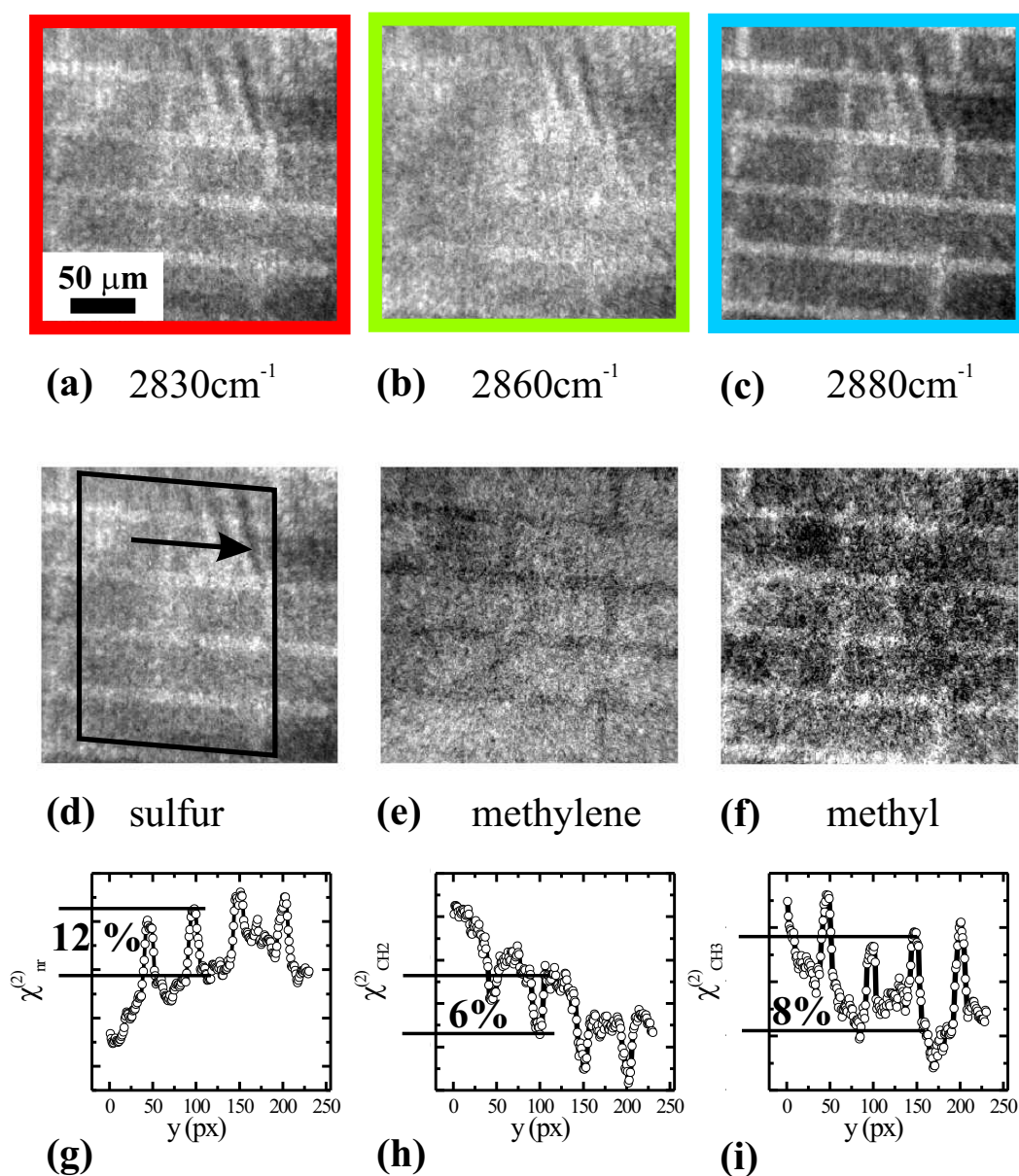
Figure 4.19: (a-c) Original SFG images (acquisition time=150 min) at the three IR frequencies corresponding to the lines in Fig. 4.16: (a) non-resonant, (b) at the symmetric methyl stretch, (c) at the symmetric methylene stretch. (d-f) Processed data, using eq. 2.38 and eq. 2.39: (d) "sulfur-image", (e) "methylene-image", (f) "methyl-image". (g-i) Cross sections through the stripe pattern in (d-f) with the intensity integrated parallel to the stripe direction (arrow in (d)). (The contrast is discussed in the text and the color code corresponds to Fig. 4.16)

Chemical contrast line/interspace:

$C_{15}COOH$ (μCP,120 s), C_{18}(solution)

$\tilde{\chi}_i^{(2)}$	sample (immersion times)	
	sample 4 (15 min)	sample 5 (15 min)
$\tilde{\chi}_{nr}^{(2)}$	0.12	0.15
$\tilde{\chi}_{CH2}^{(2)}$	-0.06	-0.11
$\tilde{\chi}_{CH3}^{(2)}$	0.08	0.08

Table 4.8: Chemical contrast between printed lines and interspace evaluated with Eqs. 2.39 and 2.38.

Coverage difference line/interspace: (% of the respective monolayer)

$C_{15}COOH$ (μCP,120 s), C_{18} (solution, 15 min)

	sample		
	sample 4		sample 5
method	SFM	loc. spec.	SFM
adsorbate	36%	–	45%
$C_{15}COOH$	-30%	-25%	-55%
C_{18}	32%	24%	30%

Table 4.9: Coverage difference between printed line and interspace in percent of a full mono-layer (Fig. 4.16). The values in the column denoted by *loc. spec.* for sample 4 are derived from the fit of local spectra for the printed lines and the interspace respectively (see text).

sections (Fig. 4.19g-i) followed the same procedure as in the preceding section.

Table 4.8 lists the contrasts deduced from Fig. 4.19g-i (sample 4) and of another sample (sample 5). Comparing the first and the third column shows that the relations between the different contrasts are similar. Both samples show a significantly higher non-resonant contrast than the samples in section 4.7.3. The deduced coverage differences in respect to a full monolayer are given in Tab. 4.9. The result indicates a mixing of thiolates.

In order to learn more about the composition of the post-adsorbed SAM and to check the consistency of SFM results and local spectroscopy results, spectra (Fig. 4.20) were taken on the sample 4 (Fig. 4.19) and extracted separately for the lines and the interspaces. Both spectra were fitted as described in section 4.7.3. The obtained weighting factors are listed in Tab. 4.10. The coverage difference deduced from the weighting factors are given in the central column of Tab. 4.9. They agree within the
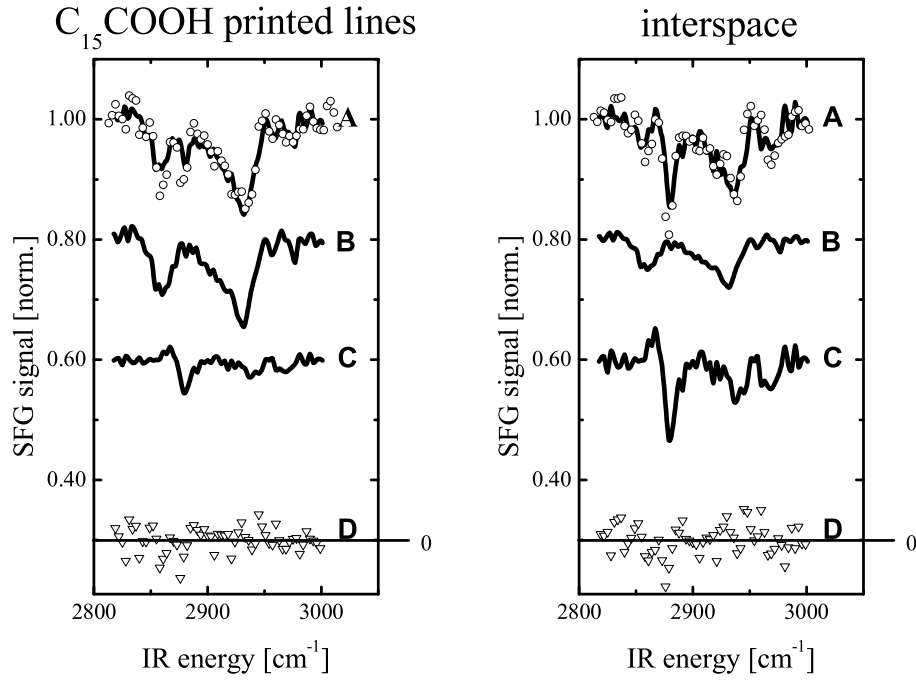
Figure 4.20: Local spectra of the printed lines and the interspace for a microcontact printed $C_{15}COOH$ pattern with post-adsorbed C_{18} from solution: (points) data/slope (see text), (A) fit, (B) $a_{C15COOH} \times spec_{C15COOH}$, (C) $a_{C18} \times spec_{C18}$, (D) fit-data

Weighting factors:

$C_{15}COOH$ (μCP,120 s), C_{18} (solution)

	printed lines	interspace
$a_{C15COOH}$	0.56	0.31
a_{C18}	0.16	0.40

Table 4.10: Weighting factors of the spectra in the fit to the local spectra in Fig. 4.20.

experimental error ($\pm 4\%$ for each value) with the result obtained from the SFM images (Fig. 4.19). Thus the consistency of both evaluations is confirmed. The local spectra prove that a mixing of phases occurres for the lines and the interspaces.

4.7.5   Printed lines – post-adsorption from solution

The patterns produced by microcontact printing and subsequent post-adsorption have a lower chemical contrast than expected from the spectra of separated thiolate phases (Fig. 4.16). The local spectra demonstrate substantial intermixing, which is discussed in this section.

In section 4.7.1 it was shown that thiol transport through the gas phase leads to a substantial coverage of thiolate also in the interspaces. The reduced contrast for a printed pattern of C_{18} (contact time 120 s, Tab. 4.3) indicates a coverage of about 2/3 ML in the interspace. The question, if this sub-monolayer is only filled up during post-adsorption with $C_{15}COOH$ must be answered with no because the vibrational contribution in the local spectrum of the interspace (Fig. 4.18b) corresponds to a C_{18} contribution of 0.08 ML only. The description of the post-adsorption process thus must include the exchange of thiol species.

Starting with the non-resonant contrast $\tilde{\chi}_{nr}^{\prime(2)}$ (Fig. 4.17d and Fig. 4.19d), both thiolate sequences in the process of printing and post-adsorption yield a higher total thiolate coverage (i.e. lower SFG intensity at a non-resonant IR-wavelength) for the area, which shows a predominant C_{18} coverage. These are the lines in the case of printed C_{18} and the interspace in the case of post-adsorbed C_{18}. The higher adsorbate density can be understood by the densely packed $\left(\sqrt{3} \times \sqrt{3}\right) R30°$ structure of alkanethiolates, which are known to form SAMs with a superior order than carboxyl-terminated SAMs [80]. Our results show a similar behavior as the observation by Kakiuchi et al. [81] who concluded from their voltammetry experiments a $\sim 20\%$ lower adsorbate density for $C_{11}COOH$ when compared to C_{16}.

Phases of well ordered C_{18} monolayers can be identified unambiguously by the methyl vibration, which is not present in a $C_{15}COOH$ thiolate phase. As the carboxyl group of the mercaptohexadecanoic acid thiolate is not SFG active we have to use the methylene vibrations as a label for phases of this thiolate. Thin phases of alkanethiolates may also exhibit methylene resonances due to the presence of gauche defects. However, the spectrum for a mercaptohexadecanoic acid SAM differs from that of a sub-monolayer alkanethiolate in position and width of the peaks. The $C_{15}COOH$ spectrum exhibits two distinct peaks at 2860 cm^{-1} and 2930 cm^{-1}, while the alkanethiolate monolayer shows a broad signature with a dominating antisymmetric stretching methylene vibration at 2916 cm^{-1} [37]. The peaks in a $C_{15}COOH$ spectrum are similar to those of an amino-

amido-thiolate [38]. The peak positions are even identical. This strongly suggests that the methylene spectrum (Fig. 4.4) is indicative of a thiolate with strong molecule to molecule interaction by hydrogen bonding. Therefore we can assume that this $C_{15}COOH$ spectrum, which is used for fitting the local spectroscopy data of the post-adsorbed samples in the sections 4.7.3 and 4.7.4, is specific to the $C_{15}COOH$ phase. For the following discussion we assume that no substantial reorientation of the chemical groups happens during the post-adsorption because the exchange process of thiolates happens domain-wise [81, 97]. Under these two assumptions the weighting factors obtained by the nonlinear fits represent the coverage in percent of a full monolayer of the respective thiolate.

For the printed $C_{15}COOH$ pattern post-adsorbed with C_{18} (Fig. 4.20a) the weighting factor $a_{C15COOH} = 0.56$ corresponds to a coverage of $C_{15}COOH$ of about one half of a solution assembled monolayer. This is in accordance with the results of section 4.7.2, where the vibrational peaks of a printed $C_{15}COOH$ have half the size of the SAM assembled from solution, indicating a different kinetic behavior of SAM assembly when compared to C_{18}. The methyl peak at $\omega_{IR} = 2880$ cm^{-1} in the local spectrum (Fig. 4.20a) and the value of $a_{C18} = 0.16$ (Tab. 4.8) shows that C_{18} fills up parts of the printed $C_{15}COOH$ lines.

Substantial amounts of both thiolate species are detected by local SFG spectroscopy in the interspace of the same sample (Fig. 4.20b). We did not quantify the absolute amount of mercaptohexadecanoic acid, which was transferred to the interspace by the vapor phase (section 4.7.2), but the observed 1/3 of a full $C_{15}COOH$ layer, demonstrates that a large amount of it is not exchanged during the post-adsorption of C_{18}. Accordingly only 0.4 ML of C_{18} is adsorbed from solution.

The findings for the inverse preparation sequence – i.e. printed C_{18}, post-adsorbed $C_{15}COOH$ – are not equivalent. The octadecanethiol in the printed C_{18} lines is exchanged by $C_{15}COOH$ to such an extent, that mercaptohexadecanoic acid becomes the majority species (Fig. 4.18a and Tab. 4.7). The same result was obtained for the edge of a octadecanethiolate SAM printed with an unstructured PDMS stamp. These findings show, that a C_{15} thiolate with a carboxyl group as terminal group can exchange with C_{18}, which has a longer methylene backbone. Nuzzo et al. estimate a minimum enthalpy gain of 0.8 kcal/mol for each additional methylene group in an alkanethiolate [47]. Thus the enthalpy gain by the interaction between carboxyl groups should be at least 2.4 kcal/mol. Cooper et al. observed for photolithographically patterned SAMs

the replacement of alkanethiolates by carboxyl-terminated thiols, which had 9 methylene groups less [83] on a similar timescale as in our experiments. The fast replacement is due to defects in the SAM, which definitely occur at the edges of the pattern and also in the pattern as the local spectra show. In contrary, homogeneous SAMs as prepared from solution exchange on a slower time scale of ~ 100 h [81].

The approximately 2/3 ML of C_{18} deposited in the interspace during the printing process by vapor transport (see section 4.7.1) are replaced almost completely during the post-adsorption by mercaptohexadecanoic acid (Fig. 4.18b and Tab. 4.7). Thus the submonolayer phase of C_{18} is very susceptible to exchange with $C_{15}COOH$. A similar result was obtained for the flat lying phase of a short alkanethiol (C_4) [83]. The remaining rest of about 1/10 ML (Tab. 4.7) might be attributed to C_{18} at defects, which is assumed to be more resistant against exchange [84].

The comparison of both samples shows that, in contrast to the low-coverage phase of C_{18}, a substantial fraction of the low-coverage phase of $C_{15}COOH$ in the interspace resists the exchange for the opposite preparation sequence (Fig. 4.20b, Trace(B)). This suggests an asymmetry in the exchange process. The same asymmetry of the exchange rates with respect to the preparation sequence is observed for the printed lines. $C_{15}COOH$ replaces printed C_{18} to a large extent(Fig. 4.18a). C_{18} only fills up an incomplete layer of printed $C_{15}COOH$ or replaces it only to a small extent (Fig. 4.20a).

This asymmetry in the replacement is mainly a property of the thiolate combination and to a smaller extent of its surface density, as we observe it in dense phases (printed lines) and thin phases (interspaces). This extends the result presented by Kakiuchi et al. [81] for solution-assembled SAMs. The authors measured the exchange process of SAMs of one species in an ethanolic solution of the other species by voltammetry and STM. They used the thiolate combination of C_{16} and $C_{15}COOH$. For these homogeneous SAMs assembled from solution also an asymmetry in the exchange rates was observed.

The sum of the weighting coefficients (Tabs. 4.10 and 4.7) is smaller than 1 and may indicate a spectroscopically invisible phase. This could possibly be C_{18} with a horizontal orientation of the methyl group [12], or $C_{15}COOH$, which is not hydrogen bonded. This is also supported by the sulphur contrast in Fig. 4.19d and Fig. 4.17d, which suggests that the coverage is not as homogeneous as it appears by the sum of the weighting factors.

In conclusion, we have seen the following processes to occur for thiolates at the Au surface: Transport through the gas phase causes a non-negligible coverage of thiolates also between the microcontact printed patterns. We observed the filling up of incomplete monolayers and the exchange of thiolates during post-adsorption. The exchange is more efficient for the replacement of C_{18} by $C_{15}COOH$ than for the inverse case. These processes explain the experimentally observed mixing of thiolates on Au surfaces.

Chapter 5

SFG spectroscopy on the interface PDMS(C$_{18}$) / air

Microcontact printing of self-assembled monolayers on gold is a straight-forward and economical method to produce chemical micropatterns on different surfaces. In the preceding chapter, as in the literature, the printing process is investigated mainly through the order, density, and structure of the printed SAM. A still open question is, whether an already existing orientational order of the thiol molecules on the PDMS stamp contributes to the fast assembly of well ordered SAMs on the timescale of 3 s to 1 min [74, 89, 90, 98]. Addressing this question, we applied sum-frequency generation spectroscopy to the PDMS/air interface with and without C$_{18}$ molecules (section 5.2), because the method is extremely sensitive to the order of chemical groups and thus molecules with preferential orientation.

The interface of PDMS has a low surface free energy (ca. 21.6×10^{-3} Jm^{-2}), which is reflected in its hydrophobicity. Exposure of PDMS to an oxygen plasma increases the surface free energy and thus the wettability. It is widely accepted that the effect of oxygen plasma on silicone rubbers is to create an increased average number of oxygen atoms bonded to silicon. This makes the surface silica-like [99, 100]. Also the formation of silanol (Si-O-H) groups contributes to the increased surface free energy ([99][1], [101]).

The parameters of plasma etching allow to tune the hydrophilic character of PDMS and thus the interaction with different materials [41][2]. Tan et al. have shown recently the important role of the wettability of the stamp in microcontact printing of proteins [102]. Furthermore, wettability of PDMS is of importance in a wide variety of fields: It can

---

[1]and references therein

[2]and references therein

be used to tailor the properties of microfluidic systems made from PDMS [103]. Water repellency, light weight combined with mechanical robustness, and its hydrophobic recovery after electrical discharges make silicone rubbers also a widely used material for outdoor electrical insulation [104].

PDMS returns to the hydrophobic state after it has been made hydrophilic. This is called hydrophobic recovery. While for electrical insulators this is desired, for other applications mentioned before and for microcontact printing this might be an un-wanted effect. Hydrophobic recovery of PDMS after plasma treatment or electrical discharges has been studied with contact angle measurements, XPS, FTIR-ATR, AFM, SEM and optical microscopy. One mechanism for the hydrophobic recovery discussed in the literature is the diffusion of low molecular weight components (fluids) of PDMS to the surface [100, 105, 106]. These fragments are residues from the polymerization and / or modification process. Re-orientation of the silanol groups from the surface into the bulk and the condensation of silanol groups with consequent cross-linking presumably also contribute to the recovery [99]. Also the re-orientation of non-polar groups from the bulk to the surface was proposed. The re-orientation of the nonpolar groups has not been measured directly but rather proposed indirectly from XPS data [101]. The FTIR-ATR data in [99] do see a plasma induced change in peak intensities for methyl and hydroxyl groups. However no change of intensity is observed during the recovery. Apparently the method is not sensitive enough, as it probes the upper 0.5 μm of the PDMS. The SFG results in section 5.3 represent to our best knowledge the first SFG measurements of the hydrophobic recovery in a polymer. They show, that methyl groups at the outermost surface contribute to the hydrophobic recovery.

5.1   Experimental

The preparation of the PDMS stamps from SYLGARD 184 (supplier Dow Corning) has been described in section 4.3. The structure of the single unit in the polymer is given in Fig. 5.1 on the right.

As PDMS exhibits no non-resonant susceptibility $\chi_{nr}^{(2)}$ the total SFG intensity of PDMS is given by expression (2.34). Thus an SFG signal is obtained only in vibrational resonances. The intensity is substantially lower than for the Au-substrate and does not allow a direct beam alignment on the polymer. The superposition of the visible and the IR beam is therefore done in the following way: A Au surface is placed in the focus of the SFM and the SFG intensity is maximized. At the same time also a possibly homogeneous illumination of the field of view can be realized. Then the PDMS stamp
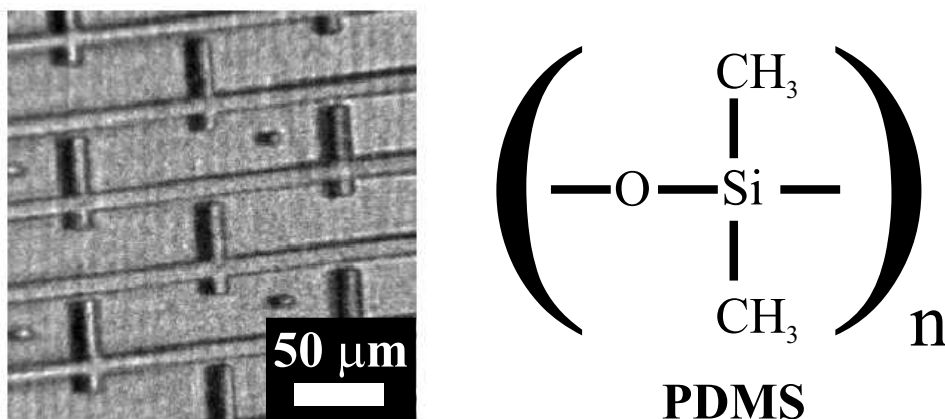
Figure 5.1: (left) Image of PDMS stamp taken in reflection with 450 nm light. The pattern allows to focus on the stamp surface, which is used to establish the overlap of the laser pulses on the stamp (see text). (right) Structure of the PDMS polymer.

is imaged with 450 nm light. The visibility of the pattern allows to focus the stamp (Fig. 5.1), which then is at exactly the same position as the gold sample before. Thus the laser pulses overlap on the stamp within the field of view.

PDMS samples for the study of hydrophobic recovery (section 5.3) were exposed for 15 s to oxygen plasma in a microwave frequency reactor (2.45 GHz, manufacturer Technics Plasma GmbH, Germany). The treatment was performed at maximum power (nominally $\sim$ 190 W), at an oxygen pressure of about 1 mbar. The stamp was then stored under air in a closed box. The relative humidity was between 20% and 30% at 23°C.

Contact angles of water droplets were determined by the sessile drop method with a G10 contact angle measuring instrument (manufacturer Krüss, Germany). MilliQ water (resistance > 18 $M\Omega$) was used. Each measurement is obtained as an average over 12 or more individual water contact angle measurements at at least 6 different positions on the stamp.

5.2 Order on PDMS – Thiol orientation on PDMS stamps

SFG spectroscopy is known to be surface sensitive for centrosymmetric materials (section 2.2.2). This also holds for polymers, in which the random distribution results in inversion symmetry. Wei et al. showed explicitly for the C-H wavelength range that there is no bulk contribution for SFG in reflection from polymers [107]. Therefore the SFG spectra
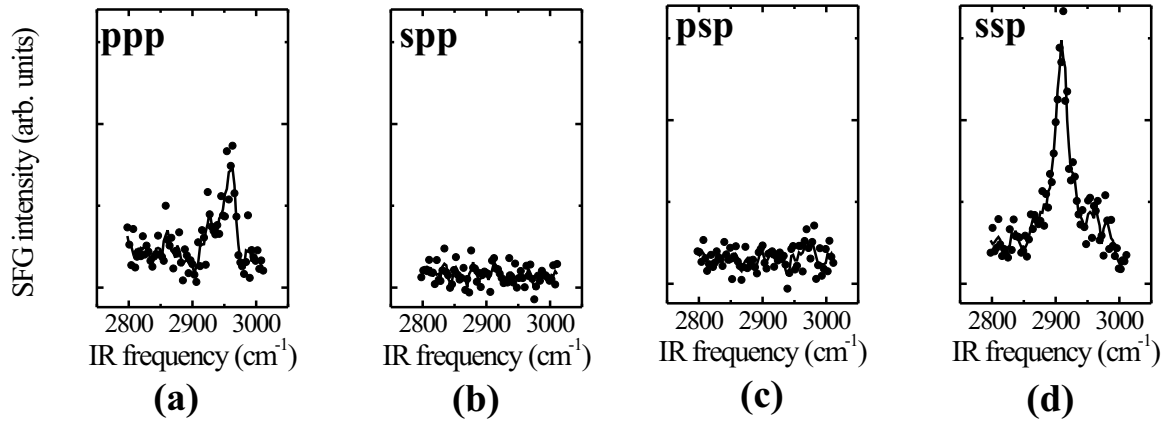
Figure 5.2: SFG spectra for different polarization combinations indicated by the letters in the order SFG, vis, IR. The IR beam was always p-polarized. The baseline is due to a constant offset of the CCD read-out electronics and a background due to diffuse scattering of the visible beam. We checked that the SFG light has a very low non-resonant intensity by blocking the IR beam.

of PDMS monitor the order in the surface layer. In the first part of this section the characterization of the pure PDMS/air interface by SFG spectroscopy is presented. The second part contains the results for a stamp inked with thiol solution.

5.2.1   SFG spectroscopy on pure PDMS

Fig. 5.2 shows the SFG spectra of PDMS with different polarization combinations of the SFG beam and the visible beam. The polarization of the SFG radiation was selected by placing a linear polarizer in front of the microscope. The IR beam is always p-polarized. For spp and psp polarization no vibrational feature is observed (Fig. 5.2b+c) because these combinations do not belong to the four combinations, which can give rise to a signal from an isotropic interface (see Tab. 2.1). The vibration at 2909 ± 3 cm^{-1} measured for ssp (Fig. 5.2d) can be attributed to the symmetric C-H stretch of Si-CH$_3$, while the antisymmetric C-H stretch is observed in ppp polarization at 2962 ± 3 cm^{-1} (Fig. 5.2a) [108][3]. The combination ssp probes the tensor element $\chi^{(2)}_{yyz}$ (Tab. 2.1). The observation of a strong symmetric methyl vibration and the fact that the antisymmetric one is hardly observed for the ssp combination indicate an orientation of the methyl group more or less perpendicular to the surface. The strength of the resonance shows also an order with respect to the preferential orientation of the methyl group either pointing from the surface or into the surface. At first sight the dominating antisymmetric
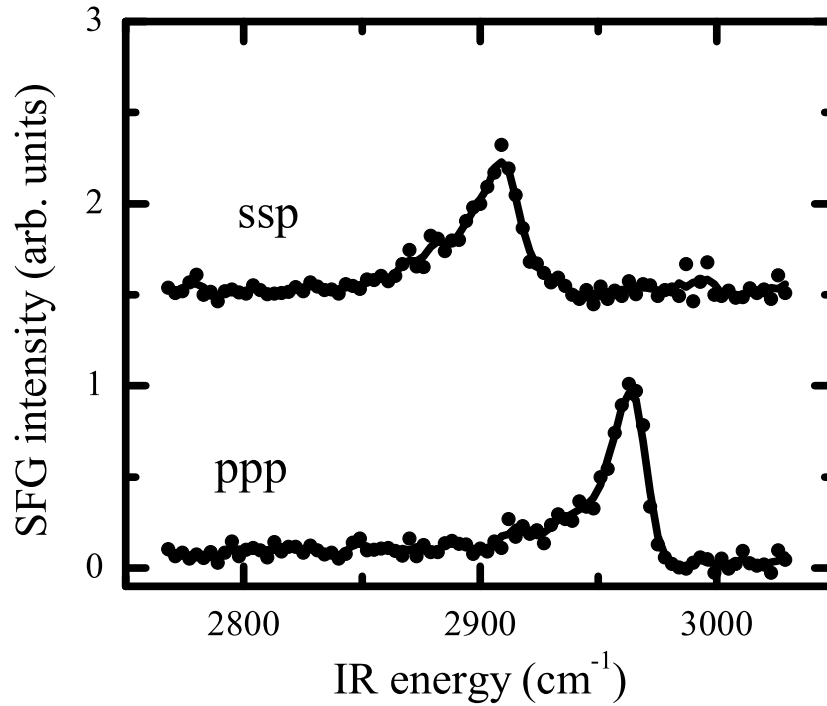
---

[3]and references therein

Figure 5.3: SFG spectra of spin-coated PDMS. They resemble the ones obtained on stamps. Thus the surface in respect to the methyl group is about the same for both preparation methods.

vibration for ppp seems to be surprising, as the IR beam is still p-polarized. However, the ppp polarization combination probes all four independent tensor elements (Tab. 2.1). The respective nonlinear Fresnel coefficients obviously lead to a dominating contribution of $\chi_{yzy}^{(2)}$. This tensor element represents an IR dipole moment oriented parallel to the surface (as indicated by the third index y). For a methyl group oriented perpendicular to the surface this is just the antisymmetric stretching vibration. In fact, this corresponds to the results of Zhang et al [108], who observed the antisymmetric stretching vibration on thin PDMS films for sps (see Tab. 2.1). As there is only one polarization of the SFG beam for a given visible input polarization, we did in the following not use a polarization analyzer for the SFG light.

Most SFG studies on polymers were done on thin films, prepared by spin-coating or solvent casting. They are exposed to air during the curing procedure. In contrast the surface of stamps used for microcontact printing in the studies here is in contact with polystyrene or silicon during polymerization (see section 4.3). In order to cross check, whether the results can be compared, we did also SFG spectroscopy on spin-coated PDMS on quartz. These spectra with better statistics than in Fig. 5.2 are shown in Fig. 5.3. The peak positions, are identical with the ones obtained for PDMS stamps

within experimental error and the vibrations are observed for the same polarization combinations. Also the asymmetric shape is found for both types of PDMS samples. Thus the orientation of the methyl group at the surface is similar for casted PDMS films and thick PDMS stamps.

5.2.2   SFG spectroscopy on inked PDMS(C_{18})
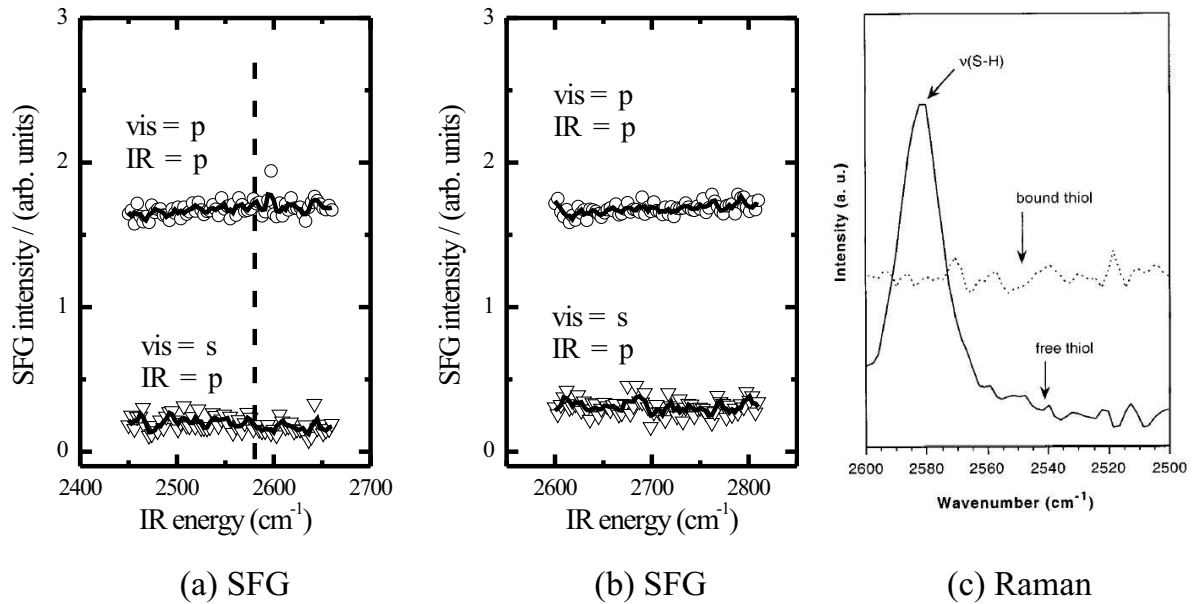

(a) SFG   (b) SFG   (c) Raman

Figure 5.4: SFG spectra of PDMS inked with octadecanethiol (C_{18}). The dashed line marks the IR frequency of the S-H stretching vibration for the free dodecanethiol (C_{12}). The spectra have been offset for clarity. (c) Raman spectrum of free C_{12} (solid line), from [109].

The SFG spectra of pure PDMS demonstrate that there is a preferential orientation of the methyl groups. Therefore the thiols deposited during inking on the PDMS surface might exhibit also a preferential orientation. Such an order could also be induced by the interaction of the unpolar CH_3 group with the unpolar PDMS surface or by a repulsive interaction of the polar S-H group with the PDMS. We expected that, if such an order exist, this should give rise to a resonant SFG signal. As PDMS does not contain S-H groups, the order of the alkanethiol may be probed with the S-H stretching vibration at the IR frequency of about 2580 cm^{-1}. The solid line in Fig. 5.4c is the Raman spectrum of free dodecanethiol (C_{12}) [109]. The vibration is well separated from the C-H frequency range and thus from the peaks of PDMS.

An inked PDMS stamp was prepared by letting a drop of 1.3 mM solution of octadecanethiol (C_{18}) in ethanol dry on the stamp. This procedure was repeated two to

five times in order to saturate the bulk[4]. The deposited amount of thiol corresponds to several hundred monolayers of alkanethiolate on Au. Fig. 5.4a+b show the SFG spectra for the denoted polarizations of the visible and the IR beam. The spectra cover the IR energy range from 2450 cm^{-1} to 2810 cm^{-1}. By blocking the IR beam we checked that the non-resonant SFG intensity is smaller than 0.1 units on the scale. The vertical scale is the same as in Fig. 5.3. As the pulse energies are about the same for the PDMS samples with and without C$_{18}$, this means that the S-H resonance is not seen in the spectra at a noise level corresponding to less than 1/4 of the asymmetric methyl peak of PDMS in Fig. 5.3.

The methyl groups of thiolates in SAMs exhibit three distinct vibrations at 2880 cm^{-1}, 2939 cm^{-1}, and 2967 cm^{-1} (see Tab. 4.1). Therefore at least two resonances are clearly separated from the transitions of the methyl in the PDMS. This is why we also measured for the samples ppp and ssp SFG spectra in the IR frequency range from 2800 cm^{-1} to 3000 cm^{-1}. No difference in the spectra before and after the inking of C$_{18}$ was observed.

Discussion

The S-H stretching vibration is IR as well as Raman active [109]. Therefore it should in principle be observable in SFG spectroscopy. However, we found no observation of the S-H vibration by SFG in the literature. We will briefly discuss possible reasons, why no S-H stretching vibration is seen in our experiment:

A first cause can be a too small resonant first order nonlinear susceptibility $\chi^{(2)}_{SH}$. According to the equations (2.11) and (2.12) the reasons for this could be a small hyperpolarizability β or a low density of thiol molecules N. From the results we cannot exclude either possibility.

The S-H group should behave similarly to the homologous O-H group. It is assumed, that for plasma-etched PDMS there is a substantial amount of hydroxyl groups at the surface [99]. However, we did not observe any SFG signal of the OH group on plasma-etched PDMS, which might indicate a low SFG cross section (see also the following section).

Thiols do also diffuse into the stamp (path 1 in Fig. 4.11). It has been shown that molecules of a 10 mM ink of C$_{16}$ appear after 5 min on the other side of an 1 mm thick sheet of PDMS [74]. Therefore the thiols may have diffused into the stamp during the minimal time of 30 min between inking and first SFG measurement. On the other hand

---

[4]On other samples we also applied the standard method as used in chapter 4, i.e. we inked the stamp for 60 s. The results did not differ from the ones by the method of repeated inking and drying.

the vapor phase transport (section 4.7.1) suggests, that C_{18} molecules are present at the surface at least for several minutes after inking. A possible experiment to check if diffusion into the bulk is the reason that the S-H stretch is not observed, would be the measurement of PDMS stamps, which have been saturated in a thiol solution.

The methyl group and methylene groups of C_{18} are not observed either. Apart from a low surface density another reason for the non measurable SFG signature of the alkanethiols might be a full orientational disorder of the C_{18} molecules at the stamp surface (This holds likely also for the hydroxyl groups mentioned above.).

5.3   Hydrophobic recovery of PDMS after oxygen plasma treatment

SFG spectroscopy can monitor the presence and order of a specific chemical group of the PDMS interface during hydrophobic recovery on the molecular scale. To correlate this with the macroscopic properties of the interface, we did also contact angle measurements, which give information on the hydrophilicity and thus on the surface free energy.

SFG measurements

The SFG spectra were measured on a PDMS stamp, which was plasma etched for 15 s at a power of 190 W. A patterned stamp was used, in order to facilitate the overlapping of the laser pulses (section 5.1). For a typical spectrum 10 runs with 100 shots per data point were measured. The peak height was determined by taking the maximum value of a 3 point smoothed curve. Before and after a spectrum is recorded, the SFG intensity was measured on a gold reference. The average of these two values was used for calibrating the peak height with a reproducible standard. The measurements on different days were taken at the same position on the stamp and on the Au substrate within a precision of better than 1 mm.

Fig. 5.5 shows the development of the SFG intensity in the asymmetric (ppp) and the symmetric (ssp) methyl stretching vibration during hydrophobic recovery. The intensity increases for both vibrations showing an increasing density of ordered methyl groups at the surface. The vibrations are detected already in the first measurement about 1 h after plasma etching. This is also the case for a plasma etching duration of 5 min, indicating that the plasma rather leads to a mild oxidation, which does not remove all methyl groups and which does not destroy their order at the surface completely.

The SFG intensity is quadratic in the density of the probed groups (equations 2.34
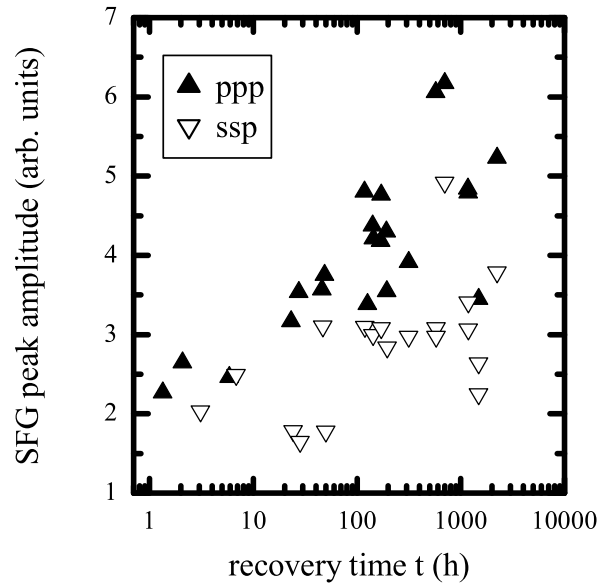
Figure 5.5: SFG peak amplitudes of a oxygen plasma treated sample after the recovery time t for the symmetric methyl stretching vibration (open triangles) and the asymmetric one (filled triangles) (logarithmic time scale).

and 2.12). In order to obtain a characteristic time, we fitted the data in Fig. 5.5 with an exponential recovery function

$$I_{SFG} = \left(N_0 + N_1 \left(1 - exp^{-t/\tau}\right)\right)^2 \qquad . \tag{5.1}$$

It models an initial fast increase in intensity, which then reaches a saturation value. The fitting parameters N_0, N_1 and τ are given in Tab. 5.1 and the fit is displayed graphically in Fig. 5.6.

The fit yields for both stretching vibrations a recovery time on the scale of 100 h and an increase in the adsorbate density of 30% of the initial value. A fit of the data with $N_0 = 0$ (i.e. under the assumption that the plasma removes all ordered methyl groups) is far from a satisfying agreement with the data.

| | **fit parameter** | | | |
polarization	N_0	N_1	τ (h)	$\frac{N_0+N_1}{N_0}$
ppp	1.64 ± 0.10	0.58 ± 0.11	122 ± 50	1.35
ssp	1.39 ± 0.14	0.42 ± 0.14	105 ± 86	1.30

Table 5.1: Fit parameter according to eq. (5.1) for the SFG results on the hydrophobic recovery of PDMS (data in Fig. 5.5).
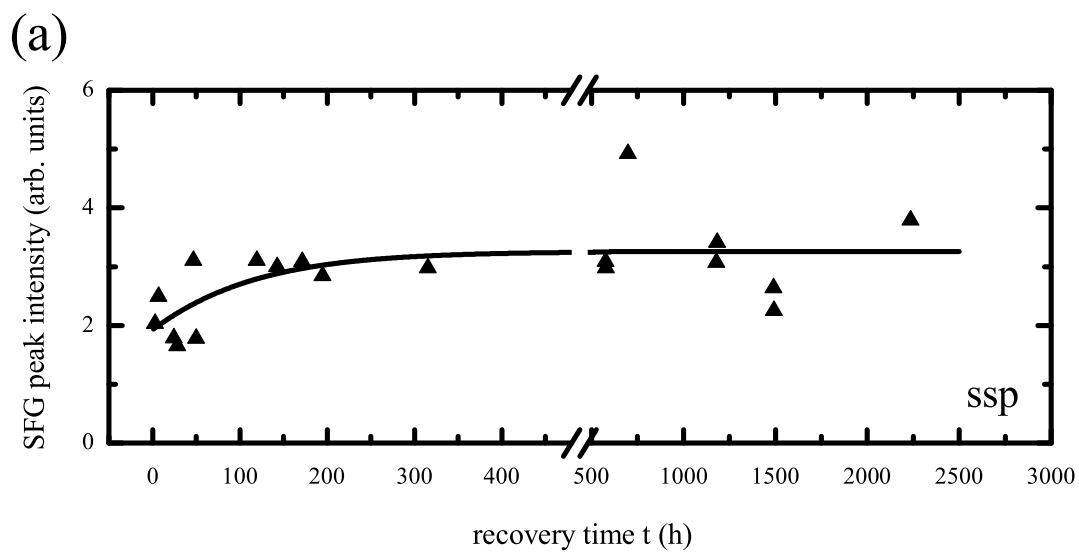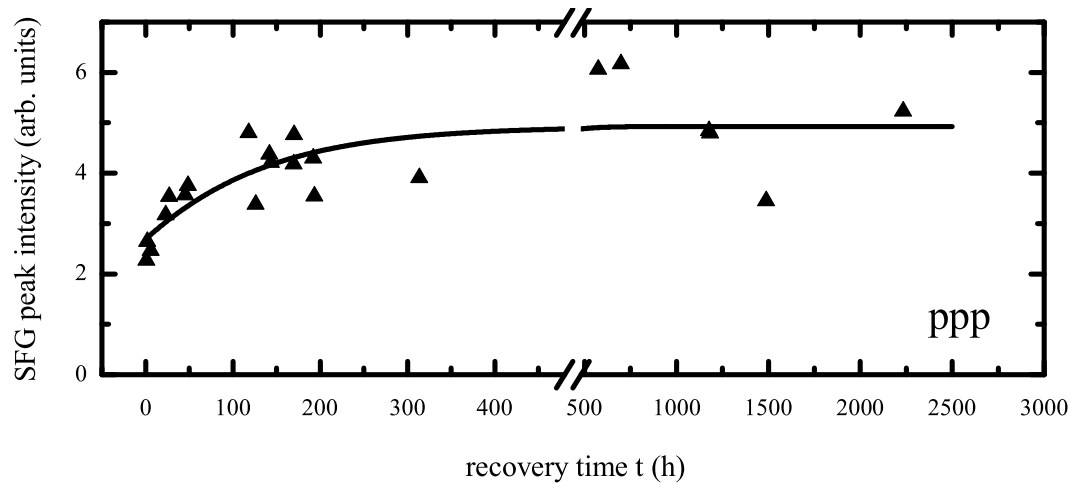
(a)

(b)

Figure 5.6: SFG peak amplitudes as in Fig. 5.5. The solid lines are the fit with the empirical function 5.1. (a) ppp polarization. (b) ssp polarization. Note the different time scales for $t < 500$ h and $t > 500$ h.
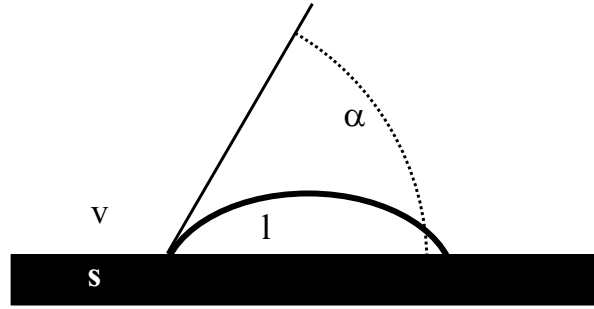
Figure 5.7: Definition of the contact angle. α denotes the angle between surface and the tangent at the liquid phase (l) at the position, where it intersects with the solid (s) and the vapor (v) phase.

Contact angle measurements

As a control measurement we recorded the hydrophobic recovery of PDMS with the water in air contact angle α, which is defined as the angle between the surface and the tangent of the liquid phase at the intersection point of solid (s), liquid(l), and vapor(v) phase (Fig. 5.7). In equilibrium the contact angle relates the respective surface free energies $\gamma_{phase1,phase2}$ through Young's equation [80, 110]:

$$\gamma_{lv} \; cos\alpha = \gamma_{sv} - \gamma_{sl} \tag{5.2}$$

For a hydrophilic surface the interface substrate/water tends to increase resulting in a small contact angle. If the substrate is hydrophobic, the area of the interface substrate/water decreases corresponding to an increased contact angle.

The inset in Fig. 5.8 shows the contact angle α of an unstructured PDMS stamp as a function of time after exposure to an oxygen plasma for 15 s at a power of 190 W (see section 5.1). For t< 1 h we obtained $\alpha \leq 4°$, the minimal value measurable in our contact angle measuring instrument. The contact angle increases from a value $< 4°$ to over $80°$ within the time of the experiment (t> 1000 h). It does not reach a saturation value during this time. It is known from literature that the contact angle of similarly treated PDMS recovers to a value, which is 80-100% of the value of the untreated PDMS [99, 100]. For untreated PDMS samples a contact angle of $\alpha = 110°$ was measured. Therefore the recovery observable by contact angle measurements is not completed on a timescale of about 1000 h. The hydrophobic recovery on the timescale of ~ 1000 h is typical for a wide range of plasma parameters [99, 100, 105].

Fig. 5.8 shows the cosine of the contact angle, which – according to (5.2) – depends linearly on the difference of the surface free energies of the solid phase, i.e. of PDMS. The solid line is a fit of the data with a first order exponential decay. It yields a decay time
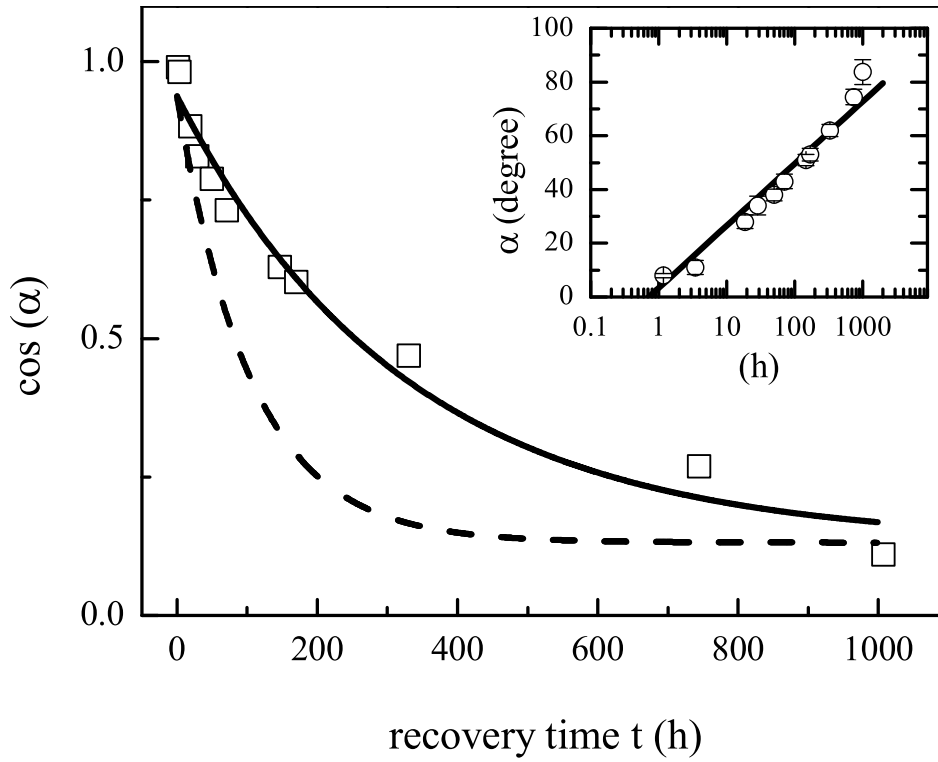
Figure 5.8: Cosine of the contact angle of a oxygen plasma treated PDMS stamp. An exponential fit (solid line) yields a decay time $\tau_{cos\alpha} = 323 \pm 65$ h. The inset gives the contact angle for a logarithmic time scale. The hydrophobic recovery does not reach saturation after 1000 h. The dashed line is the calculated decay for $\tau = 105$ h, the value, which has been obtained in the SFG experiment (see also text).

$\tau_{cos\alpha} = 323 \pm 65$ h. For comparison the dashed line gives the decay for the characteristic time $\tau = 105$ h measured in the SFG experiment. Tab. 5.2 lists the recovery times obtained by both methods.

<div align="center">

Recovery times PDMS

method	contact angle	SFG	
physical property	cos (α)	peak amplitude	
		symmetric stretch	asymmetric stretch
recovery times	323 ± 65 h	105 ± 86 h	122 ± 50 h

</div>

Table 5.2: Recovery time of the surface free energy as obtained by contact angle measurement and recovery time by fitting the peak amplitudes of the methyl resonances (see text).

Discussion

The SFG results monitor the increase of the ordered methyl group density at the interface, which contributes to the hydrophobic recovery of PDMS. The average intensity of the peaks measured by SFG increases in the first 200 h and then stays constant within the variations of the individual measurements (Fig. 5.6). In contrast to that, $\cos(\alpha)$, which is correlated to the surface free energy by eq. (5.2), decreases in the time between t=200 h and t=1000 h by more than half of the total observed change (Fig. 5.8). This suggests, that a slower process is involved in the hydrophobic recovery. The initial faster decay for the data points (Fig. 5.8) in comparison to the exponential fit hints also in the direction, that at least two recovery processes are involved. This could explain, why the recovery times measured by SFG spectroscopy and by contact angle measurements differ by a factor of about 3 (Tab. 5.2). In the literature no quantitative relation is given between contact angle and the surface density of molecular groups on PDMS.

A possible candidate for the slow process may be the re-orientation and condensation of Si-O-H groups, which was proposed as a further mechanism of the hydrophobic recovery [99][5]. We took spectra in the IR frequency interval from 3000 cm^{-1} to 3750 cm^{-1} in order to monitor the SFG intensity of the hydroxyl group. No signal was found. In principle, the hydroxyl group is observable by SFG, as shown for water/solid and water/air interfaces [111, 112]. However, these systems exhibit a substantially higher density of hydroxyl groups than polymers do. We found no example in the literature for the detection of a hydroxyl group on a polymer by SFG spectroscopy.

By SFG spectroscopy it is possible to separate the contributions of re-orientation of methyl groups and diffusion of low molar mass PDMS to the hydrophobic recovery. For re-orientation the ratio of the peak intensities measured by the different polarization combinations changes [113]. If the signal increases at constant ratio the change can be attributed to additional groups appearing at the surface. The ratio of the peak intensities for the ppp and ssp polarization combinations in our measurements shows no trend during the recovery. Thus we do not see a direct indication of re-orientation. This may suggest, that diffusion is the dominating process for the increase in the density of orientated methyl groups.

---

[5]and references therein

Chapter 6

Intense localized emission from NaCl crystallites

During the SFM measurements sometimes regions on the scale of some micrometers were observed, which gave a localized intensity several hundred times higher than the SFG signal on a pure gold sample. These bright spots were at the same position, where particles on the substrate could be seen in the linear optical image. A higher SFG intensity is one of the most important issues in sum-frequency microscopy as it improves the SNR (see chapter 7). We did first experiments on gold with the aim to generate this effect reproducibly and to investigate, whether it can be possibly used for doing sum-frequency microcopy at surfaces with measurement times on the order of 1 min on the μm^2 scale. In comparison acquisition times in chapter 4 were on the scale of 1 to 2 h. To mimic the dust particles we chose small NaCl crystallites. Ideal NaCl crystallites exhibit no resonances due to absorption and no bulk sum-frequency generation as they are transparent for the visible as well as for the IR light and as the ion lattice is centrosymmetric.

We deposit pestled nutrition grade NaCl on a thiol-covered gold substrate. The size of the crystallites is 10-100 μm. A fraction of the NaCl crystallites show a strong signal in the SFM. The SFG intensity was found to depend linearly on the intensity of the visible laser beam. The signal vanishes if the IR pulses are delayed by 50 ps with respect to the visible laser pulses. These two facts show, that the signal is not fluorescence but behaves as expected for sum-frequency generation.

The image of such a crystallite obtained by illumination with 450 nm light is displayed in Fig. 6.1c (no SFM image). Fig 6.1a shows the SFM image ($\omega_{IR} = 2922$ cm^{-1}) at the same position. The acquisition time is only 2 min! The brightness scale is chosen
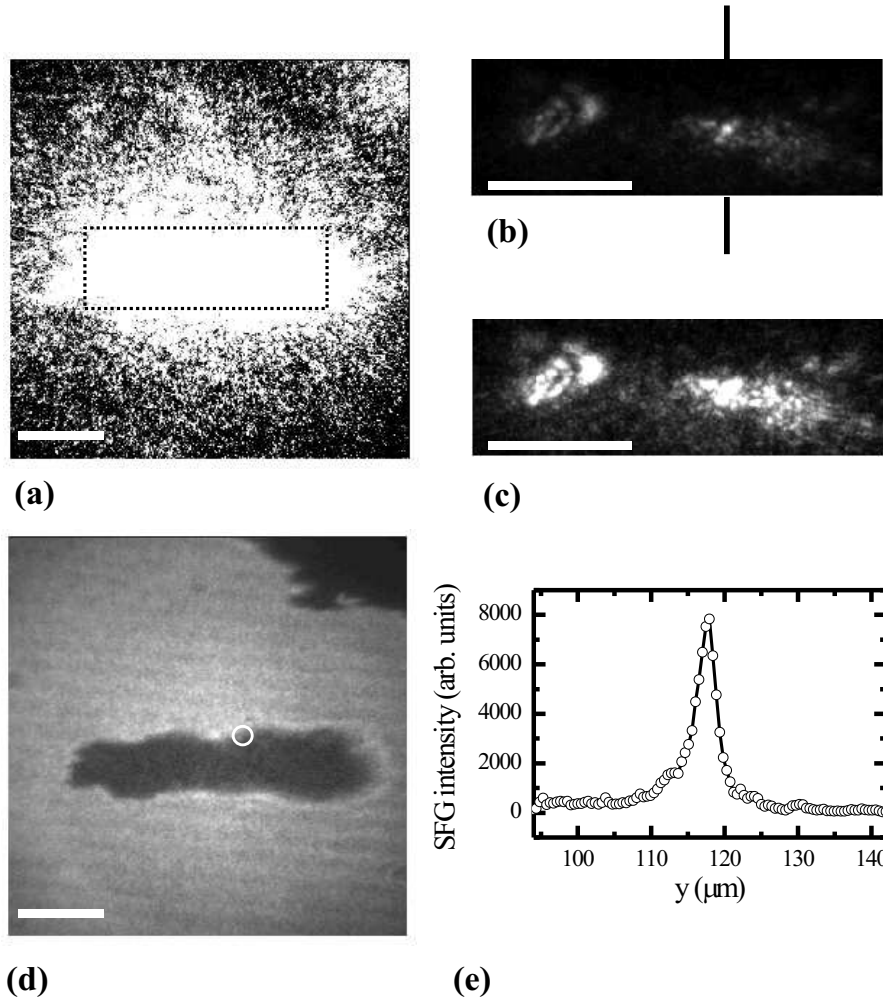
Figure 6.1: Sum-frequency generation by NaCl crystallites: (a) SFG image at 2922 cm^{-1} (acquisition time 120 s, the white area corresponds to an SFG intensity higher then the one obtained on a pure gold substrate). (b) Full scale image of the region indicated by the box in (a). (c) Same region but different intensity scale. (d) Reflected light image ($\lambda = 450$ nm) of the same region as in (a). The white circle marks the position of highest intensity in (b). (e) Single line cross section corresponding to the black line in (b). Details see text. (White bar = 50 μm)

such that the white area corresponds to SFG intensity higher than measured on typical gold samples for the corresponding laser pulse energies. The framed area is displayed in Fig. 6.1b with a brightness scale that includes the lowest and the highest SFG intensity value in that region. The highest intensity is located near the edge of the crystallite as indicated by the white circle in Fig. 6.1d. The spot size, as depicted by the single line cross section (Fig. 6.1e) at the position of the black line, is at the diffraction limit of ~ 3 μm. The SFG intensity in this maximum is 200 times higher than for a clean gold surface. Fig. 6.1c shows the same rectangle as in b at a different brightness scale
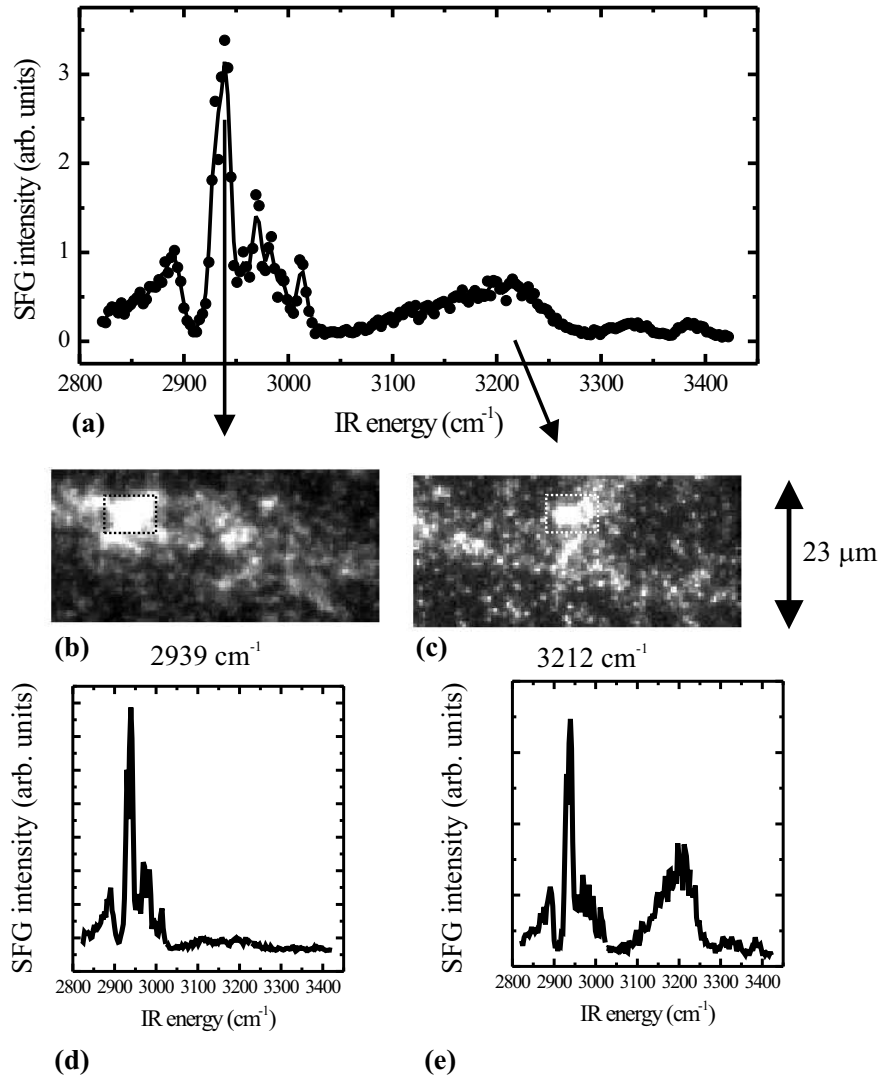
Figure 6.2: Spectral dependence: (a) Spectrum of a region around the intensity maximum in Fig. 6.1. (b+c) SFM image for the indicated resonances (acquisition times 7.5 s and 5 s respectively). (d+e) Local spectra for the regions marked in (b) and (c).

to demonstrate, that there is additional structure within the region of elevated SFG intensity.

Fig. 6.2a shows the spectrum for the bright region in the right half of Fig. 6.1c. Each data point in the interval from 2822 cm^{-1} to 3022 cm^{-1} is taken by integrating the SFG intensity over 3×2.5 s (150 laser shots), for the remaining wavelengths the average of 2×2.5 s (100 laser shots) was taken. The spectra are normalized to the exposure time. Several peaks are observed in the spectrum, some of them in the region of the C-H stretch vibrations. For the selected region the SFG intensity at $\omega_{IR} = 2939$ cm^{-1} is 200 times larger than for a gold surface. For the intensity maximum in the area this factor is
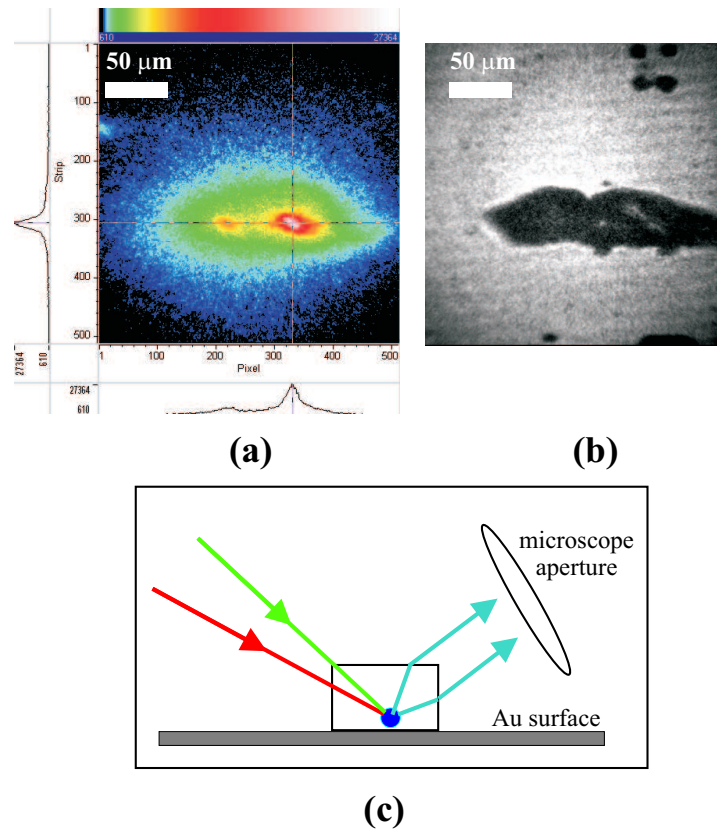
Figure 6.3: Sum-frequency generation in a NaCl crystallite viewed from two sides: (a) SFM image (logarithmic false color scale in the image, linear scale in the cross section). (b) Linear optical image ($\lambda = 450$ nm) of the same region. (c) Schematics of imaging on thick samples: Due to oblique imaging a source of intensity can be imaged twice if it is located inside a thick medium with high index of refraction.

1800. SFM images are displayed for the resonances at 2939 cm^{-1} and at 3212 cm^{-1}(Fig. 6.2b+c). The intensity maxima are separated by about 10 μm. The spectra of these two maxima (dashed box) contain both resonances (Fig. 6.2d+e). The different ratio of their amplitudes demonstrates that the resonance at 3200 cm^{-1} is correlated with the right intensity maximum in Fig. 6.2c. Similar spectra were obtained even for areas of 1 μm^2.

The spectral features on this crystallite are reproducible. It shall be noted, however, that on other crystallites investigated we see also a strongly enhanced SFG but no distinct spectral peaks.

In a next step to clarify the origin of the high SFG intensity we used pestled crystallites of chemically pure NaCl. Again a fraction of the crystallites showed strong SFG intensity. Fig. 6.3a is the SFM image of a typical crystallite, which appears in the linear
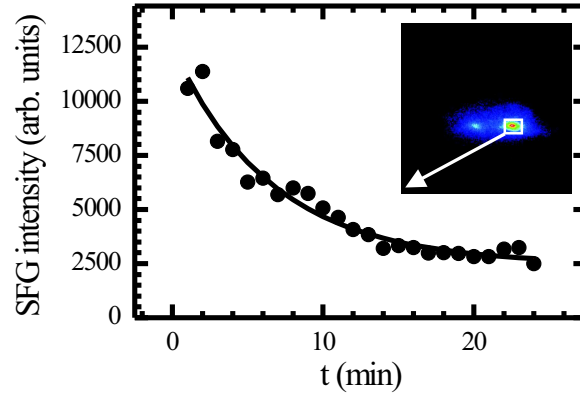
Figure 6.4: SFG intensity for an intensity maximum as a function of time. The inset shows a false color SFM image of the same sample as in Fig. 6.3 (linear scale)). The box corresponds to the area, where the SFG was evaluated.

optical image as shown in Fig. 6.3b. The false color SFG intensity scale is logarithmic in order to show the intensity distribution in the hot spot and the surrounding area in the same image. The intensity at the most intense pixel is about 700 times higher than on a pure gold surface. The intensity in the image shows a halo that extends beyond the region of the crystallite in the linear image. The double structure with two intensity maxima is observed for many NaCl crystallites (see also Fig. 6.1c). Due to the oblique imaging at the angle of 60° the SFM images the top and the side of a thick sample at the same time. A point in the crystallite can therefore appear at least twice in the image(Fig. 6.3c). The twin structure in the SFM image is thus most probably due to the multiple imaging of the same light source.

The intensity for different crystallites behaved differently in time. We observed bright spots with constant, fluctuating and decaying intensity. The graph in Fig. 6.4 is an example for the last kind. It gives the intensity as a function of time measured in the area of the intensity maximum (indicated by the white box in the inset) of the sample in Fig. 6.3.

In a next step NaCl crystallites are grown on a thiol-covered gold substrate by positioning a drop of aqueous NaCl solution on the sample and letting the solvent evaporate. This method seems to generate larger and more regular crystallites with less defects, as indicated by the macroscopic appearance in the image under linear illumination (Fig. 6.5b and schematics in c). Fig. 6.5a shows the false color SFM image of such a NaCl crystallite (logarithmic brightness scale) at the same sample position.

The intensity maximum in the SFM image is localized on the μm scale and it is near the edge of the crystallite. However, no halo but rather an irregular intensity distribution around the maximum is observed. The intensity in the most intense pixel is only 25 times higher than the corresponding SFG intensity for pure gold.
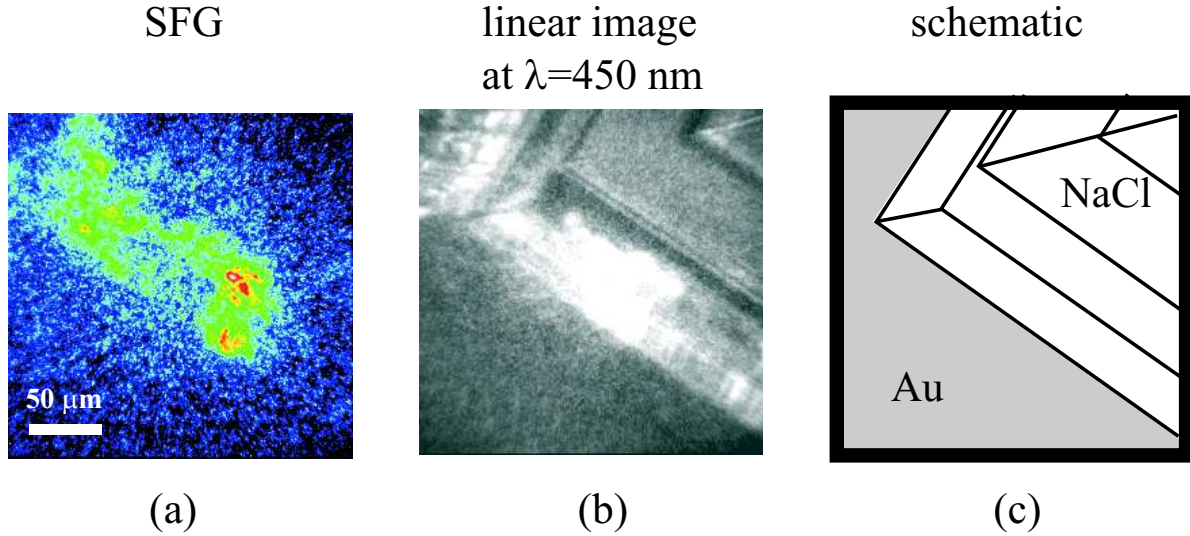
SFG	linear image at λ=450 nm	schematic

(a)	(b)	(c)

Figure 6.5: Sum-frequency generation from a solution grown NaCl crystallite: (a) SFM image (logarithmic brightness scale). (b) Linear optical image ($\lambda = 450$ nm) at the same position. (c) Schematics of the linear image.

Discussion

We can draw conclusions on the observed localized emission of intensity from NaCl crystallites, although this effect is not yet fully understood.

First, the signal was strongest for the nutrition quality (i.e. chemically highly unpure!) NaCl and lowest for the solution grown crystallites, which should be the best in terms of a low number of defects. This indicates, that defects in the crystallite are likely to play a role. They cannot be point defects (e.g. F-centers) with inversion symmetry. The generation of SFG requires e.g. inner surfaces, which break the local inversion symmetry of the crystal, or extended defects.

Second, also focusing effects of such inner and also outer surfaces can contribute. Sometimes bright spots are also seen in the linear optics images of the crystallite (Fig.6.5), indicating such an effect. However the maxima do not precisely coincide with those in the SFM images.

Third, if one assumes, that the signal (1800 times higher than the corresponding SFG signal from a gold surface) of the sample in Fig. 6.2b stems from the gold surface,

this means that the intensity at the surface is more than 40 times higher for the IR or the visible input ($I_{SFG} \propto I_{IR} \, I_{vis}$). This is definitely above the macroscopic damage threshold of the gold substrate. The halo observed e.g. in Fig. 6.3a exceeds the region of the crystallite (Fig. 6.3b). With these measurements the contribution of the Au surface to the bright spot and to the halo cannot be clarified. Possible experiments to test this, would be the use of a surface, which generates a negligible amount of sum-frequency light.

Fourth, local electrical charges in the NaCl could break the symmetry in NaCl and also contribute to a high local electrical field. This again might increase the nonlinear optical activity as in electric field induced second harmonic generation (EFISH).

A more detailed study would be necessary to further elucidate the origin of these microscopic and intense SFG sources.

Chapter 7

Conclusions and outlook

A novel SFG microscope for in-situ chemical imaging of reflecting, non-transparent samples was developed, set up and characterized in this thesis. The process of sum-frequency generation allows to map the chemical composition of interfaces and the order and molecular orientation of adsorbates at surfaces. In order to maximize the SFG intensity the sample has to be observed from one side at an angle near 60° with respect to the surface normal. The setup is designed (a) to keep focus over the full image field and (b) to compensate for the distortion of the field-of-view, and (c) to transmit efficiently the SFG light by means of a blazed grating. In contrast to "specular" SFG spectroscopy, the incident beams reflected from the sample and the generated SFG light cannot be separated by angular filtering. Blocking the reflected beams would also block a large part of the diffracted SFG light and would thus degrade the spatial resolution of the SFM. In this setup the separation thus relies on efficient spectral filtering. The filter combination suppresses the visible beam by more than 20 orders of magnitude, while letting pass 30% of the SFG intensity at 450 nm. The spatial resolution is 3 μm.

The laser setup, which generates visible laser pulses and tunable IR radiation, was moved from the EPFL to the MPI in Stuttgart. On rebuilding it, changes were made to triple the power of the mid-IR beam and to improve the long term beam stability.

Sum-frequency microscopy permits to probe quantitatively the chemical composition of an interface. This is demonstrated by imaging the edge of a microcontact printed thiolate SAM on Au. The chemical specificity allows to address the individual building blocks of a SAM – head group, terminal group and molecular backbone – and to distinguish between thiolate species like octadecanethiol and mercaptohexadecanoic acid. Sum-frequency microscopy is sensitive enough to quantify sub-monolayer coverages. The coverage of the thiolate between microcontact printed patterns on Au due to the vapor

phase transport was found to be surprisingly high. Monolayers with inscribed chemical micro-structures were pepared by microcontact printing and subsequent post-adsorption from solution. SFM images taken for each IR wavelength of an SFG spectrum and evaluating the spectra locally yields quantitative information on the mixing of thiolates as well as on the exchange of both thiolate species. An asymmetry with respect to the exchange was observed: Carboxyl terminated thiols displace alkanethiolates more readily than vice versa.

Measuring the SFG spectrum for one region of the image and calibrating it with the SFG intensity from a defined reference area in the same image was used for "on-substrate calibration". It improves the SNR in SFG spectra by a factor 2 to 3.

The hydrophobic recovery of PDMS – the material typically used for the stamps in microcontact printing – was studied by sum-frequency spectroscopy. In contrast to other IR techniques that lack the required surface sensitivity, SFG spectroscopy is apt to monitor the changes at the surface with chemical group selectivity. Furthermore it is sensitive to molecular order. The methyl groups are found to have a preferential orientation along the surface normal. During oxygen plasma etching the density of oriented methyl groups decreases only by 30%. A recovery of the density of preferentially oriented methyl groups within the first 200 h after exposure to the plasma was identified. Control experiments by contact angle measurements suggest that there exists a slower process, which determines the hydrophobic recovery of PDMS on the time scale of 1000 h.

NaCl crystallites were found to emit intense SFG radiation up to 2000 times stronger than the pure gold SFG signal when illuminated by visible and IR laser pulses. The origin of the effect could not be unambiguously identified. The results indicate, that it may be correlated to inner defects of the crystallites.

Future experiments can use the demonstrated capability of SFM to obtain quantitative chemical information on heterogeneous SAMs. This quantitative chemical information is in part complementary to the results obtainable by chemical AFM, which typically probes not the chemical composition directly but the hydrophobic interaction of the SAM with the functionalized AFM tip. SFM as a vibrational technique is particularly suited for processes, e.g. interdiffusion and self-exchange, which are preferably studied with deuterated and un-deuterated thiols. This is, because the hydrocarbon

vibrations of chemically identical thiols are clearly separated in the SFG spectrum due to the different mass of the hydrogen isotope.

Extending the scope, the three systems investigated in this thesis – organic monolayers as model system for biomembranes, a polymer surface, and a highly localized source of SFG – convey an impression of the wide applicability of the SFM microscope:

Resent SFG spectroscopy experiments on phospholipid membranes [114] and monolayers of biological molecules [115] could be extended to locally resolved studies, which address the ongoing question of the so-called "rafts", i.e. of structural inhomogeneities in cell membranes and vesicles [116, 117].

Devices of organic semiconductors made from organic crystalline material or polymers are increasingly investigated, because their production promises to be cheap and straightforward [118]. A critical factor is the interface between the organic material and the metal gate. SFM could be used to image the order, composition and the orientation of the molecules at this interface. Electric field induced sum-frequency generation may give information on the electric field at the interface similar to the established method of electric field induced second-harmonic generation.

From the experimental point of view, the spatial resolution of the SFM can be improved to the diffraction limit of about 1 μm by custom designing the 1:1 imaging optics.

The use of the SFM in combination with a high-repetition laser system ($\sim$kHz) would increase the SNR, which is determined by photon statistics, by at least 1 order of magnitude. Generally, a larger SFG signal results in a higher SNR. However, increasing the power density of either laser beam in our setup led to damage of the sample. As the sample damage is due to processes with a relaxation time of less than 1 ms (e.g. molecular vibrations) and not due to an averaged temperature rise, higher repetition laser systems can achieve higher SFG intensities and thus better signal-to-noise ratios. This is shown in the simulation (Fig. 7.1) of the SFM images in Fig. 4.17 for our 20 Hz and for a 1 kHz laser system.

The simulated pattern consists of 10 μm wide lines with 50 μm periodicity. The intensity of the area between the lines is set to 30 photons at the non-resonant wavelength. Thus the intensity for the pattern is set to $(1-0.08)\times30$ photons=27.6 photons for the non-resonant wavelength and to $(1-0.17)\times30$ photons=24.9 photons for the wavelength in resonance with the symmetric methyl vibration. The image at the detector was cal-
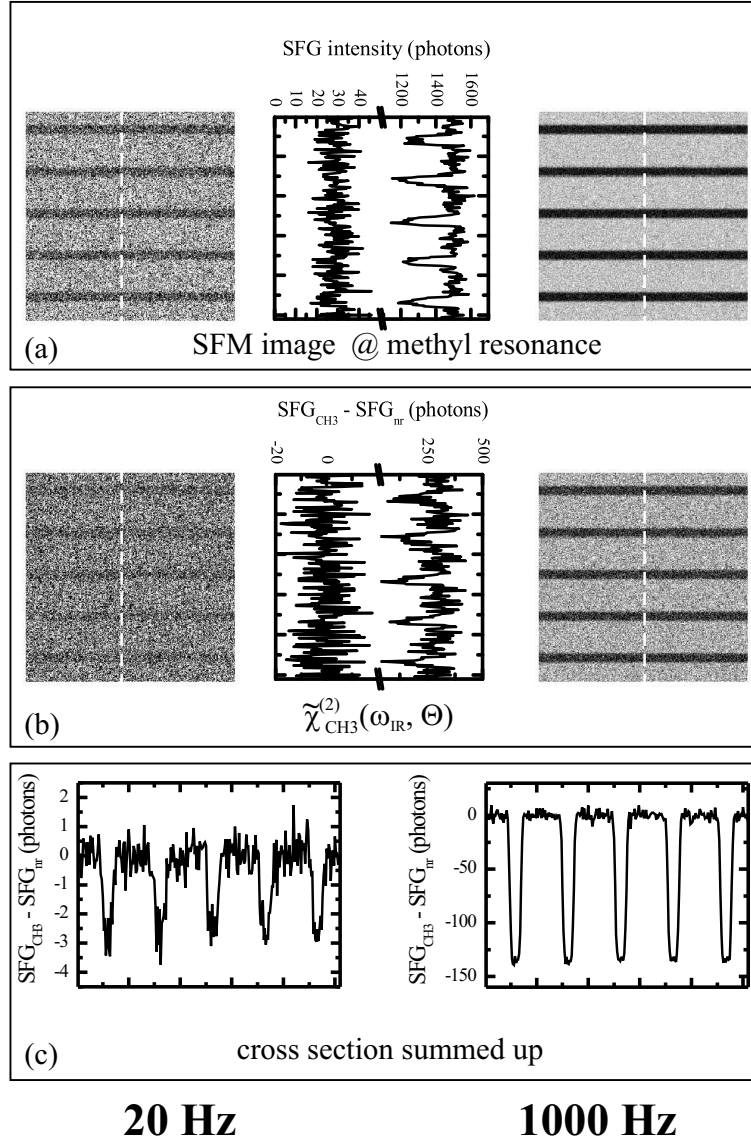
Figure 7.1: Simulation of the image of a micropatterned SAM: The left hand side corresponds to the 20 Hz laser system and the experimental values in Fig. 4.17 (images c, f, and i). The average intensity is 30 photons/pixel. On the right hand side a 50 times higher intensity as achievable with a high repetition laser system is simulated. The single line cross sections at the position of the dashed lines are shown on the respective side of the graph. (a) Simulated image at the resonance of the symmetric methyl stretch, i.e. at $\omega_{IR} = 2880$ cm^{-1} with a contrast of $17\% = 5.1$ photons/pixel. (b) Simulated difference between resonant and non-resonant image corresponding to $\tilde{\chi}^{(2)}_{CH3}$. (c) Cross section added up parallel to the lines similar as used in the evaluation of section 4.7.

culated by folding the pattern with a resolution function of 2.8 μm width. Photon noise was introduced by a poisson distribution for the intensity received by each pixel with the average intensity as parameter. The reduction of the SNR by 10% due to the scatter in the MCP amplification factor for an individual photon (see section 3.3) is neglected.

Fig. 7.1a,left shows the simulated SFM image, if ω_{IR} is in resonance with the symmetric methyl vibration. The contrast in the simulation appears as in the experimental data in Fig. 4.17c. A single line cross section at the position of the dashed line is shown to the right of the image.

Fig. 7.1b,left shows the simulated difference $I_{nr} - I_{CH3}$, which can be compared to Fig. 4.17f. As for the raw SFM image the SNR in the single line cross section (to the right of the image) is too low, to identify the contrast between lines and interspaces.

Therefore a cross section is calculated by adding up the pixels along the direction of the pattern (Fig. 7.1c,left) as it is done in the experimental results. The SNR is about 3 in agreement with experiment (Fig. 4.17i).

As already mentioned in section 3.3, there are laser systems operating in the mid infrared with a repetition rate of 1 to 2 kHz. To estimate the performance of our SFM attached to such a laser system, the same simulation was done for an SFG intensity being 50 times higher.

The simulated raw data (for the ICCD configuration) (Fig. 7.1a,right) and the single cross section demonstrate, that the SNR is high enough after two hours to allow the pixel-wise measurements of a contrast of 17%. In the methyl map the SNR is still large enough to make the chemical contrast observable in the single pixel noise (Fig. 7.1b,right).

The SNR is reduced by a factor of $\sqrt{50}$ for the summed-up cross section in (Fig. 7.1c,right).

As the simulation reproduces the magnitude of the noise in the experimental data it can be concluded that the statistics in our SFM images is dominated by the photon noise. Furthermore the results for a 1000 Hz system conveys an impression how sensitive the SFM can be in combination with a high repetition laser system.

The sensitivity is increased further because the SFM should be used without image intensifier at these intensities. This would mean another gain by a factor of 5 in the detected number of photons due to the better quantum efficiency of the CCD when compared to the MCP.

Appendix A: Initial alignment of the SFM

The alignment of the sum-frequency microscope has to fulfill two main demands: First, the image plane of the 1:1 optics has to be identical with the object plane of the magnifying microscope. Second the conjugate planes of the magnifying microscope have to be parallel in order to ensure an optimum performance. In the following the routine of setting up and aligning our SFM is described.

Step 1 Standard beam height: The CCD camera is illuminated by parallel light. This is realized by a cold-light source at a distance of about 3 m. An iris aperture is placed directly in front of the camera such that its hole is at the central height of the chip. This pinhole is used as the standard for defining the height in all following steps.

Step 2 Path A: The beam paths are principally defined with a HeNe laser before inserting any optical elements. Path A (Fig. 7.2) defines the optical axis of the magnifying microscope.

Step 3 Grating alignment: The grating, which can be translated along three directions in order to utilize the highest quality position on the grating, is inserted perpendicular to path A. It is adjusted by rotation around the x and y axis such that the $0th$ order reflection of the HeNe laser is going back the same way as the incoming beam. Subsequently the grating is rotated around the y axis so that the $1st$ order diffraction is observable. Its height is adjusted to the norm pinhole by a z-rotation of the grating. Both steps are repeated until both orders have standard height.

Step 4 Path B: Now the optical axis of the 1:1 imaging path is defined by the HeNe laser(path B). Path A and path B are to coincide onto the grating with an angle of 60°. The 400 μm pinhole allows for overlapping both beams with sub-mm precision.

Step 5 Microscope objective: The objective is positioned into path A. The coarse alignment is guaranteed, if the focus of beam A impinges at the same position on the grating as before. Fine tuning is done by tilting and by y- and x- translations of the objective until the beam reflected from the grating is running along path A. When the
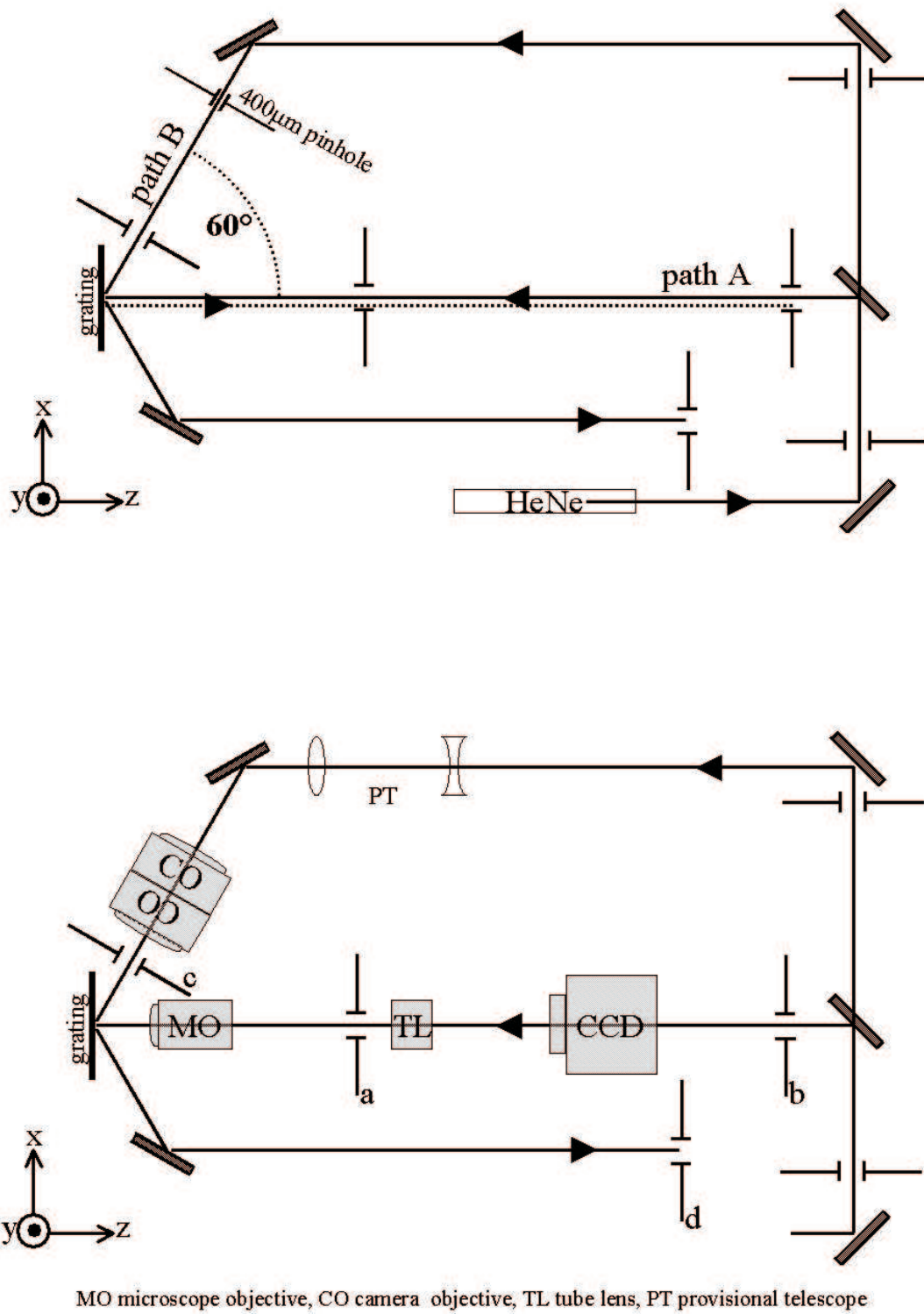
MO microscope objective, CO camera objective, TL tube lens, PT provisional telescope

Figure 7.2: Schematics for the aligning procedure of the SFM.

objective is defocused, i.e. moved along the z-direction, the reflection diameter has to increase symmetrically around the apertures a and b.

Step 6 Camera objectives: For symmetrical reasons the distance between the sample and the camera objectives (COs) equals the distance between the COs and the grating and it is ca. 37 mm. The COs are inserted into path B at that distance to the grating. Similar to step 5 they are aligned such that the transmitted HeNe beam still passes the pinholes c and d. The HeNe beam is now focused in front of the COs by a provisional telescope(PT). The convex lens and thus the focus of the HeNe light is moved along path b until the spot on the grating is focused as well. The distance between the COs and the focus has to be equal to the separation grating – COs.

Step 7 Tube lens: The tube lens(TL) is inserted into path A. The distance between the backside of MO and the front of TL should be in the range of 100-200 mm. The transmitted HeNe beam has to pass pinhole a, the reflected one passes pinhole b.

Step 8 CCD: The CCD camera is placed at a distance of about 150 mm from the tube lens. The HeNe laser is newly set up: It runs for ca. 7 m before it passes the tube lens and is focused on the CCD chip. Attenuation with the nominally infinite filter and at least one further filter is necessary in order to avoid overloading the CCD chip! The tube lens is moved along z until the focus recorded by the CCD is minimal. This separation corresponds to the imaging distance b. The final separation is found by taking into account the divergence of the HeNe laser using

$$\frac{1}{f} = \frac{1}{b} + \frac{1}{g}. \tag{7.1}$$

The focal width f being 200 mm and the distance from the laser to the tube lens being $g = 7000$ mm we can calculate a difference between imaging distance b and f of ≈ 5.6 mm. The tube lens is shifted that far.

Step 9 Focusing: Now the microscope objective is adjusted to image the edge of the grating.

Step 10 MCP: The MCP is mounted to the CCD. Step 8 is repeated accordingly and by repeating step 9 one assures that the edge is still in focus.

Step 11 Sample: A sample is positioned before the camera objectives. Using defined test structures the sample plane is finely adjusted and the magnification is determined.

Appendix B: Abbreviations and Common Symbols

AFM	atomic force microscopy
CARS	coherent anti-Raman spectroscopy
C_n	alkanethiol(ate) with n-1 methylene groups
C_nCOOH	alkanethiol(ate) with n-1 methylene groups and a terminal carboxyl group
FFM	friction force microscopy
FWHM	full width at half maximum/minimum
GIXD	grazing incidence X-ray diffraction
HREELS	high resolution electron energy loss spectroscopy
(I)CCD	(intensified) charge coupled device
LFM	lateral force microscopy
ML	a full **monolayer** of thiolate in $(\sqrt{3} \times \sqrt{3})$R30° structure
μCP	microcontact printing
OPA	optical parametric amplification
OPG	optical parametric generation
PDMS	polydimethylsiloxane
SAM	self-assembled monolayer
SEM	scanning electron microscopy
SFG	sum-frequency generation
SFM	sum-frequency microscopy
SHG	second-harmonic generation
SIMS	secondary ion mass spectroscopy
SNR	signal-to-noise ratio
STM	scanning tunnelling microscopy
UHV	ultra high vacuum
XPS	X-ray photoelectron spectroscopy

Bibliography

[1] F. Zernike and J.E. Midwinter, *Applied Nonlinear Optics* (Wiley & Sons, New York, 1973).

[2] R. W. Boyd, *Nonlinear Optics* (Academic Press, San Diego, 1992).

[3] P. Guyot-Sionnest, J.H. Hunt, and Y.R. Shen, Phys. Rev. Lett. **59**, 1597 (1987).

[4] R. Superfine, J.Y. Huang, and Y.R. Shen, Phys. Rev. Lett. **66**, 1066 (1991).

[5] M. Himmelhaus, Ph.D. thesis, University of Heidelberg, 1997.

[6] C. Hirose, N. Akamatsu, and K. Domen, Applied Spectroscopy **46**, 1051 (1992).

[7] M. Epple, Ph.D. thesis, École Polytechnique Fédérale de Lausanne, 2000.

[8] *American Institute of Physics Handbook, 3rd Ed.*, edited by D.E. Gray (Mc Graw Hill, New York, 1972).

[9] J.H. Hunt, P. Guyot-Sionnest, and Y.R. Shen, Chem. Phys. Lett. **133**, 189 (1987).

[10] Y.R. Shen, *The Principles of Nonlinear Optics* (Wiley & Sons, New York, 1984).

[11] A.L. Harris, C.E.D. Chidsey, N.J. Levinos, and D.N. Loicano, Chem. Phys. Lett. **141**, 350 (1987).

[12] M. Epple, A.M. Bittner, K. Kuhnke, K. Kern, W.-Q. Zheng, and A. Tadjeddine, Langmuir **18**, 773 (2002).

[13] P.B. Johnson and R.W. Christy, Phys. Rev. B **6**, 4370 (1972).

[14] H.-J. Krause, Ph.D. thesis, Forschungszentrum Jülich, 1992.

[15] H.-J. Krause and W. Daum, Appl. Phys. B **56**, 1 (1993).

[16] Continuum, Operation and Maintenance Manual, PY61 Series Laser.

[17] A. Volkmer, J.-X. Cheng, and X. S. Xie, Phys. Rev. Lett. **87**, 23901 (2001).

[18] M. Floersheimer, C. Brillert, and H. Fuchs, Mater. Sci. Eng. **C 8-9**, 335 (1999).

[19] Y. Shen, J. Swiatkiewicz, J. Winiarz, M. Przemyslaw, and P.N. Prasad, Appl. Phys. Lett. **19**, 2946 (2000).

[20] B. Humbert, J. Grausem, A. Burneau, M. Spayer, and A. Tadjeddine, Appl. Phys. Lett. **78**, 135 (2001).

[21] R. D. Schaller and J. Saykally, Langmuir **17**, 2055 (2001).

[22] J. Squier and M. Mueller, Rev. Sci. Instrum. **72**, 2855 (2001).

[23] T. A. Klar and S. W. Hell, Opt. Lett. **24**, 954 (1999).

[24] I. Freund and M. Deutsch, Opt. Lett. **11**, 94 (1986).

[25] K. A. Schultz and E. G. Seebauer, J. Chem. Phys. **97**, 6958 (1992).

[26] M. Floersheimer, D. H. Jundt, H. Looser, K. Sutter, M. Kuepfer, and P. Guenther, Ber. Bunsenges. Phys. Chem. **98**, 521 (1994).

[27] M. Floersheimer, C. Brillert, and H. Fuchs, Langmuir **15**, 5437 (1999).

[28] G. Haas, Ph.D. thesis, Freie Universität Berlin, 1997.

[29] J. C. Chastang, Proc. SPIE **399**, 239 (1983).

[30] W. J. Smith, *Practical Optical System Layout* (McGraw-Hill, New York, 1997).

[31] Princeton Instruments Inc., *Manual: Lens-Coupled ICCD Detector*.

[32] *Handbook of Microscopy, Methods II*, edited by S. Amelinckx, D. Van Dyck, J. Van Landuyt, and G. Van Tenedeloo (VCH, Weinheim, 1997).

[33] R.G. Nuzzo and D.L. Allara, J. Am. Chem. Soc. **105**, 4481 (1983).

[34] F. Schreiber, Prog. Surf. Sci. **65**, 151 (2000).

[35] C.A. Alves, E.L. Smith, and M.D. Porter, J. Am. Chem. Soc. **114**, 1222 (1992).

[36] M.S. Yeganeh, S.M. Dougal, R.S. Polizozzi, and P. Rabinowitz, Phys. Rev. Lett. **74**, 1811 (1995).

[37] M. Himmelhaus, F. Eisert, and M. Grunze, J. Phys. Chem. B **104**, 576 (2000).

[38] A.M. Bittner, M. Epple, K. Kuhnke, R. Houriet, A. Heusler, H. Vogel, A.P. Seitsonen, and K. Kern, J. Electroanal. Chem., in print (2003).

[39] C.D. Bain, E.B. Troughton, Y.-T. Tao, J. Evall, G.M. Whitesides, and R.G. Nuzzo, J. Am. Chem. Soc. **111**, 321 (1989).

[40] A. Kumar and G.M. Whitesides, Appl. Phys. Lett **63**, 2002 (1993).

[41] Y. Xia and G.M. Whitesides, Angew. Chem., Int. Ed. Engl. **37**, 550 (1998).

[42] Y. Kim, K.-S. Kim, M. Park, and J. Jeong, Thin Solid Films **341**, 91 (1999).

[43] M. Fujihira, M. Furugori, U. Akiba, and Y. Tani, Ultramicroscopy **86**, 75 (2001).

[44] G. J. Kluth, C. Carraro, and R. Maboudian, Phys. Rev. B **59**, R10499 (1999).

[45] C.E.D. Chidsey, G.-L. Liu, P. Rowntree, and G. Scoles, J. Chem. Phys. **91**, 4421 (1989).

[46] D.L. Lavrich, S.M. Wetterer, S.L. Bernasek, and G. Scoles, J. Phys. Chem. B **102**, 3456 (1998).

[47] R.G. Nuzzo, L.H. Dubois, and D.L. Allara, J. Am. Chem. Soc. **112**, 558 (1990).

[48] L. Strong and G.M. Whitesides, Langmuir **4**, 546 (1988).

[49] N. Camillone, C.E.D. Chidsey, G.-L. Liu, and G. Scoles, J. Chem. Phys. **98**, 3503 (1993).

[50] G.E. Poirier and M.J. Tarlov, Langmuir **10**, 2853 (1994).

[51] P. Fenter, F. Schreiber, L. Berman, G. Scoles, P. Eisenberger, and M.J. Bedyzek, Surf. Sci. **412/413**, 213 (1998).

[52] R.G. Nuzzo, E.M. Korenic, and L.H. Dubois, J. Chem. Phys. **93**, 767 (1990).

[53] P.E. Laibinis, G.M. Whitesides, D.L. Allara, Y.T. Tao, A. N. Parikh, and R.G. Nuzzo, J. Am. Chem. Soc. **113**, 7152 (1991).

[54] R.H. Terrill, T.A. Tanzer, and P.W. Bohn, Langmuir **14**, 845 (1998).

[55] J. Thome, M. Himmelhaus, M. Zharnikov, and M. Grunze, Langmuir **14**, 7435 (1998).

[56] P. Fenter, A. Eberhardt, K.S. Liang, and P. Eisenberger, J. Chem. Phys. **106**, 1600 (1997).

[57] M.D. Porter, T.B. Bright, D.L. Allara, and C.E.D. Chidsey, J. Am. Chem. Soc. **109**, 3559 (1987).

[58] N. Camillone, P. Eisenberger, T.Y.B. Leung, P. Schwartz, G. Scoles, G. E. Poirier, and M. Tarlov, J. Chem. Phys. **101**, 11031 (1994).

[59] G. E. Poirier, M.J. Tarlov, and H.E. Rushmeier, Langmuir **10**, 3383 (1994).

[60] N. Camillone, T.Y.B. Leung, P. Schwartz, P. Eisenberger, and G. Scoles, Langmuir **12**, 2737 (1996).

[61] R. Staub, M. Toerker, T. Fritz, T. Schmitz-Hübsch, F. Sellam, and K. Leo, Langmuir **14**, 6693 (1998).

[62] F. Schreiber, A. Eberhardt, T.Y. Leung, P. Schwartz, S.M. Wetterer, D.J. Lavrich, L. Berman, P. Fenter, P. Eisenberger, and G. Scoles, Phys. Rev. B **57**, 12476 (1998).

[63] C. Zeng, B. Wang, B. Li, H. Wang, and J.G. Hou, Appl. Phys. Lett. **79**, 1685 (2001).

[64] R. Yamada and K. Uosaki, Langmuir **13**, 5218 (1997).

[65] R. Yamada and K. Uosaki, Langmuir **14**, 855 (1998).

[66] X. Xiao, B. Wang, C. Zhang, Z. Yang, and M.M.T. Loy, Surf. Sci. **472**, 41 (2001).

[67] M. Kawasaki, T. Sato, T. Tanaka, and K. Takao, Langmuir **16**, 1719 (2000).

[68] L. Houssiau and P. Bertrand, Appl. Surf. Sci. **175**, 399 (2001).

[69] K. Tamada, M. Hara, H. Sasabe, and W. Knoll, Langmuir **13**, 1558 (1997).

[70] O. Dannenberger, M. Buck, and M. Grunze, J. Phys. Chem. B **103**, 2202 (1999).

[71] M. Buck, F. Eisert, J. Fischer, M. Grunze, and F. Träger, Appl. Phys. A **53**, 552 (1991).

[72] G. Kaltenpoth, B. Volkel, C.T. Nottbohm, A. Golzhauser, and M. Buck, J. Vac. Sci. Technol. B **20**, 2734 (2002).

[73] R.D. Piner, J. Zhu, F. Xu, S.H. Hong, and C.A. Mirkin, Science **283**, 661 (1999).

[74] E. Delamarche, H. Schmid, A. Bietsch, N.B. Larsen, H. Rothuizen, B. Michel, and H.A. Biebuyck, J. Phys. Chem. B **102**, 3324 (1998).

[75] J.B. Renault, A. Bernard, A. Bietsch, B. Michel, H.R. Bosshard, E. Delamarche, M. Kreiter, B. Hecht, and U.P. Wild, J. Phys. Chem. B **107**, 703 (2003).

[76] A. Kumar, H.A. Biebuyck, and G.M. Whitesides, Langmuir **10**, 1498 (1994).

[77] M. Mrksich, L.D. Dike, J. Tien, D. E. Ingber, and G. M. Whitesides, Experimental Cell Research **235**, 305 (1997).

[78] D. Hobara and T. Kakiuchi, Electrochemistry Communications **3**, 154 (2001).

[79] H. Klein, N. Battaglani, B. Bellini, and Ph. Dumas, Mater. Sci. Eng. C **29**, 279 (2002).

[80] C.D. Bain, J. Evall, and G.M. Whitesides, J. Am. Chem. Soc. **111**, 7155 (1989).

[81] T. Kakiuchi, K. Sato, M. Iida, D. Hobara, S. Imabayashi, and K. Niki, Langmuir **16**, 7238 (2000).

[82] C. Chung and M. Lee, Journal of Electroanalytical Chemistry **486**, 91 (1999).

[83] E. Cooper and G.J. Leggett, Langmuir **15**, 1024 (1999).

[84] J.B. Schlenoff, M. Li, and H. Ly, J. Am. Chem. Soc. **117**, 12528 (1995).

[85] T.H. Ong and P.B. Davies, Langmuir **9**, 1836 (1993).

[86] M.A. Hines, J.A. Todd, and P. Guyot-Sionnest, Langmuir **11**, 493 (1995).

[87] O. Dannenberger, K. Weiss, H.-J. Himmel, B. Jäger, M. Buck, and C. Wöll, Thin Solid Films **307**, 183 (1997).

[88] D. Lin-Vien, N.B. Colthup, W.G. Fateley, and J.G. Grasselli, *The Handbook of Infrared and Raman Characteristic Frequencies of Organic Molecules* (Academic Press, San Diego, 1991).

[89] D. Fischer, A. Marti, and G. Hähner, J. Vac. Sci. Technol. A **15**, 2173 (1997).

[90] A.S. Eberhardt, R.M. Nyquist, A.N. Parikh, T. Zawodzinski, and B.I. Swanson, Langmuir **15**, 1595 (1999).

[91] N.B. Larsen, H. Biebuyck, E. Delamarche, and B. Michel, J. Am. Chem. Soc. **119**, 3017 (1997).

[92] I. Böhm, A. Lampert, M. Buck, F. Eisert, and M. Grunze, Appl. Surf. Sci. **141**, 237 (1999).

[93] G. Bar, S. Rubin, T.N. Taylor, B.I. Swanson, T.A. Zawodzinski Jr., J.T. Chow, and J.P. Ferraris, J. Vac. Sci. Technol. A **14**, 1794 (1996).

[94] G. Bar, S. Rubin, A.N. Parikh, B.I. Swanson, T.A. Zawodzinski Jr., and M.-H. Whangbo, Langmuir **13**, 373 (1997).

[95] F. Eisert, F. Gudmundson, and A. Rosén, Appl. Phys. B **68**, 579 (1999).

[96] F. Reif, *Fundamentals of Statistical and Thermal Physics* (McGraw-Hill, New York, 1965).

[97] Y. Okabe, U. Akiba, and M. Fujihira, Appl. Surf. Sci. **157**, 398 (2000).

[98] D. J. Graham, D. D. Price, and B. D. Ratner, Langmuir **18**, 1518 (2002).

[99] M. Morra, E. Occhiello, R. Marola, F. Garbassi, P. Humphrey, and D. Johnson, J. Coll. Interfac. Sci. **137**, 11 (1990).

[100] H. Hillborg, M. Sandelin, and U.W. Gedde, Polymer **42**, 7349 (2001).

[101] A. Toth, I. Bertoti, M. Blazso, G. Banhegyi, A. Bognar, and P. Szaplonczay, J. Appl. Polym. Sci. **52**, 1293 (1994).

[102] J. L. Tan, J. Tien, and C.S. Chen, Langmuir **18**, 519 (2002).

[103] J.M.G. Ng, I. Gitlin, A.D. Stroock, and G.M. Whitesides, Electrophoresis **23**, 3461 (2002).

[104] T. Kikuchi, S. Nishimura, M. Nagao, K. Izumi, Y. Kubota, and M. Sakata, IEEE Trans. Diel. Electr. Insul. **6**, 548 (1999).

[105] H. Hillborg, J.F. Ankner, U.W. Gedde, G.D. Smith, H.K. Yasuda, and K. Wikström, Polymer **41**, 6851 (2000).

[106] J. Kim, M.K. Chaudhury, M.J. Owen, and T. Orbeck, J. Colloid Interface Science **244**, 200 (2001).

[107] X. Wei, S.-C. Hong, A.I. Lvovsky, H. Held, and Y. R. Shen, J. Phys. Chem. B **104**, 3349 (2000).

[108] D. Zhang, R. S. Ward, Y.R. Shen, and G. A. Somorjai, J. Phys. Chem. B **101**, 9060 (1997).

[109] T. Pham, J.B. Jackson, N.J. Halas, and T.R. Lee, Langmuir **18**, 4915 (2002).

[110] T. Young, Philos. Trans. R. Soc. (London) **95**, 65 (1805).

[111] Q. Du, E. Freysz, and Y.R. Shen, Science **264**, 826 (1994).

[112] M.S. Yeganeh, S.M. Dougal, and H.S. Pink, Phys. Rev. Lett. **83**, 1179 (1999).

[113] Z. Chen, R. Ward, Y. Tian, S. Baldelli, A. Opdahl, Y.-R. Shen, and G. A. Somorjai, J. Am. Chem. Soc. **122**, 10615 (2000).

[114] T. Petralli-Mallow, K.A. Briggman, L.J. Richter, J.C. Stephenson, and A.L. Plant, Proc. SPIE **3858**, 25 (1999).

[115] R.A. Walker, J.A. Gruetzmacher, and G.L. Richmond, J. Am. Chem. Soc. **120**, 6991 (1998).

[116] K. Simons and E. Ikonen, Nature **387**, 569 (1997).

[117] S.L. Veatch and S.L. Keller, Phys. Rev. Lett. **89**, 268101 (2002).

[118] J.M. Shaw and P.F. Seidler, IBM J. Res. & Dev. **45**, (2001).

Acknowledgments

At the end of this thesis I would like to express my gratitude to those who supported me during the past years and contributed in various ways to the success of this work:

To Prof. Klaus Kern for the opportunity and the support in doing something really new. This was facilitated a lot by the very good conditions and possibilities he has provided in his group in general and for the project in particular.

To Klaus Kuhnke for the collaboration and companionship in the hunt for photons. Thanks especially for motivating advice, for many discussions, for new ideas, and for taking turns at measuring.

To the people in the IPN in Lausanne, where I spent and enjoyed the first 7 months of the thesis. Particularly I would like to thank Maximilian Epple for getting me started in the SFG business.

Thanks to the experts on SAMs in our group – Alexander Bittner, Xiaochun Wu, and Mato Knez – for introducing me to microcontact printing and for many information about the "life of thiols". Ralf Vogelgesang for the discussions about our projects, about numerous aspects in optics and, if that was not enough, about new business ideas in physics. Wolfgang Stiepany for starting the laser early in the morning and Wolfgang Heinz and Rafail Chaikevitch for marvellous and prompt support in designing and building mechanical and electric components. Sabine Birtel for the help in many organizational matters.

The valuable collaboration with many members of different service groups is highly appreciated. Thanks also to Dr. Irslinger, that we could always count on his support during our time as PhD speakers.

Curriculum vitae

Name:	Dominik M.P. Hoffmann
Date of Birth:	April 29, 1973
Nationality:	German

September 2003	PhD thesis: "Development of a versatile sum-frequency generation microscope and application to chemical imaging of interfaces"
2000–2003	Research assistant in the group of Prof. K. Kern in the Department of Nanoscale Science at the Max-Planck-Institut für Festkörperforschung in Stuttgart, Germany
Nov. 1999–2000	Research assistant in the group of Prof K. Kern at the École Polytechnique Fédérale de Lausanne, Switzerland
Okt. 1998–Okt. 1999	Diploma thesis in the group of Prof. A. Forchel at the Department of Technical Physics of the Bayerische-Julius-Maximilians-Universität Würzburg: "Elektronenwellenleiter in AlGaAs/GaAs-Heterostrukturen"
1996–1997	Graduate studies in physics at the State University of New York at Stony Brook, USA
1993–1999	Diploma studies in physics at the Bayerische-Julius-Maximilians-Universität Würzburg, Germany
1988	Middle School at the Glenstal Abbey School, Republic Ireland
1984–1992	Middle and High School at the Collegium Augustinianum Gaesdonck, Goch, Germany
1983–1984	Middle School at the Markt-Gymnasium Bünde, Germany

Publications

- *Sum-frequency generation microscope for opaque and reflecting samples*,
  D.M.P. Hoffmann, K. Kuhnke, and K. Kern, Rev. Scient. Instr. 73 (9), 3221(2002)

- *Chemical imaging of structured SAMs with a novel SFG microscope*,
  D.M.P. Hoffmann, K. Kuhnke, and K. Kern in "Nonlinear Spectroscopy", D.L. Andrews, Ed., Proceedings of SPIE Vol. 4812, 82 (2002)

- *Binding the Tobacco Mosaic Virus to Inorganic Surfaces*,
  M. Knez, M.P. Sumser, A.M. Bittner, C. Wege, H. Jeske, D.M.P. Hoffmann, K. Kuhnke, and K. Kern, (submitted)

- *Chemical Imaging of Interfaces by Sum-Frequency Generation Microscopy: Application to Patterned Self-Assembled Monolayers*,
  K. Kuhnke, D. M. P. Hoffmann, A.M. Bittner, X.C. Wu, and K. Kern, (submitted)